



Sediment transport processes over benthic ecosystems

Ryan Lowe^{1,4}, Marco Ghisalberti^{2,3,4}, Andrew Pomeroy^{1,4}, Mike Cuttler^{1,4},
Carlin Bowyer

¹School of Earth Sciences, UWA Oceans Institute and ARC Centre for Coral Reef Studies, The University of Western Australia, Crawley, Western Australia, Australia

²School of Civil, Environmental and Mining Engineering, The University of Western Australia, Crawley, Western Australia, Australia

³Department of Infrastructure Engineering, The University of Melbourne, Melbourne, Victoria, Australia

⁴Western Australian Marine Science Institution, Perth, Western Australia, Australia

WAMSI Dredging Science Node

Final Report

Theme 3 | Project 3.3

March 2019



WAMSI Dredging Science Node

The WAMSI Dredging Science Node is a strategic research initiative that evolved in response to uncertainties in the environmental impact assessment and management of large-scale dredging operations and coastal infrastructure developments. Its goal is to enhance capacity within government and the private sector to predict and manage the environmental impacts of dredging in Western Australia, delivered through a combination of reviews, field studies, laboratory experimentation, relationship testing and development of standardised protocols and guidance for impact prediction, monitoring and management.

Ownership of Intellectual property rights

Unless otherwise noted, any intellectual property rights in this publication are owned by the Western Australian Marine Science Institution, the Australian Institute of Marine Science and the University of Western Australia.

Copyright

© Western Australian Marine Science Institution

All rights reserved.

Unless otherwise noted, all material in this publication is provided under a Creative Commons Attribution 3.0 Australia Licence. (<http://creativecommons.org/licenses/by/3.0/au/deed.en>)



Funding Sources

The \$20 million Dredging Science Node is delivering one of the largest single issue environmental research programs in Australia. This applied research is funded by **Woodside Energy, Chevron Australia, BHP Billiton and the WAMSI Partners** and designed to provide a significant and meaningful improvement in the certainty around the effects, and management, of dredging operations in Western Australia. Although focussed on port and coastal development in Western Australia, the outputs will also be broadly applicable across Australia and globally.

This remarkable **collaboration between industry, government and research** extends beyond the classical funder-provider model. End-users of science in regulator and conservation agencies, and consultant and industry groups are actively involved in the governance of the node, to ensure ongoing focus on applicable science and converting the outputs into fit-for-purpose and usable products. The governance structure includes clear delineation between end-user focussed scoping and the arms-length research activity to ensure it is independent, unbiased and defensible.

And critically, the trusted across-sector collaboration developed through the WAMSI model has allowed the sharing of hundreds of millions of dollars worth of environmental monitoring data, much of it collected by environmental consultants on behalf of industry. By providing access to this usually **confidential data**, the **Industry Partners** are substantially enhancing WAMSI researchers' ability to determine the real-world impacts of dredging projects, and how they can best be managed. Rio Tinto's voluntary data contribution is particularly noteworthy, as it is not one of the funding contributors to the Node.

Funding and critical data

Critical data



Legal Notice

The Western Australian Marine Science Institution advises that the information contained in this publication comprises general statements based on scientific research. The reader is advised and needs to be aware that such information may be incomplete or unable to be used in any specific situation. This information should therefore not solely be relied on when making commercial or other decision. WAMSI and its partner organisations take no responsibility for the outcome of decisions based on information contained in this, or related, publications.

Year of publication: 2019

Metadata: <http://catalogue.aodn.org.au/geonetwork/srv/eng/metadata.show?uuid=07556fa0-d8ae-4b19-95dd-def52db223a1>

<http://catalogue.aodn.org.au/geonetwork/srv/eng/metadata.show?uuid=a0b7f5c8-aac3-4498-a7f8-a127c11f8f02>

Citation: Lowe R, Ghisalberti M, Pomeroy A, Cuttler M, Bowyer C (2019) Sediment transport processes over benthic ecosystems. Report of Theme 3 – Project 3.3 prepared for Dredging Science Node, Western Australian Marine Science Institution, Perth, Western Australia, 99 pp.

Corresponding author and Institution: R Lowe (UWAS). Email address: Ryan.Lowe@uwa.edu.au

Competing Interests: The commercial investors had no role in the data analysis, data interpretation, the decision to publish or in the preparation of the manuscript. The authors have declared that no competing interests exists.

Acknowledgments: The authors acknowledge funding from the Australian Research Council (ARC) Centre of Excellence for Coral Reef Studies (CE140100020), an ARC Discovery Project grant (DP140102026) and an ARC Future Fellowship (FT110100201) that provided additional support for aspects of the project.

Collection permits/ethics approval: No collection occurred in the production of this report.

Publications arising from this study:

- Pomeroy, A., Lowe, R., Ghisalberti, M., Storlazzi, C., Symonds, G. and Roelvink, D., (2017). Sediment transport in the presence of large reef bottom roughness. *Journal of Geophysical Research – Oceans*, doi:10.1002/2016JC011755
- Cuttler, M., Lowe, R., Falter, J. and Buscombe, D. (2016), Estimating the settling velocity of bioclastic sediment using common grain-size analysis techniques. *Sedimentology*. doi:10.1111/sed.12338
- Adams MP, Hovey RK, Hipsey MR, Bruce LC, Ghisalberti M, Lowe R, et al. 2016. Feedback between sediment and light for seagrass: Where is it important? *Limnology and Oceanography* 61: 1937-55
- Etminan, V., Lowe, R. and Ghisalberti, M. (2017). A new model for predicting the drag exerted by vegetation canopies. *Water Resources Research*, DOI: 10.1002/2016WR020090
- Dufois F., Lowe R.J., Branson P., Fearn P. (2017) Tropical cyclone-driven sediment dynamics over the Australian North West Shelf, *Journal of Geophysical Research – Oceans*, <https://doi.org/10.1002/2017JC013518>
- Pomeroy, A., Lowe, R., Ghisalberti, M., Storlazzi, C., Symonds, G. (2017). Spatial variability of sediment transport processes over intra- and subtidal timescales within a coral reef-lagoon system. *Journal of Geophysical Research – Earth Surface*, <https://doi.org/10.1002/2017JF004468>
- Adams, M., Ghisalberti, M., Lowe, R. et al. (2017) Modelling ecological resilience of seagrass from a sediment and light feedback. *Journal of Applied Ecology* (in revision)
- Etminan V., Lowe R. and Ghisalberti M. (2018). Predicting bed shear stresses in vegetated channels. *Water Resources Research*, 54 (11), 9187-9206

Front cover images (L-R)

Image 1: Trailing Suction Hopper Dredge *Gateway* in operation during the Fremantle Port Inner Harbour and Channel Deepening Project.
(Source: OEPA)

Image 2: Field instrumentation off northern Ningaloo Reef to quantify how reef roughness modifies sediment fluxes across reefs (image courtesy of UWA)

Image 3: Dredge Plume at Barrow Island. Image produced with data from the Japan Aerospace Exploration Agency (JAXA) Advanced Land Observing Satellite (ALOS) taken on 29 August 2010

Image 4: Flume experiments using idealized roughness to assess how canopies modify sediment transport (image courtesy of UWA).

Contents

- EXECUTIVE SUMMARY I**
- CONSIDERATIONS FOR PREDICTING AND MANAGING THE IMPACTS OF DREDGING II**
- RESIDUAL KNOWLEDGE GAPS V**
- 1 ESTIMATING THE SETTLING VELOCITY OF BIOCLASTIC SEDIMENTS USING COMMON GRAIN SIZE ANALYSIS TECHNIQUES 1**
 - 1.1 INTRODUCTION1
 - 1.2 METHODS4
 - 1.3 RESULTS9
 - 1.4 DISCUSSION.....12
 - 1.5 CONCLUSIONS.....15
 - 1.6 APPENDIX17
 - 1.7 REFERENCES18
- 2 SEDIMENT TRANSPORT IN THE PRESENCE OF LARGE REEF BOTTOM ROUGHNESS 21**
 - 2.1 INTRODUCTION21
 - 2.2 BACKGROUND: FLOW STRUCTURE AND SEDIMENT TRANSPORT WITHIN ROUGH-WALL BOUNDARY LAYERS23
 - 2.3 METHODS26
 - 2.4 RESULTS30
 - 2.5 DISCUSSION.....36
 - 2.6 CONCLUSIONS.....41
 - 2.7 REFERENCES42
- 3 HYDRODYNAMIC DRIVERS OF SPATIAL AND TEMPORAL VARIABILITY OF SEDIMENT TRANSPORT PATTERNS IN A FRINGING CORAL REEF 45**
 - 3.1 INTRODUCTION45
 - 3.2 METHODS47
 - 3.3 RESULTS52
 - 3.4 DISCUSSION.....61
 - 3.5 CONCLUSIONS.....65
 - 3.6 REFERENCES66
- 4 NEAR-BED HYDRODYNAMICS AND BED SHEAR STRESSES IN CANOPIES WITH CURRENT-DOMINATED FLOWS..... 70**
 - 4.1 INTRODUCTION70
 - 4.2 METHODS71
 - 4.3 RESULTS72
 - 4.4 DISCUSSION.....76
 - 4.5 REFERENCES77
- 5 SEDIMENT TRANSPORT IN AQUATIC CANOPIES WITH CURRENT-DOMINATED FLOWS 78**
 - 5.1 INTRODUCTION78
 - 5.2 METHODS79
 - 5.3 RESULTS81
 - 5.4 DISCUSSION.....83
 - 5.5 REFERENCES85



Executive summary

A common feature of many coastal systems is the presence of complex bottom roughness (or canopies) on the seafloor formed by a wide range of different marine communities, including seagrasses, coral reef organisms and mangroves. The health of these ecosystems can be substantially impacted by dredging plumes, through burial, light attenuation and the clogging of feeding mechanisms of individual organisms. Canopies can significantly attenuate coastal flows generated by waves and currents, resulting in large modifications to the deposition and suspension of dredging-derived sediments in these areas. Presently, however, mechanistic models of sediment transport in submerged canopies are severely lacking, and there has been no predictive capability to even estimate how dredged sediment is deposited or resuspended in these sensitive environments.

The fundamental aim of this project was to build on 'conventional' knowledge of sediment transport over bare sandy beds to develop new transport formulations applicable to a broad range of bottom types. Critically, it is shown here that conventional sediment transport models break down dramatically in canopy environments. These models typically either (1) ignore the flow attenuation provided by the canopy or (2) assign an enhanced bed stress to canopy regions (to diminish the flow), a correction which ultimately enhances sediment erosion (relative to adjacent regions without canopies). Both of these errors can result in massive over-prediction of the capacity for sediment to be mobilised within the canopy, and thus significant underestimation of the threat from dredging activities.

It is demonstrated here that to accurately predict the deposition and resuspension of sediment in canopy systems, the in-canopy (i.e. near-bed) velocity is the flow measure that most needs to be quantified. Laboratory experiments demonstrate robust predictive capacity for the near-bed velocity under both current- and wave-dominated conditions. Furthermore, thresholds for the onset of sediment motion in canopy systems can be described in terms of this near-bed velocity. Once this velocity threshold is exceeded, canopies that experience sediment deposition become regions of sediment remobilisation. Importantly, application of a threshold near-bed velocity provides significantly different (and much improved) predictions of sediment transport, compared to conventional bare bed models.

The effect of the canopy flow attenuation, which causes the in-canopy velocity to be significantly less (by up to an order of magnitude) than that in the absence of the canopy, is twofold. Firstly, suspended sediment concentrations in real canopies are seen to be significantly less than those in adjacent bare bed areas, indicative of the capacity for canopies to create strongly depositional environments. Secondly, when the canopy flow attenuation is not accounted for, predictions of sediment resuspension in canopy environments are in clear disagreement with field observations. Indeed, bed stress estimates that account for the reduced near-bed flow vastly improve the relationship between the predicted and observed grain sizes in suspension.

Key parameters of the near-bed flow that govern rates of sediment remobilisation in canopy environments (in particular the bed stress, described through the bed shear velocity, u_{*}) are also described in terms of the near-bed velocity. The physical link between the near-bed flow and sediment transport in canopy systems has allowed the prediction of rates of sediment mobilisation in canopy environments and comparison against detailed measurements in both the laboratory and the field. In a complex flow environment with mean currents, swell waves and infragravity waves, regions of rapid sediment suspension (and high suspended sediment concentrations) can be readily predicted through consideration of the canopy impact on the near-bed flow and, in turn, the impact on local bed stresses.

For accurate estimation of the impact of dredging plumes on these environments, hydrodynamically-relevant descriptors of the sediment and canopy are required. This project demonstrates that, in terms of its impact on the near-bed flow, a submerged canopy can be uniquely characterised by its roughness density (β). It is also shown that natural bioclastic sediments in these regions exhibit significant variability in density, porosity and shape. Accurate estimates of settling velocity for these sediments, which is fundamental in any description of sediment deposition, can only be made once this variation is accounted for. Pre-dredging surveys should

prioritise the evaluation of these key canopy and sediment characteristics.

Overall, by consideration and prediction of the in-canopy flow, this project provides a new capacity for the prediction of regions that are most prone to rapid rates of deposition of sediment in a dredging plume. In particular, dense canopies in low-flow environments (where the near-bed velocity or stress will often fall below the threshold value) are most at risk of rapid rates of sediment deposition. The timescale of removal of deposited sediment from these systems will be governed by rates of sediment mobilisation during high-flow periods.

Considerations for predicting and managing the impacts of dredging

Pre-development Surveys

Habitat and bathymetric mapping

Our results indicate that accurately quantifying the characteristics of benthic habitats prior to dredging operations is not only essential for predicting the impacts to benthic organisms (e.g. primary producers and filter feeders) but also critical to making robust predictions of rates of sediment transport itself, including local rates of sediment deposition, the resuspension of sediment deposits, and the large-scale (far-field) behavior of dredge plumes in these environments. These pre-development surveys could occur at two levels (depending on acceptable levels of uncertainty and available resources):

Fundamental level: The simplest set of surveys should provide basic identification and spatial extent of key benthic habitats (e.g. seagrass meadows, coral reefs and rocky reef habitats), as well as sufficiently high-resolution bathymetry to resolve the main morphological features of the habitat. Firstly, this is important given that hydrodynamic models used to predict the impact of dredged sediment should ensure they resolve the detailed bathymetry of these benthic ecosystems so they are capable of robustly predicting the spatially-variable hydrodynamic conditions (waves and currents) that drive sediment transport. For many cases, e.g. in the presence of shallow reefs, fine-scale bathymetry in these regions is critical to resolve these hydrodynamics (in some cases resolving down to scales of 10s of metres), which may best be obtained by aerial LIDAR surveys. Secondly, detailed benthic habitat surveys conducted at similar fine-scales can then be used to categorize model grid cells as containing benthic canopies or not. These regions should be initially be flagged within models as areas where there will be potentially large uncertainty in sediment transport behavior. As discussed below in 'Impact Prediction', in the simplest case sediment transport in these grid cells can be modified to account for the expected reduction in bed stresses, in order to quantitatively assess how the bottom roughness of these habitats will likely modify dredge plume behavior and rates of sediment deposition. Even in the absence of detailed information about canopy characteristics, our results suggest that reducing bed stresses by one to two orders of magnitude through a sensitivity analysis should provide an initial rough estimate of the potential impact of the canopies on the sediment transport.

Detailed level: Resources permitting, to further reduce uncertainty in sediment transport predictions within benthic ecosystems, a more comprehensive benthic mapping exercise would provide information to greatly improve the capacity to predict sediment transport in these environments. For particular benthic habitats such as seagrass meadows, canopy descriptors can be readily obtained by knowledge of the species, vegetation density and height, which allows the canopy roughness density parameter (β) to be computed that combines all of the relevant canopy geometry properties into a single parameter, and can be used to estimate the impact of a canopy the near-bed flow and bed shear stresses. Over more complex benthic habitats such as coral reefs, surveys of the detailed bottom roughness characteristics (including reef rugosity) can be recorded at fine scales using well-established measurement technologies, which can be complemented with nearbed flow measurements (as in Section 2). In addition, while it may not be practical to conduct these fine-scale surveys over the scale of an entire reef, targeted surveys could be conducted to provide some representative estimates of roughness characteristics of different reef habitat zones and use this information to infer broader scale variability in canopy roughness density throughout a reef.

Sediment sampling to determine settling velocity, density of natural sediments

Significant fractions of marine sediments in Western Australia, including in the northwest (NW WA), are comprised of calcium carbonate that is biogenically-produced by a wide range of marine organisms. As a consequence, there can be substantial variability in sediment grain properties (shape, porosity, density, etc.) that we show in Section 1 can substantially influence sediment transport (i.e. through modifications to the settling velocity). This is further confounded by the fact that there are a wide range of techniques commonly used to predict sediment grain size characteristics and settling velocity (e.g. settling tube, sieve, laser diffraction, digital image analysis) that have primarily been developed and validated for siliciclastic sediments with very different physical properties. Our analysis of carbonate sediment spanning 0.063 - 2.0 mm obtained on reefs in NW WA (Section 1) revealed that very different settling velocities are predicted when using four commonly used grain size analysis approaches. The results indicate that if sediment transport predictions are the primary motivation for conducting sediment sampling, then direct measurement of settling velocities using a settling tube is preferable. We found that the other three common grain size analysis techniques can be used to obtain robust estimates of settling velocities; however, two key issues should be carefully considered. Firstly, algorithms that we assessed in Section 1 to account for variability in particle shape were found to significantly improve the predictions of settling velocities from known grain size distribution information. Secondly, we found that wide range of sediment densities for carbonate sediment reported in the literature can have a profound effect on predicted settling velocities, and we thus recommend that the particle grain density of samples be directly measured. Our results further indicate that while the influence of particle shape was found to diminish as the grains become finer, likely due to the grains becoming increasingly spherical as they break down over time (and hence become finer), the effect of sediment density appears to remain significant even for very fine carbonate sediment.

Pre-development hydrodynamic assessments

Although hydrodynamic measurements of waves and currents are routinely conducted at sites prior to dredging, especially to support the development and validation of numerical hydrodynamic models, how and where these instruments should be deployed should be carefully considered. Typically, these hydrodynamic monitoring programs focus on observing relatively deep water depths (e.g. 10+ m depths), where in the case of NW WA, coastal flows tend to be dominated by tides and regional shelf current systems. To correctly predict the hydrodynamics within potentially impacted benthic ecosystems such as reefs this also requires direct measurements of the shallow water hydrodynamic processes that can often be driven by very different forcing mechanisms from those that occur in the deeper waters surrounding reefs. This hydrodynamic information is needed to develop more accurate reef-scale hydrodynamic models that are essential to predict the expected spatial pattern of sediment-related dredging pressures across individual reef systems. In addition, if the capability exists, detailed hydrodynamic measurements within the turbulent bottom boundary layer over benthic habitats (as in Section 2) can be used to provide direct estimates of how the local roughness reduces near-bed flows and bed shear stresses, thus providing a means to validate estimates based on assessments of canopy roughness properties and ambient (above canopy) hydrodynamics alone.

Impact Prediction

Hydrodynamic modelling of ambient currents/waves across relevant habitat scales

The large bottom roughness of benthic communities can substantially modify the circulation and distribution of wave energy in their vicinity by locally enhancing bottom drag coefficients and wave friction factors experienced by the overlying flow by an order of magnitude or greater (i.e. Sections 2 and 3). Accounting for this bottom roughness is critical to obtain robust hydrodynamic model predictions of the currents and waves within these benthic communities (including resolving the strong spatial variability that arises from habitat variability). Thus, information from habitat surveys should be incorporated into hydrodynamic model predictions to provide an accurate representation of the current and wave conditions within benthic communities, which ultimately drive sediment transport. To ensure these hydrodynamic models are correctly reproducing the spatial and temporal

variability of waves and currents across these environments, including correctly parameterizing the influence of bottom roughness, they should be rigorously validated with hydrodynamic observations obtained during the pre-development stage through hindcast simulations.

Identifying likely zones of significantly enhanced deposition

Both the field and laboratory results have demonstrated how sediment transport rates, suspended sediment concentrations and rates of resuspension are all substantially suppressed in the presence of benthic canopies, creating a relatively strong depositional environment. Canopy systems whose values of the bed shear velocity u_* are below the thresholds established here are most at risk of experiencing significant deposition. This is most likely to occur when current speeds are low, waves are small, and the canopy is tall and dense (that is, with a high value of β). Canopies that are predicted to fall below this threshold for a significant fraction of their exposure time to the dredging plume are those most at risk of harmful effects from the deposition of dredging derived sediments.

As a consequence of this work, it is clear that substantial errors will exist when applying conventional sediment transport formulations and models to predict the transport of dredged sediments in benthic communities. In particular, we show how bed shear velocities (u_*) related to bed stresses are significantly reduced when compared to values that occur in absence of the canopy, typically by an order of magnitude or larger. The application of conventional modelling approaches will thus greatly underestimate the sediment deposition that occurs within benthic canopies. It is recommended that the formulations developed here to estimate this reduction of bed shear stresses and sediment transport thresholds be considered for incorporation in sediment transport models used to predict the fate and transport of dredged sediments. At the minimum, in regions with canopy forming ecosystems, the sensitivity of sediment transport to reductions of bed shear stresses by a few orders of magnitude should be used to quantify the sensitivity of the sediment transport to this uncertainty. More detailed information about the bottom roughness characteristics obtained at the pre-development stage would enable a more accurate prediction of the reduction of bed shear stresses that can be incorporated to further reduce uncertainty in the sediment transport predictions.

This study has observed the transport of sediments in benthic ecosystems with grain sizes (D) greater than $\sim 60 \mu\text{m}$, which is coarser than the typical particle size distribution of dredge plumes in the far-field. However, the general sediment transport framework developed here to predict the impact of benthic communities on sediment deposition, transport and retention is expected to be equally relevant to dredged sediment, as the models developed are based on the general principles that are known to govern sediment dynamics. In other words, the focus was on modifying sediment transport modelling approaches initially developed for bare beds (spanning the range of sediment size fractions) as the most critical step to significantly improve predictions. As we acknowledge in Residual Knowledge Gaps (see below), there may also be some additional (unaccounted for) differences in sediment transport between bare beds and canopies that are peculiar to interactions with fine sediment (i.e. the influence of cohesive effects). While there is a well-established framework for predicting cohesive sediment transport processes in the presence of bare beds, additional work is needed to understand whether these can be directly transferred to cases where canopies are present. To achieve this, future field work would need to overcome the practical challenge of obtaining direct *in situ* measurements of sediment transport during or immediately following the impact of a dredging plume with benthic canopies.

Monitoring

Monitoring deposition in predicted 'zones of impact'

Given the expected enhancement of sediment deposition in benthic communities, monitoring efforts during dredging operations should consider deploying arrays of sediment traps (or ideally new sediment deposition sensor technology, as detailed in WAMSI Dredging Science Node Project 4.4) to obtain *in situ* measurements of rates of sediment deposition across a number of potentially impacted habitat types (even if in relatively close proximity), rather than simply focusing on distributing these sites in space. Given the higher uncertainty in sediment transport within these ecosystems, even when accounting for this roughness in modified sediment

transport formulations, this monitoring would provide an early warning mechanism if there were substantial discrepancies in modelled versus observed depositions, and also increase confidence that the effect of the bottom roughness is correctly being accounted for in earlier impact prediction modelling. Thus, efforts to monitor sediment transport in likely zones of impact during dredging operations may also benefit by weighting observations in regions with sensitive benthic communities where there will also naturally be greater uncertainty in predictions (especially if the roughness characteristics of the benthos have been poorly quantified).

Post-assessment

Recovery of dredging-impacted habitats

In the event that a benthic community such as a seagrass meadow or coral reef becomes impacted by a dredging event, the sediment transport processes governing the subsequent resuspension and potential removal of deposited sediment are equally modified by the presence of the large roughness and the associated reduction in bed shear stresses. Thus, the same general approaches and models used to predict sediment deposition discussed earlier in 'Impact Prediction' are equally applicable if the roughness characteristics of the benthos do not significantly change. This would, for example, be expected to be the case for reefs dominated by reef building corals, where the structure of the reef framework would likely not substantially change even following large scale mortality of corals. However, a key exception can be benthic habitats comprised of seagrass or macroalgae, for example, where the canopies they form may be entirely lost following mortality. In this case the loss of the roughness may result in local enhancement of bed shear stresses under the same ambient flow conditions, which will likely enhance sediment resuspension and transport to adjacent regions.

In addition, focusing on the particular case of seagrass canopies, accounting for how these canopies modify local suspended sediment concentrations and in turn light can be an important factor to consider when assessing the likelihood that seagrass meadows will re-establish and recover. From this work (Publication 7.3), we have highlighted that there can be a strong feedback loop between seagrass density, suspended sediment concentrations and light levels. The resilience of seagrass meadows under chronic exposure to dredging plumes would thus, in part, be regulated by this feedback loop and should be considered. For example, seagrass canopies in clear (oligotrophic) waters that are exposed to a wide sediment size distribution in high flow conditions are most likely to be at risk of irreversible adverse effects as a result of chronic exposure to dredging plumes. Therefore, managing the exposure of these canopies to substantial impacts to dredging plumes would likely be much more important.

Residual Knowledge Gaps

Expanded classification of dredge-generated carbonate sediments

The detailed assessment and inter-comparison of analysis techniques to classify sediment grain characteristics (specifically the settling velocity) focused on natural reef carbonate sediments spanning the coarse silt (0.063 mm) to coarse sand size fractions (2.0 mm). While we have no reason to believe that dredge-generated carbonate sediments would behave substantially different at similar size fractions, further work could be conducted to confirm this (i.e. by conducting experiments with samples collected in dredge hoppers). In addition, although the discrepancies between the techniques diminished as sediment size decreased, the potential effect of sediment grain density appeared to be present across all size ranges. Further work is needed to understand how the sediment grain (particle) density in particular varies for given sediment types over a wide range of size fractions (including over the entire finer silt fraction), including whether mechanical production of dredged sediment alters these relationships in any way. Lastly, our work in Section 1 highlighted the substantial discrepancies in the reported and assumed densities for carbonate sediments reported in the literature, and in particular the relationship between particle and bulk densities. Further work is needed to more clearly define how particle and bulk densities are inter-related for carbonate sediments, which is critical to be able to accurately relate mass fluxes of deposited sediment (as output from predictive models) to rates of vertical sediment deposition.

Field quantification of rates of deposition across different habitats

This project has provided some of the first quantitative measures of how the presence of benthic canopies can regulate sediment transport processes by modifying the near-bed mean and turbulent flow properties, and the first field-based studies to accurately quantify and predict these dynamics in natural ecosystems. While considering these processes would already be a significant advance in modelling studies to predict the impact of dredging on sensitive benthic ecosystems, this new area of research is admittedly still in its infancy and there is considerable scope for further research to develop and validate improved knowledge and models to further reduce uncertainty. Additional work is needed to quantify these hydrodynamic and sediment transport models more comprehensively over an even wider range of benthic community and habitat types. While the intensive studies in the field needed to achieve this can require substantial resources, many of the experimental approaches and techniques that have been developed in this project can now be more readily applied in future studies with confidence. Over time, as additional data are obtained (including by the broader international community) over a wider range of habitats and hydrodynamic regimes, this will provide the greatest opportunity to further refine models and improve their accuracy. In addition, given the resources available to the project and logistical limitations, the project focused on producing generalised process-understanding of the sediment transport processes by studying natural coral reef and seagrass meadows. While it was not directly possible to apply these concepts to a benthic community directly impacted by a dredging plume, if opportunities and permissions exist, future work should target these studies in advance for communities that are known to be at high risk from future dredging operations.

Cohesive effects

The field and laboratory components of this study have examined the transport of sediments that are sufficiently large for cohesive effects (due to both physico-chemical and biologically-mediated processes) to be negligible. In both settings, it is easier to work with sand-sized particles to develop the critical process-based understanding of sediment transport in these complex environments. However, for sediment in dredge plumes, cohesive forces can lead to flocculation of sediments (altering their effective size distributions), which is particularly relevant to predicting the broader behaviour of these plumes. There would therefore be benefit from additional work to understand the role of cohesive effects of fine dredged sediment (i.e. mud) once it has been deposited within a benthic canopy, and in particular how this modifies the resuspension thresholds for canopies that have been proposed here. Fortunately, there is already a large body of knowledge of cohesive sediment transport in the absence of canopy that would provide a foundation for further work. Given the major differences in the near-bed hydrodynamic processes in the presence of canopies, it presently remains unclear whether this existing knowledge can be extrapolated to benthic communities by simply accounting for the reduction of bed shear stresses by the canopy

1 Estimating the settling velocity of bioclastic sediments using common grain size analysis techniques¹

Abstract

Most techniques for estimating settling velocities of natural particles have been developed primarily for siliciclastic sediments. Therefore, to understand how these techniques apply to bioclastic environments, measured settling velocities (w_s) of bioclastic sedimentary deposits sampled from a nearshore fringing reef in Western Australia were compared with settling velocities calculated using results from several common grain size analysis techniques (sieve, laser diffraction and image analysis) and established models. The effects of sediment density and shape were also examined by using a range of density values and three different models of w_s . Sediment density was found to have a significant effect on calculated w_s , causing a range in root-mean-square error of up to 28% depending upon settling velocity model and grain size method. Accounting for particle shape reduced errors in predicted w_s by 3% to 6% and removed any velocity-dependent bias, which is particularly important for the fastest settling fractions. When shape is accounted for and measured density is used, root-mean-square error is 4%, 10%, and 18% for laser diffraction, sieve, and image analysis, respectively. The results of this study show that established models of w_s that account for particle shape can be used to estimate settling velocity of irregularly-shaped, sand-sized bioclastic sediments from sieve, laser diffraction, or image-analysis-derived measures of grain size with a limited amount of error. Collectively, these findings will allow for grain size data measured with different methods to be accurately converted to settling velocity for comparison. This will facilitate greater understanding of the hydraulic properties of bioclastic sediment which will increase our general knowledge of sediment dynamics in these environments.

1.1 Introduction

Settling velocity in water is a fundamental physical property of sediments, which can be used to understand how sediment is entrained, transported and deposited in marine environments (Miller et al., 1977; Komar and Clemens, 1986; Le Roux, 2002; Paphitis et al., 2002). Settling velocity is key to understanding both the hydrodynamic properties of bed sediment, and thus transport mode and/or entrainment thresholds (Shields, 1936; Rouse, 1937), as well as sedimentary plume dynamics, where settling velocity determines sediment fall-out times and advection length scales (Syvitski et al., 1988). Furthermore, this can be of particular importance in environments such as estuaries, where deposition of suspended material can lead to harmful build-ups of heavy metals (Birch and Taylor, 1999); or in coral reefs, where increased turbidity can limit light availability (Storlazzi et al., 2015) and lead to coral stress and/or mortality (Rogers, 1990).

The settling velocity of a particle is determined by its size, shape and density. These variables have been empirically related for straight-forward conversion from grain diameter, a commonly measured parameter, to settling velocity (Gibbs et al., 1971; Dietrich, 1982; Le Roux, 1992; Cheng, 1997; Le Roux, 2002; Ferguson and Church, 2004). Although each model accounts for particle size and density, each has a different treatment of particle shape. For example, the Gibbs et al. (1971) relationship, makes no correction for grain shape, accounting only for sediment density and size; Ferguson and Church (2004) use two constants in their equation that are related to grain shape; and Dietrich (1982) explicitly accounts for grain shape through the Corey (1949) shape factor (CSF) and grain roundness through the Powers (1953) roundness index (PRI).

These equations have been developed and tested principally for siliciclastic sediments; however, it remains

¹ Published as Cuttler, M. V., Lowe, R. J., Falter, J. L., & Buscombe, D. (2017). Estimating the settling velocity of bioclastic sediments using common grain-size analysis techniques. *Sedimentology*. 64 (4), 987-1004

unclear how accurate these equations are when applied to bioclastic sediment which is typically highly irregular in shape and density. Bioclastic sediment is derived from the physical and chemical breakdown of biogenic structures (e.g. coral reefs) and the death of organisms (e.g. foraminifera, molluscs, calcareous algae (e.g. *Halimeda spp.*), etc.). These sediment sources have direct influence on particle morphologies, sizes, and densities present in the sediment pool as organisms build skeletons with specific porosities, and therefore densities, and break down into characteristic shapes and sizes (Sorby, 1897; Perry et al., 2011). For example, *Halimeda* and mollusc fragments tend to form plate-like particles, urchin spines will form rod-like particles, foraminifera will generally form disc-like particles, and most corals and coralline algae will form irregular, block-like particles (Maiklem, 1968; Braithwaite, 1973). Because these irregularities make it difficult to derive a characteristic grain diameter for bioclastic deposits using common grain size techniques (see below), settling velocity has been suggested to be a more meaningful metric for interpretation of bioclastic sedimentary deposits (Kench and McLean, 1996). Although, settling tube is the primary method for analysing settling velocity of bulk samples, not all laboratories have this equipment; therefore, other common grain size methods have been applied to bioclastic environments (Folk and Robles, 1964; Harney et al., 2000; Larcombe et al., 2001). Thus, there is a clear need to understand how accurately results from common grain size techniques can be converted to settling velocities using established empirical models.

Common methods to measure grain size distributions (GSDs) include: sieves; laser diffraction; and image analysis. Sieve analysis involves sorting sediment particles through a series of square-mesh screens, whereby it is assumed that the particles are spherical with a diameter corresponding to the length of the side of the square sieve openings (Komar and Cui, 1984). As particles become more irregular (i.e., less spherical), the length of a grain's intermediate (second largest) axis relative to the length of the diagonal of the square sieve opening determines passage of the grain through the sieve (Rittenhouse, 1943; Komar and Cui, 1984). Laser diffraction measures a grain's 'nominal' diameter, or the diameter of a sphere with the same volume and of the same material as the measured grain, based on the forward scattering of a parallel beam of monochromatic light, with scatter angle and intensity related to grain size by a specific optical model (Cheetham et al., 2008). Thus, like sieving, grain sizes derived from laser diffraction provide idealised, scalar value representations of the actual three-dimensional irregularity of natural sediments. Image analysis estimates GSD from an image of sediment in one of two ways: 1) so-called 'geometrical' methods (cf. Buscombe et al., 2010), which measure the apparent grain axes of each individual grain using image-segmentation techniques (Sime and Ferguson, 2003; Graham et al., 2005; Graham et al., 2010; Chang and Chung, 2012;); and 2) statistical methods, which measure GSD based on spatial autocorrelation (Rubin, 2004; Barnard et al., 2007; Buscombe, 2008; Buscombe and Masselink, 2009; Warrick et al., 2009; Gallagher et al., 2011; Cheng and Liu, 2015) or spectra of image intensity (Buscombe et al., 2010; Buscombe and Rubin, 2012). However, each of these forms of image analysis has limitations. Geometrical methods, based on edge-detection and segmentation of individual grains, often have difficulty resolving overlapping grains, or touching grains of similar colour or shade, which can lead to over- and under-segmentation of grains, and thus, has so far made a universally applicable edge-detection algorithm elusive (see review by Buscombe, 2013). Conversely, some statistical methods have relied on the time-consuming generation of a site-specific reference image catalogue prior to analysis (Rubin, 2004; Barnard et al., 2007; Buscombe, 2008; Buscombe and Masselink, 2009; Warrick et al., 2009; Gallagher et al., 2011; Di Maria et al., 2016) or otherwise only provide the mean and/or sorting coefficient rather than the full GSD (Buscombe et al., 2010; Buscombe and Rubin, 2012). Buscombe (2013) proposed a statistical method based on wavelet analysis that estimates the full GSD, without the need to isolate and segment each grain, and without the need for site-specific calibration. To the authors' knowledge, this method has been tested only on siliciclastic sediment (Buscombe et al., 2014; King et al., 2016).

Sieving and laser diffraction methods assume that particles are spherical and of uniform density (McCave and Syvitski, 1991). Although either or both of these assumptions may often be valid in siliciclastic environments, they are both almost always violated in bioclastic environments (e.g., coral reefs), where sediment is largely derived from calcifying organisms (corals, coralline algae, foraminifera, molluscs, etc.) with variable shapes (rods, disks, plates) and densities (Maiklem, 1968; Braithwaite, 1973). Previous methodological comparisons using

siliciclastic sediment have shown that sieve and settling tube produce nearly identical GSDs when deposits are well-sorted (Komar and Cui, 1984); sieve and laser diffraction yield similar GSDs for sand-sized material (Cheetham et al., 2008; Di Stefano et al., 2010); and image analysis can produce GSDs within 4% of those measured by sieve and settling tube (Barnard et al., 2007; Gallagher et al., 2011; Buscombe et al., 2014). However, comparative studies in bioclastic environments have suggested that sieves can yield significantly larger mean grain size estimates (up to 300%) than settling tubes for coarse samples (mean > 1 mm), smaller mean grain size estimates in fine samples (mean < 1 mm; Kench and Mclean, 1997), and that the relationship between sieve and settling tube can be significantly non-linear (Smith and Cheung, 2002). These differences can cause misinterpretations of transport pathways and deposit-forming processes in bioclastic environments (Kench and Mclean, 1996, 1997).

There remains a gap in the sedimentological literature concerning how results from more modern methods (such as laser diffraction and image analysis) relate to more classic grain size methods (sieve and settling tube) for bioclastic sediments. This is particularly important given that the more modern methods are usually less time consuming, achieve greater detail and more accurate analysis of finer material, and, for image analysis, can be conducted *in situ*, obviating the need for sample collection and storage; both of which facilitate higher rates of spatial and temporal sampling (Barnard et al., 2007; Gallagher et al., 2011; Buscombe et al., 2014) and hence may yield greater insight into sediment dynamics. Furthermore, it is poorly understood how common settling velocity models, developed from experiments on siliciclastic particles, perform for more irregular, bioclastic sediment. Here, we address these gaps by 1) measuring the GSDs of bioclastic sediment from a nearshore reef environment on the northwest coast of Australia using three common methods (sieve, laser diffraction and image analysis); 2) calculating settling velocities from the resulting GSDs according to three different models as developed by Gibbs et al. (1971), Dietrich (1982), and Ferguson and Church (2004); and 3) comparing these results against direct measurements of settling velocities. This study will further our understanding of sediment dynamics in bioclastic environments by allowing for conversion of existing grain size distributions to settling velocities and thus allowing for the hydrodynamic properties and transport modes of grains to be established.

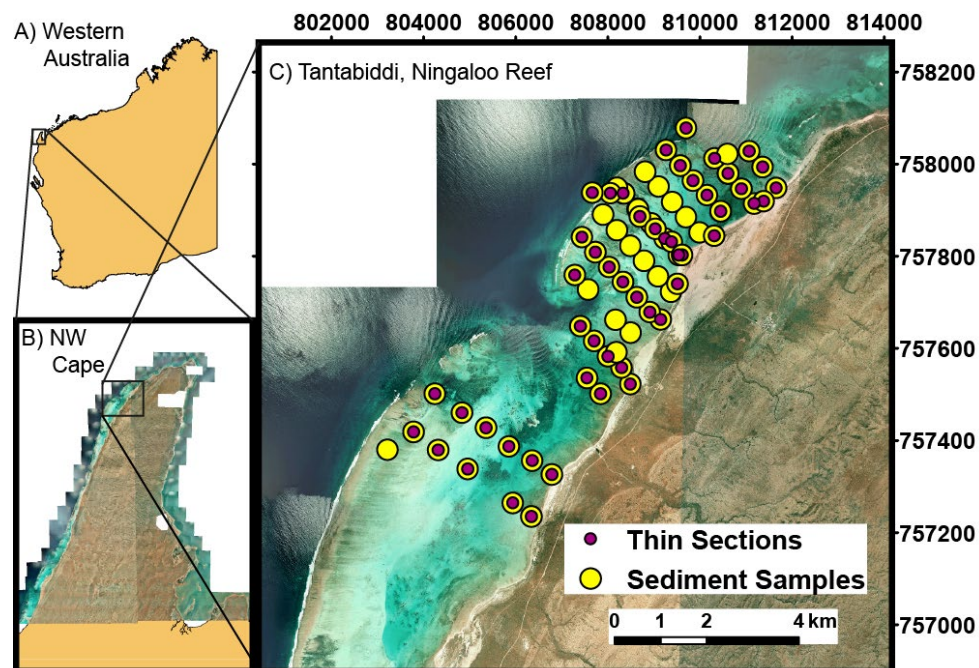


Figure 1.1. Map of (A) Western Australia, (B) the northwest (NW) cape of Western Australia, and (C) the study site at Tantabiddi, Ningaloo Reef, Western Australia. Aerial imagery is from the SLIP Portal by the Western Australian Land Information System (WALIS) and Landgate (<https://www2.landgate.wa.gov.au/>). White areas in C are due to lack of coverage in the aerial imagery.

1.2 Methods

Study area

'Natural' ($n = 73$) and 'standard' ($n = 2$) sediment samples were used in this analysis. The 73 natural samples were collected from Tantabiddi, Ningaloo Reef, Western Australia (21.8714°S , 113.9903°E ; Figure 1.1). Approximately 500 g samples were collected from the top 5-7 cm of the seabed at each site. The standard samples were well-rounded, quartz-based sand ($D_{50} \sim 0.3$ mm) and CaribSea Aragamax™, an oolitic aragonite sand ($D_{50} \sim 0.5$ mm).

This study focused on the sand fraction (0.063 – 2 mm) only. Therefore, all samples were washed over a $63 \mu\text{m}$ sieve and dried to remove silt and clay-sized grains ($\leq 1\%$); a riffle splitter was then used to generate five statistically equivalent sub-samples. Each of the four grain size methods (sieve, settling tube, laser diffraction, and image analysis) was used on one of the sub-samples to determine the GSD, and the last sub-sample was used to determine the composition of each sample.

Sub-samples for compositional analysis were embedded in epoxy and thin-sectioned (Figure 1.2); composition was then determined by identifying a minimum of 300 grains using a petrographic microscope. Grains were divided into 8 categories: coral, coralline algae, foraminifera, mollusc, echinoderm, quartz, framework, and other.

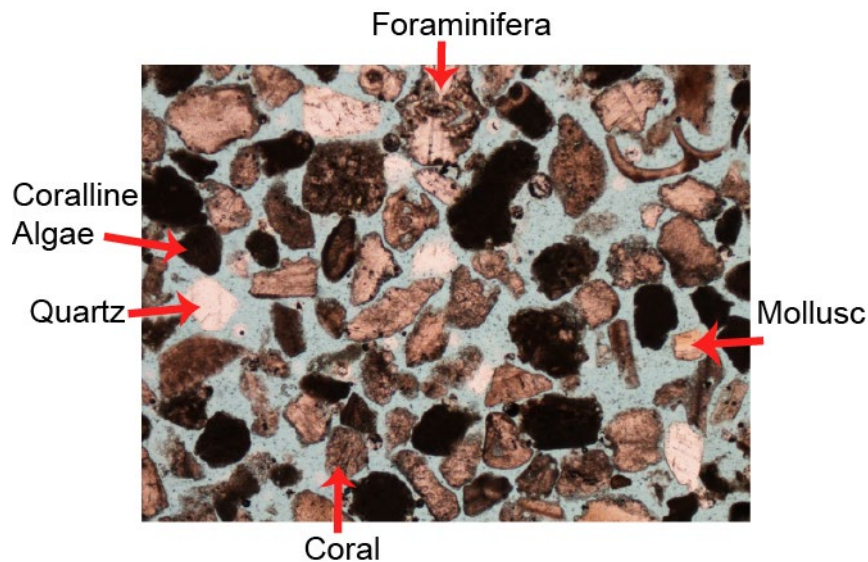


Figure 1.2. Example thin section image used in constituent assemblage analysis. Coral, coralline algae, quartz, mollusc and foraminifera fragments are highlighted.

GSDs were determined using the modified geometric method of Folk and Ward (1957) for sieve, laser diffraction, and image analysis (Blott and Pye, 2001); median grain size (D_{50}) was then converted to settling velocity for comparison with measured settling velocities. Normalized root-mean-square error (RMSE) and mean absolute error (MAE) were used to compare between results for all the various methods.

$$RMSE(\%) = \frac{\sqrt{\frac{\sum [(Measured - Estimated)^2]}{n}}}{Measured_{max} - Measured_{min}} \quad (0.1)$$

$$MAE(\%) = \frac{\frac{1}{n} \sum (|Measured - Estimated|)}{Measured_{max} - Measured_{min}} \quad (0.2)$$

Sediment density measurements

There exists a wide range of sediment density values in the carbonate sediment literature; which is primary due to the type of density measured (Table 1.1). Whereas each type of density reported in Table 1 has a specific application (see Discussion), for sediment transport applications and settling velocity calculations it is appropriate to use the ‘particle density’ (ρ_{part}), which corresponds to the particle’s specific gravity (Gibbs et al., 1971; Komar, 1981; Ferguson and Church, 2004) when all intragranular pore spaces of the particle are filled with water (Smith and Cheung, 2003). To directly measure ρ_{part} , we employed a method similar to the American Society for Testing and Materials’ method for measuring specific gravity (ASTM International, 2010).

Table 1.1. Summary of sediment density values found in the literature. *range includes measurements on specific sediment constituents

Author	Sediment density (g cm-3)	Sediment composition	Type of Density Measured
Berthois and Calvez (1960)	1.16	Foraminifera	Effective density
Jell et al. (1965)	1.6 to 2.9 *	Foraminifera, coral, green/red calcareous algae	Particle density
Berger and Piper (1972)	1.5	Planktonic foraminifera	Effective density
Neuman and Land (1975)	1.15	Calcareous algae and ‘lime mud’	Bulk density
Land (1979)	1.35	Calcareous ooze, Halimeda-rich mud, foraminifera-rich sand	Bulk density
Fok-Pun and Komar (1983)	1.48	Foraminifera	Effective density
Sadd (1984)	1.5	Coral, molluscs, foraminifera, echinoids, coralline algae	Bulk density
Hubbard et al. (1990)	1.2	Coral, molluscs, foraminifera, echinoids, coralline algae	Bulk density
Kench and McLean (1997)	1.85	Coral, coralline algae, alcyonarian spicules, crustaceans, echinoids, Halimeda, foraminifera, molluscs	Particle density
Michels (2000)	1.73	Foraminifera	Effective density
Paphitis et al. (2002)	2.72 to 2.80 *	Mollusc shells	Particle density
Smith and Cheung (2003)	2.59 to 2.78	Foraminifera, coralline algae, molluscs, corals, echinoids, Halimeda	Particle density
Harney and Fletcher (2003)	0.7 to 1.56 *	Coral, coralline algae, Halimeda, foraminifera, Molluscs	Bulk density
Morgan and Kench (2014)	1.85	Coral, coralline algae, Halimeda, molluscs	Particle density
This study	2.51 to 2.76	Coral, coralline algae, molluscs, foraminifera	Particle density

Approximately 50 g of sediment was combined with fresh water at a known temperature in a 100 mL volumetric flask and then the solution was sonicated for 1 hr (as opposed to boiled) to remove entrapped air. Particle density was then calculated as:

$$\rho_{part} = \frac{M_s T}{M_s + M_{FW} - M_{FSW}} * \rho_{water} \quad (0.3)$$

where M_s is the mass of dry sand, T is a correction factor based on the temperature of water, M_{FW} is the mass of the volumetric flask filled with water, M_{FSW} is the mass of the volumetric flask with both sand and water, and ρ_{water} is the standard density of fresh water at 20 degrees Celsius (i.e. 1 g cm^{-3}).

ρ_{part} was measured for 20 natural (bulk) sediment samples spanning the range of sub-reef sampling sites; these 20 values were then averaged to calculate a representative ρ_{part} for all natural samples. Similarly, ρ_{part} was measured, and then averaged, for two sub-samples of each standard (the quartz sand and the aragonite sand). As there exists a range of sediment density values reported in the literature, even for the same types of measured densities (Table 1.1), it is necessary to understand the contribution to error in calculated w_s due to specification of sediment density. Therefore, settling velocities were calculated not only using the measured ρ_{part} values, but also using 1.2 g cm^{-3} (at the lower-end of densities reported for carbonate sands) and 1.85 g cm^{-3} (a mid-range density).

Sieve

Approximately 70 g of sediment was analysed through a sieve stack ranging from 4 phi (0.063 mm) to -1 phi (2 mm) at 0.5 phi intervals (i.e., 11 sieve fractions). Samples were sieved in a mechanical sieve shaker for 15 min, which was sufficient time to allow complete separation into size classes (Román-Sierra et al., 2013). Sediment trapped on each sieve screen was collected and weighed to calculate the GSD.

Settling Tube

Settling tube analysis was conducted in a 24-cm diameter, 212-cm tall water column. Between 15 and 20 g of sediment was wetted to a sample plate and attached to a magnetic holder above the water column. An external trigger was used to simultaneously lower the plate into the water, thus releasing the sediment, and starting the timer. Each run lasted 10 min, which was sufficient time to measure the fall velocities of the finest material of interest ($\sim 0.063 \text{ mm}$), with the cumulative mass recorded at 1 Hz. The balanced used was accurate to $\pm 0.05 \text{ g}$ (± 1 standard deviation); which corresponds to $\pm \sim 0.02 \text{ cm s}^{-1}$ for measured w_s .

Laser Diffraction

A Malvern Mastersizer 2000 (Malvern Instruments Ltd, Malvern, United Kingdom) was used for laser diffraction (LD) analysis (Cheetham et al., 2008; Di Stefano et al., 2010). Prior to analysis, samples were sieved through a 0 phi (1 mm) sieve, then added to a solution of 10 mL of alkaline sodium hexametaphosphate and 800 mL of deionised water, and then ultrasonically stirred for 30 s (Di Stefano et al., 2010). Because sample preparation removed material $> 1 \text{ mm}$, only samples that had no fractions coarser than 1 mm from sieve analysis were used for comparison. LD converts optical scatter to GSD using a specified optical model; however, selection of a particular optical model has been shown to have negligible effects on results for sand-sized particles (Blott and Pye, 2006). Therefore, GSDs were calculated using Mie theory and the refractive index of either aragonite (i.e., 1.53 for the natural and aragonite sands) or quartz (i.e., 1.46 for the quartz sand).

Image analysis

Images of sediment samples were collected using a Canon EOS 5D Mark II, fitted with a 65-mm macro lens. Sediment samples were arranged on a fixed stage and manually flattened; this meant that the image plane was parallel to the object plane, and therefore, spatial resolution was uniform over the entire image and a single conversion factor (0.0062 mm/pixel) could be used to convert GSD results from pixels to mm (Barnard et al., 2007; Gallagher et al., 2011; Buscombe, 2013). Previous tests of image analysis (IA) have shown that errors are

reduced if multiple images are taken and then averaged; therefore, in this study a total of 20 images were taken for each sample (Barnard et al., 2007; Gallagher et al., 2011; Buscombe, 2013).

A Matlab program implementing the algorithm of Buscombe (2013), 'Digital Grain Size' (DGS), was used to process the images. The method of Buscombe (2013) approximates the GSD using the global power spectral density function derived using a Morlet wavelet. When using DGS, there are various options for image processing; the first option is the region of interest (ROI) used to calculate the GSD. The user is allowed to specify the entire image as the ROI or to use a subsection, or multiple subsections of the image as ROIs. To determine which was most appropriate, a series of tests were performed using the whole image as the ROI, multiple non-overlapping equal-area ROIs, and multiple overlapping equal-area ROIs (Figure 1.3).

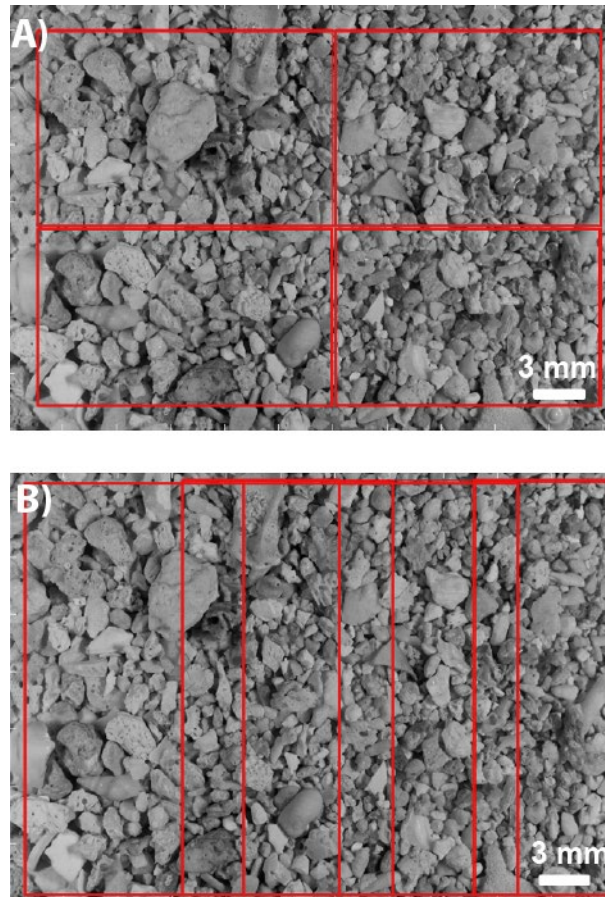


Figure 1.3. Examples of (A) non-overlapping regions of interest (ROI) and (B) overlapping ROIs (~30% overlap) used when calculating grain-size distributions with the digital grain-size graphical user interface (DGS GUI) from Buscombe (2013).

Other options in DGS include 'flattening' the image, which is a Savitsky-Golay high-pass filter (Savitzky and Golay, 1964) and can help to eliminate errors that are introduced by non-uniform lighting conditions, lens curvature, or the sediment surface being non-parallel to the image plane. These optical artefacts are picked up by spectral analysis as spuriously high variance at wavelengths greater than any grain length scale, which can lead to over-estimates of grain size. In order to test the potential effects of this, the algorithm was run with and without flattening the image. To ensure the algorithm was producing realistic results, a manual 'point count' was conducted on 10 samples following the method of Barnard et al., (2007) and compared to DGS results, which has become a standard way to evaluate the image-derived grain size estimates with a completely equivalent metric (Warrick et al., 2009; Buscombe et al., 2010; Buscombe and Rubin, 2012; Buscombe, 2013; Buscombe et al., 2014).

The results of DGS are an area-by-size measure of grain diameter, whereas, sieve, laser diffraction, and settling tube are a volume- or mass-by-size measure. Although these two measures of grain diameter are not directly

comparable, there exists a common method to convert from areal- to volume-based measures of grain size (Diplas and Sutherland, 1988; Graham et al., 2005, 2012)

$$p(V-W)_i = \frac{p(S)_i * D_i^x}{\sum p(S)_i * D_i^x} \quad (0.4)$$

where $p(V-W)_i$ is the volume-by-weight proportion of the i -th size fraction, $p(S)_i$ is the image-derived areal proportion of the i -th size fraction, D_i is the grain size of the i -th size fraction, and x is a conversion constant. Diplas and Sutherland (1988) suggest x should vary between 0 and -1 depending upon porosity (with $x = -1$ when porosity = 0%). According to Diplas and Fripp (1992), it is necessary to use different values for exponent x depending on grain size, but a pragmatic approach is to use an average value for x , which is determined empirically (Diplas et al., 2008). The data from Diplas and Sutherland (1988) suggests $x = -0.47$ for natural sediments with ~33% porosity; therefore, when converting to volume-by-size proportions we tested both $x = -0.5$ and $x = -1$.

Conversion to settling velocity

The equations from Gibbs et al., (1971), Dietrich (1982) and Ferguson and Church (2004) were used to convert grain size results to settling velocities. The equation from Gibbs et al., (1971) (hereafter, 'Gibbs') only accounts for particle size and ρ_{part} :

$$w_s = \frac{-3\mu + \sqrt{9\mu^2 + gr^2\rho(\rho_{sg} - \rho)(0.015476 + 0.19841r)}}{\rho(0.011607 + 0.14881r)} \quad (0.5)$$

where μ is kinematic viscosity of water, g is gravitational acceleration, r is grain radius, and ρ is fluid density; therefore, measured ρ_{part} and D_{50} values were used for sieve, laser diffraction, and image analysis.

The equation from Dietrich (1982) (hereafter, 'Dietrich'), requires ρ_{part} , the Corey (1949) shape factor (CSF) and the Powers (1953) roundness index (PRI) to determine settling velocity (Eq. (0.4)):

$$w_s = R_3 10^{R_1 + R_2} \quad (0.6)$$

where R_1 , R_2 , and R_3 are fitted equations correcting for particle density, shape and roundness, respectively (see Appendix for equations). While the measured ρ_{part} and the suggested PRI for natural particles (i.e., 3.5) were used for both the standard and natural samples, 0.7 and 0.55 were used for CSF for the standard and natural samples, respectively. CSF for the standard samples is the value suggested by Dietrich (i.e., 0.7); whereas 0.55 is the average CSF determined by Smith and Cheung (2003) for reef-derived material. Dietrich is valid only when nominal diameters (D_n) are used for grain size. Therefore, the sieve and image analysis results required conversion to D_n whereas LD was directly applicable. Smith and Cheung (2002) proposed an empirical equation to convert sieve-derived D_{50} to D_n for carbonate material ($D_n = 1.18 * D_{50}$); given that IA is comparable to sieve diameters after conversion to volume-by-size diameters (Kellerhals and Bray, 1971; Diplas and Sutherland, 1988) this equation was used to calculate D_n for both sieve and image analysis results.

Finally, we evaluated the settling velocity equation proposed by Ferguson and Church (2004) (hereafter, 'F&C'):

$$w_s = \frac{(\rho_{part} - \rho)gD^2}{C_1\nu + (0.75C_2(\rho_{part} - \rho)gD^3)^{0.5}} \quad (0.7)$$

where D is either sieve or nominal diameter, and C_1 and C_2 are constants determined by particle shape. F&C

suggest values of C_1 and C_2 should be 18 and 0.4, respectively, for smooth spheres; 18 and 1, respectively, for natural sands if sieve diameters are used; 20 and 1.1, respectively, for natural sands if D_n is used; and 24 and 1.2, respectively, for very angular grains. We set C_1 and C_2 equal to 20 and 1.1, respectively, and used the same grain diameters as were input to Dietrich (i.e., D_n).

1.3 Results

Sediment density and compositional analysis

There is some variability in constituent assemblage across sub-reef environments (i.e., reef crest, reef flat, lagoon) at Ningaloo; however, Ningaloo sands are predominantly composed of coral fragments, coralline algae, and molluscs (Table 1.2; Cuttler et al., 2015).

Table 1.2. Constituent assemblages for bulk sediment samples from the sub-reef environments at Tantabiddi, Ningaloo Reef.

Constituent	Reef Crest (%)	Reef Flat (%)	Lagoon (%)	Channel (%)	Beach (%)
Coral	37	38	36	27	33
Coralline algae	21	19	16	17	14
Mollusc	22	20	19	21	24
Foraminifera	8	7	7	5	6
Echinoderm	1	1	1	0	1
Framework	5	3	4	2	4
Quartz	5	5	16	28	18
Other	1	1	1	1	1

Table 1.3. Root-mean-square error (RMSE) for (A) sieve, (B) laser diffraction and (C) image analysis due to sediment density for each settling velocity equation.

A)	Sieve	Sediment Density		
	Settling Velocity Equation	1.2 g cm ⁻³	1.85 g cm ⁻³	2.6 g cm ⁻³
	Gibbs et al. (1971)	35 %	18%	11%
	Dietrich (1982)	37%	21%	10%
	Ferguson and Church (2004)	36%	19%	8%
B)	Laser Diffraction	Sediment Density		
	Settling Velocity Equation	1.2 g cm ⁻³	1.85 g cm ⁻³	2.6 g cm ⁻³
	Gibbs et al. (1971)	14%	2%	10%
	Dietrich (1982)	16%	6%	4%
	Ferguson and Church (2004)	16%	5%	6%
C)	Image Analysis	Sediment Density		
	Settling Velocity Equation	1.2 g cm ⁻³	1.85 g cm ⁻³	2.6 g cm ⁻³
	Gibbs et al. (1971)	28%	8%	24%
	Dietrich (1982)	31%	11%	18%
	Ferguson and Church (2004)	30%	10%	21%

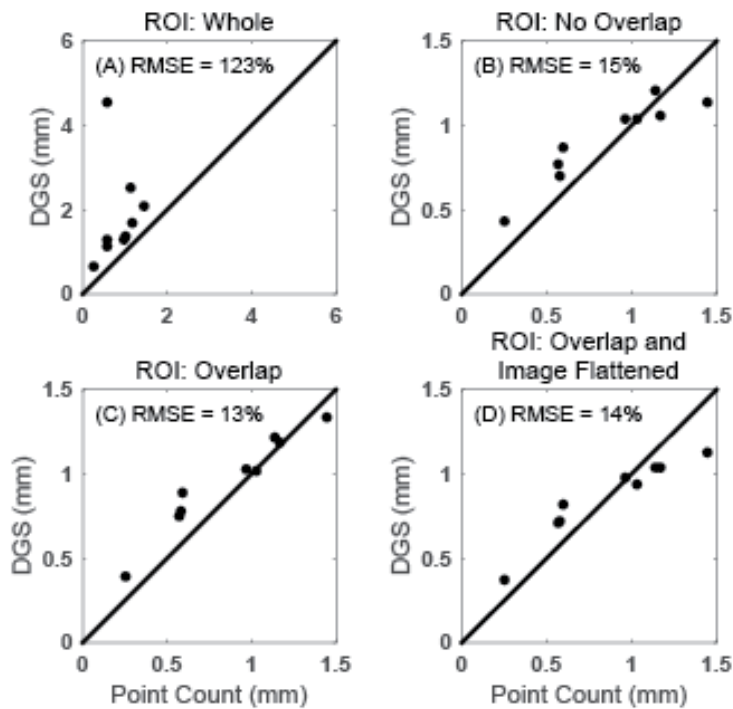


Figure 1.4. Comparison of digital grain-size (DGS) algorithm from Buscombe (2013) with manual point count results for D_{50} when region of interest (ROI) is set to (A) the whole image, (B) multiple, non-overlapping regions, (C) multiple, overlapping regions, and (D) multiple, overlapping regions with image flattening.

Measured ρ_{part} for the natural, bioclastic sediments was $2.58 \pm 0.02 \text{ g cm}^{-3}$ (mean ± 1 standard deviation) and showed no relationship with median settling velocity (slope = -0.002 ± 0.004 , $\alpha = 0.05$, $p = 0.34$). Measured ρ_{part} for the standard quartz and aragonite sands were $2.64 \pm 0 \text{ g cm}^{-3}$ and $2.71 \pm 0.05 \text{ g cm}^{-3}$, respectively.

Varying ρ_{part} from 1.2 g cm^{-3} to 2.6 g cm^{-3} caused a 22% to 28% change in RMSE for sieve results; an 11% to 12% change in RMSE for laser diffraction; and a 20% change in RMSE for image analysis (Table 3).

Comparison of methods

Selection of 'Digital Grain Size' region of interest and conversion to volume-by-size

Estimated GSDs from each analysis consisting of different ROIs were tested against manual point count results to determine the most suitable ROI. RMSE progressively improved as the number of ROIs and amount of overlap increased (

Figure 1.4). Image flattening, however, caused a slight increased RMSE; therefore, we used overlapping ROIs (~30% overlap) without image flattening because this yielded the lowest RMSE (13%) when compared to manual point counts.

Results of converting image analysis grain sizes from area-by-size to volume-by-size are presented in Fig 1.5. When compared to sieve analysis, an equivalent measure of grain size, RMSE is 28% and 16% when x is set to -

0.5 and -1, respectively; therefore, we used -1 for x in Eq. (0.4).

Comparison of settling velocity equations

The results of calculated w_s using the three selected equations versus measured w_s using the settling tube are shown in Figure 1.6. Settling velocities calculated from image analysis (

Figure 1.6C) have the highest MAE and RMSE, with a maximum of 22% and 24%, respectively. MAE and RMSE from laser diffraction varied from 2% to 6% and 4% to 10%, respectively, for Gibbs, Dietrich, and F&C (

Figure 1.6B); whereas MAE and RMSE from sieve diameters varied from 6% to 9% and 8% to 11%, respectively, for Gibbs, Dietrich, and F&C (

Figure 1.6A).

Although Gibbs predicts w_s with comparable RMSE to Dietrich and F&C, there is a clear trend of increasing over-prediction of w_s with increasing observed w_s for sieve and laser diffraction (

Figure 1.6A,B). Furthermore, whereas the relationships between observed and estimated w_s for sieve and laser diffraction are linear (

Figure 1.6A,B), the same relationships for IA (

Figure 1.6) are nonlinear, showing maximum discrepancy at mid-range w_s . These trends are consistent for all tested values of ρ_{part} ; however, the variability in RMSE between settling velocity models for measured ρ_{part} (3% to 6%) is much smaller than the range in RMSE caused by varying ρ_{part} for a given grain size method and settling velocity model (Table 1.3).

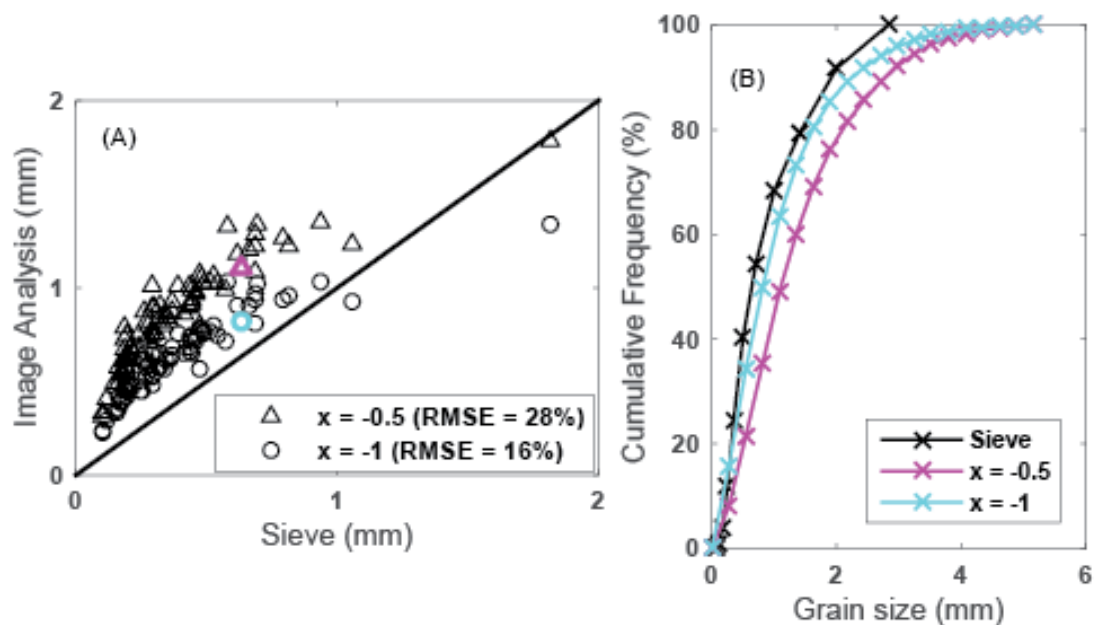


Figure 1.5. (A) Comparison of volume-by-size image analysis D50 with sieve D50; squares and circles denote -0.5 and -1, respectively, for the value of x in Equation 2. (B) Cumulative frequency curves for sieve, $x = -0.5$, and $x = -1$ for sample highlighted in (A).

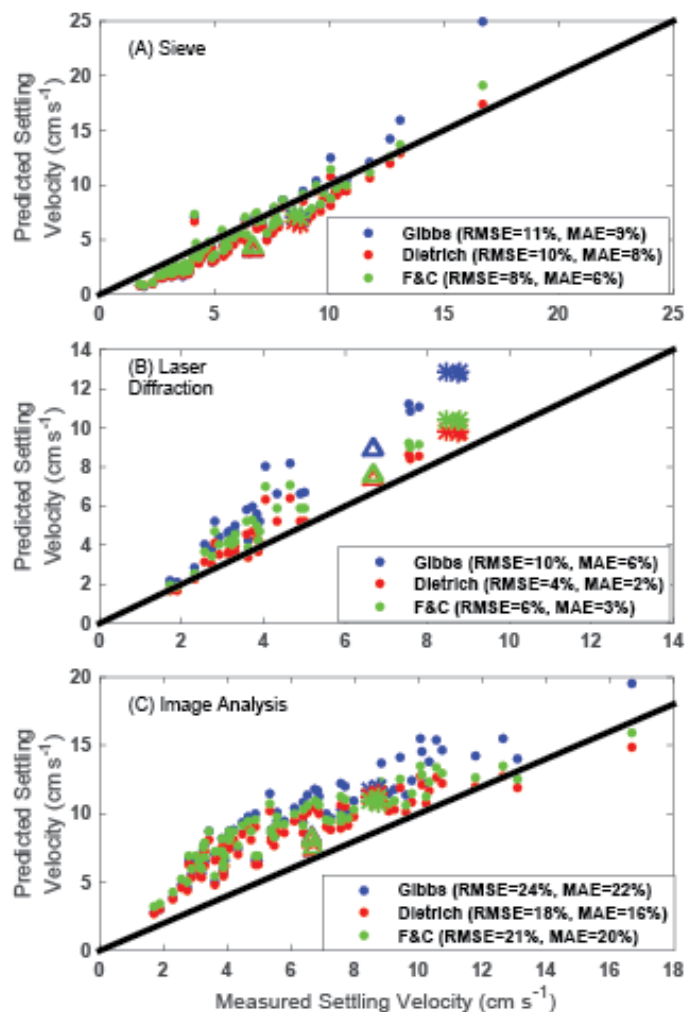


Figure 1.6. Comparison of equations used to convert (A) sieve, (B) laser diffraction, and (C) image analysis grain-sizes to settling velocity. In all panels, blue indicates the Gibbs et al., (1971) equation, red indicates Dietrich (1982), and green indicates Ferguson and Church (2004); asterisks indicate aragonite sand standard, triangles indicate quartz sand standard.

1.4 Discussion

The size and shape of the ROI used in the image analyses (Figure 1.3) affected the calculated GSD. In general, larger ROIs led to the over-estimation of grain size. This response is consistent with Buscombe and Rubin (2012), who showed that image intensity in an image of sediment is a non-stationary random field; therefore, by changing the size and location of the window (i.e. ROI), the 2nd-order (spatial) statistics of image intensity change. Sayles and Thomas (1978) showed that, in such a situation, the variance in the power spectral density is directly proportional to the bandwidth (in the frequency domain) which is related to the window size (in the spatial domain). In this case, the effect was to coarse-bias the estimates of grain-size for large ROIs. Given that the effects of ROI size on grain size estimates are likely to be different for each sedimentary population, being related to numerous factors such as the ratio of grain size to window size, grain sorting, orientation, and shape, in practice, the size and number of ROIs should ideally be treated as tunable parameters to be determined empirically, such as here, in the practical implementation of the method of Buscombe (2013). It is suggested that averaging results from large numbers of relatively small ROIs should work best in most cases; however, caution should be used when applying image analysis to intermediate settling velocity material as this material yielded the highest errors (

Figure 1.6C).

Varying sediment density across the range of reported values (1.15 – 2.8 g cm⁻³; Table 1.1) caused an 11% to 28% range in RMSE depending upon settling velocity model and grain size method (Table 1.3). This highlights not only the importance of using an accurate sediment density in settling velocity calculations but also the need to understand why there exists such a range in reported values. This range is a function of how different investigators define the density of their sediments, the nature of their study, the distinct ways carbonate

producers calcify, and the inherent diversity of sediment constituents within the sediment pool. Studies aimed at the movement of specific facies (e.g., foraminifera) often report an ‘effective’ density for irregularly shaped particles that implicitly assumes a particle of an equivalent spherical diameter whose density matches the observed settling velocity (Berthois and Calvez, 1960; Berger and Piper, 1972; Fok-pun and Komar, 1983). Studies aimed at constructing reef- or system-scale budgets of carbonate chemistry, however, often report a ‘bulk’ sediment density (ρ_{bulk}), which includes the microporosity of the particles (ϕ_{part}) and the mineral density ($\rho_{mineral}$; e.g., $\rho_{bulk} = \rho_{mineral} * (1 - \phi_{part})$) so that changes in the mass of calcium carbonate can be computed from changes in sediment volume (Stearn et al., 1977; Land, 1979; Grigg, 1982; Sadd, 1984; Hubbard et al., 1990). Previous examinations of the porosity of specific sediment constituents have shown that corals and coralline algae are ~50-60% porous (Stearn et al., 1977; Grigg, 1982); therefore, $\rho_{bulk} \sim 1.5 \text{ g cm}^{-3}$ seems to be a reasonable value for budget calculations (see Appendix in Sadd, 1984 for example calculations).

Finally, studies aimed at understanding the physical suspension, transport, and deposition of sediments generally report the average density of the particles suspended in the fluid (i.e. ρ_{part}) which includes the water or seawater that occupies the micro-porosity of the sediment grains (e.g., $\rho_{part} = \rho_{mineral} * (1 - \phi_{part}) + \rho * \phi_{part}$) so as to best represent their hydraulic behaviour in a moving fluid (Kench and Mclean, 1997; Paphitis et al., 2002; Smith and Cheung, 2003). Both this study and the only other study, to the authors’ knowledge, that measured ρ_{part} with a similar method, reported a value of $\sim 2.6 \text{ g cm}^{-3}$ (Smith and Cheung, 2003); however, other transport studies have used a value of 1.85 g cm^{-3} (Kench and Mclean, 1997; Morgan and Kench, 2014), which originates from component-specific measurements by Jell et al. (1965). This difference in ρ_{part} can be attributed to a variety of possible factors including: sediment composition, mean grain size, measurement technique, and depositional environment. Sediment composition is likely not the cause because all three studies had similar constituent assemblages. Although the sediment samples studied by Kench and McLean (1997) generally had a larger mean grain size, both our results and those of Smith and Cheung (2003) showed that ρ_{part} was independent of grain size. Unfortunately, Jell et al. (1965) do not explain how they determined specific gravity; therefore, it is difficult to evaluate their measurement technique against their derived values. Depositional environment could be an important factor, as this study and that of Smith and Cheung (2003), both analysed sediments from fringing reefs, whereas Kench and McLean (1997) analysed sediments from an atoll system. If we assume that 1.85 and 2.6 g cm^{-3} are representative values for atoll systems and fringing reefs, respectively, then one explanation for the difference in ρ_{part} could be the age of sediments in the respective systems. For example, sands in Hawaiian fringing reef systems have been shown to be derived from older (100s-1000s years old) material (Harney et al., 2000) and material from the top 1 m of a lagoon core at Tantabiddi has been dated to ~ 5000 years old (Collins et al., 2003). However, work in reef island systems have shown that sediment is derived from modern (10s years old) sources (e.g., modern reef calcifiers; Yamano et al., 2000; Dawson et al., 2012). It is therefore possible that due to their age, fringing reef sediments no longer retain their original internal porosities (e.g., taphonomic processes and/or internal microboring could alter internal structures), and therefore have a higher ρ_{part} ; reef island sands, on the other hand, likely still retain the microstructure of the biogenic source material and therefore could have a lower ρ_{part} . However, as there have been so few actual measurements of ρ_{part} in various bioclastic environments, there is a clear need for more work like the present contribution to resolve the above discussion and to understand the range of sediment densities applicable to these different systems.

Shape is also a key factor when determining settling velocities, as any divergence from spherical can only lead to decreases in settling velocity when compared to spherical particles of an equivalent weight (Dietrich, 1982). Although the D&F and Church models explicitly account for particle shape, the Gibbs equation does not. Shape effects are visible in the Gibbs data for sieve and laser diffraction as increasing over-estimation of settling velocity with increasing measured settling velocity (Figure 1.6A,B). Similar results have been shown in previous comparisons between sieve and laser diffraction measurements (Konert and Vandenberghe, 1997; Blott and Pye, 2006), as well as between sieve and settling tube measurements (Komar and Cui, 1984; Kench and Mclean, 1997). Shape effects on settling velocity are primarily due to the fact that natural particles settle perpendicular to their largest projected area, which increases drag on the particle and leads to a slower settling velocity (Dietrich, 1982; Komar and Cui, 1984). This has been shown to reduce settling velocities by a maximum of $\sim 2x$ for particles coarser than $\sim 1.4 \text{ mm}$, or by $\sim 1.5x$

for those smaller than ~ 1.4 mm (Dietrich, 1982).

In bioclastic environments, shape is inherently linked to the specific organism the particle is derived from (Perry et al., 2011); therefore, constituent assemblage could explain some of the increasing discrepancy between measured and estimated settling velocities for faster settling samples. Past studies of carbonate sediment settling have shown that typical constituents have specific settling behaviours that enhance the disagreement between sieve and settling tube results (Maiklem, 1968; Braithwaite, 1973; Smith and Cheung, 2003). Mollusc shells, for example, have large physical sizes but tend to settle with a spiral motion; this settling style will lead to slow settling velocities, whereas their shape will cause them to be trapped on coarser sieves (Maiklem, 1968; Braithwaite, 1973; Smith and Cheung, 2003). Indeed, the thin section analysis showed an increasing percentage of mollusc fragments (both broken and intact) in faster settling deposits collected from Ningaloo which, based on their settling behaviour and irregular shape, could help explain the over-estimation of calculated w_s by Gibbs for these samples.

When shape was accounted for by the settling velocity model (i.e. Dietrich or F&C), RMSE was improved by 3% to 6% (Table 1.3) and the velocity-dependent bias was removed from sieve and laser diffraction results (

Figure 1.6A,B). Furthermore, although F&C performs better for sieve diameters, Dietrich is more accurate for laser diffraction and image analysis and is also a more thorough treatment of particle irregularities. Therefore, Dietrich is suggested here as the preferred equation for settling velocity calculations.

In practical applications to bioclastic environments, settling velocities can be used to delineate various sub-environment zones (i.e. different reef zones) and to predict sediment transport mode; both of these applications are critical to understanding and predicting sediment transport pathways through these systems. Kench (1997) suggested that bioclastic sediment can be grouped into distinct settling velocity fractions, ranging from very slow settling (0.39 cm s^{-1} to 0.78 cm s^{-1}) to very fast settling (25 cm s^{-1} to 50 cm s^{-1}). Using this classification and measured settling velocities, there are clearly three settling velocities zones at Tantabiddi (Figure 1.7A): 1) fast-moderate settling on the fore reef/reef crest (6.25 cm s^{-1} to 12.5 cm s^{-1}); 2) Moderate settling on the reef flat and majority of the lagoon (3.12 cm s^{-1} to 6.25 cm s^{-1}); and 3) moderate-slow settling in the nearshore area of the southern channel (1.56 cm s^{-1} to 3.12 cm s^{-1}).

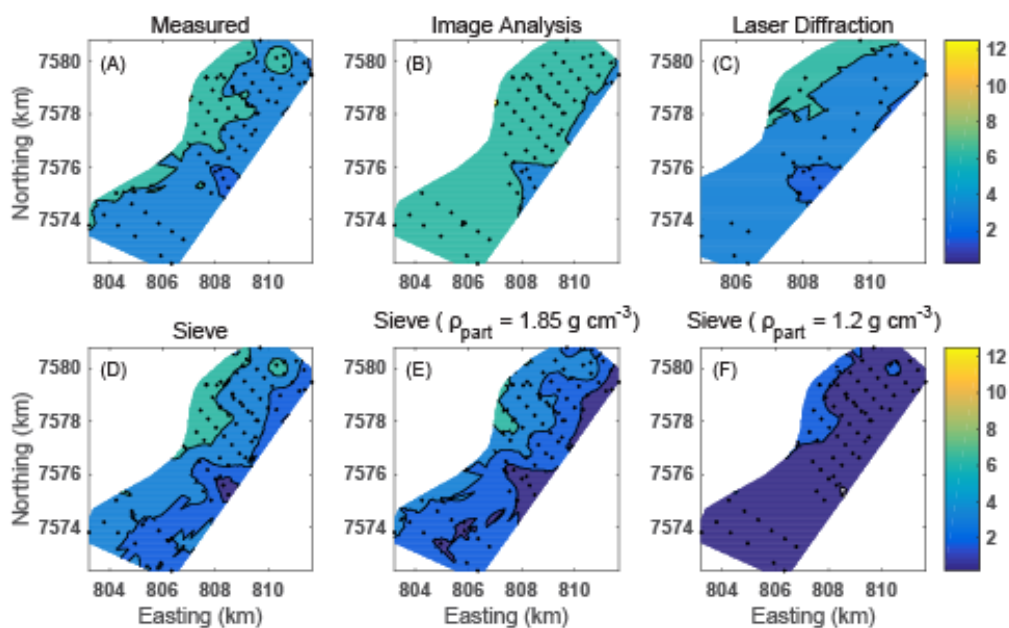


Figure 1.7. Spatial maps depicting settling velocity boundaries at Tantabiddi, Ningaloo Reef for (A) measured settling velocities, (B) image analysis-derived settling velocities, (C) laser diffraction-derived settling velocities, and (D) sieve-derived settling velocities. For B, C, and D, the Dietrich equation was used with $PRI = 3.5$, $CSF = 0.55$ or 0.7 , and ρ_{part} = measured values. E and F depict the settling velocity boundaries for sieve-derived measurements when $\rho_{part} = 1.85$ or 1.2 g cm^{-3} , respectively.

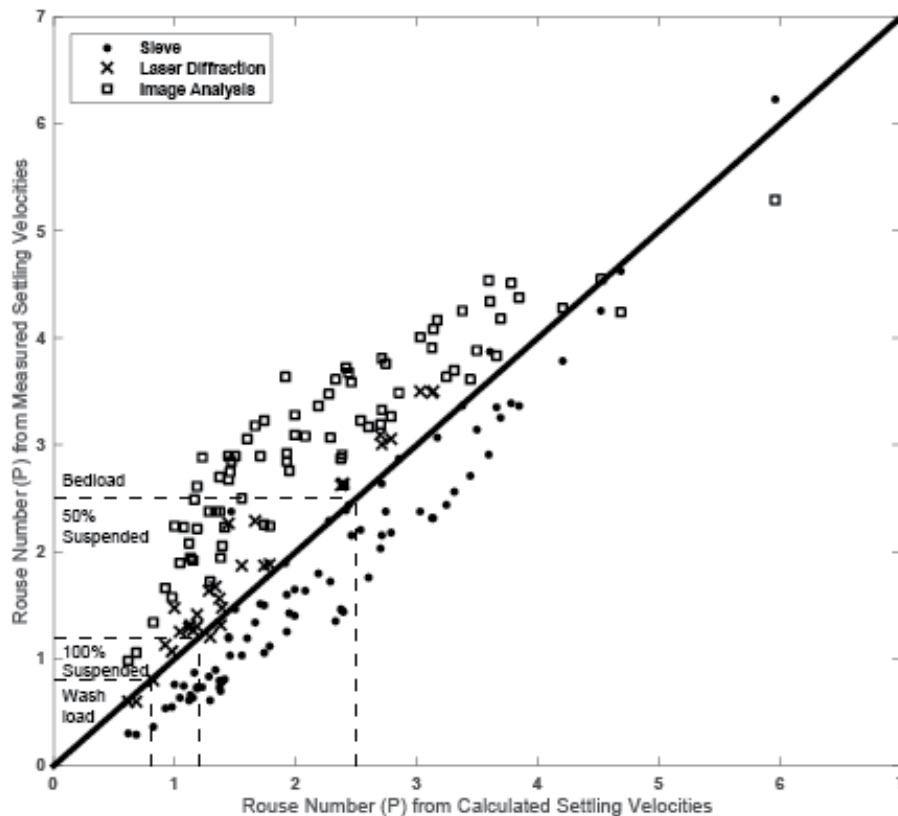


Figure 1.8. Comparison of Rouse number (P) from measured and calculated settling velocities. Values are shown for results from sieve, laser diffraction and image analysis.

Although no method is able to perfectly match the measured spatial variation, laser diffraction reproduces the correct number and location zones (Figure 1.7C); sieve reproduces the correct spatial pattern, however, it under-predicts the slowest settling material (Figure 1.7D); and, finally, when image analysis is used, there is no indication of the slowest settling zone and the fastest settling zone occupies a much larger area than measured. Furthermore, similar results are observed when ρ_{part} is varied for sieve results (i.e. variable number of zones and under-prediction of settling velocity) (Figure 1.7E,F).

Settling velocity can also be used to determine entrainment and transport mode (bedload, suspended load, or wash load) in aquatic environments, most commonly in the context of the Rouse number, $P = w_s/ku^*$, where k is the von Karman constant (0.4) and u^* is the shear velocity (Rouse, 1937). Sand ripples have been observed in the Ningaloo lagoon (~ 20 cm amplitude and ~ 50 cm wavelength) and wave-induced ripple migration (i.e., bedload transport) has been suggested to be primary mode of sediment supply to the shoreline (Cuttler et al., 2015).

Using Dietrich-derived settling velocities and a typical wave-induced u^* value of 7 cm s^{-1} (Cuttler et al., 2015) to calculate P for the lagoon samples, the use of laser diffraction and image analysis over-estimate P (i.e., trend towards predicting bedload transport), whereas the use of sieve slightly under-estimates P (Figure 1.8); however, the use of each grain size method would suggest that the majority of lagoon deposits are mobilised as bedload or partial suspended-load under normal wave conditions (significant wave height $\sim 1\text{-}2$ m), thus supporting the hypothesis that ripple migration is crucial to shoreline maintenance at Ningaloo.

1.5 Conclusions

Settling velocity is a common characteristic of sedimentary deposits that can be used to understand sediment

dynamics in aquatic environments. Although errors in predicted settling can be up to 20%, these errors are still small relative to the natural range of settling velocities of sand-sized material (0.05 to 0.30 cm s⁻¹, or a variation of ~83%; Smith and Cheung, 2003; Ferguson and Church, 2004). While these errors tended to be relatively uniform across the range of particle sizes for the sieve and image analysis, for the laser diffraction analysis the errors reduced at the smaller size fractions; this suggests that the laser diffraction approach can produce robust measurements of carbonate samples at fine sediment fractions (likely extending into the silt and clay fractions that are within the capabilities of the instrumentation). Although image analysis had the highest errors, we still encourage the use (with caution) and development of this technique as the greater spatial and temporal sampling it provides will greatly outweigh a slight increase in error.

Collectively, the results suggest that any of these common grain size analysis techniques and settling velocity models, which were originally developed for siliciclastic sediments, can be used to predict settling velocities of irregularly-shaped bioclastic sediments with reasonable accuracy; however, this agreement is improved when models account for shape effects. These results highlight the importance of using an accurate measure of sediment density when calculating settling velocity as an incorrect density can cause a change in RMSE of up to 28%. We suggest the use of the Dietrich (1982) model for estimating settling velocity because it is more accurate for more modern, time-saving techniques, and in general, is a more thorough treatment of particle irregularities. Finally, this analysis will allow for the conversion of grain size data from a variety of bioclastic environments to be converted to settling velocities for comparison; this will greatly enhance our understanding of sediment dynamics and transport processes in these environments.

1.6 Appendix

Dietrich (1982) accounts for particle density, shape and roundness when converting particle size to settling velocity through three fitted equations (see Eq. (0.6)) based on the non-dimensional settling velocity (W_*) and the non-dimensional grain size (D_*):

$$W_* = \frac{\rho w_s^3}{(\rho_s - \rho) g \nu} \quad (A1.1)$$

$$D_* = \frac{(\rho_s - \rho) g D_n^3}{\rho \nu^2} \quad (A1.2)$$

where ρ is fluid density, ρ_s is sediment density, ν is kinematic viscosity, w_s is settling velocity and D_n is nominal diameter.

The three fitted equations in Eq. (0.6) account for particle size and density (R_1), shape (R_2), and roundness (R_3). Particle size and density are related by a fourth-order polynomial:

$$R_1 = -3.76715 + 1.92944 \log D_* - 0.09815 \log D_*^2 \dots \\ \dots - 0.00575 \log D_*^3 + 0.00056 \log D_*^4 \quad (A1.3)$$

Particle shape is accounted for via the Corey (1949) shape factor (CSF), which ranges from 0 to 1:

$$R_2 = \left(\log \left(1 - \frac{1 - CSF}{0.85} \right) \right) - (1 - CSF)^{2.3} \tanh(\log D_* - 4.6) \dots \\ \dots + 0.3(0.5 - CSF)(1 - CSF)^2 (\log D_* - 4.6) \quad (A1.4)$$

Finally, the effect of particle roundness is incorporated using the Powers (1953) roundness index (PRI):

$$R_3 = \left[0.65 - \left(\frac{CSF}{2.83} \tanh(\log D_* - 4.6) \right) \right]^{1 + (3.5 - PRI)/2.5} \quad (A1.5)$$

These three equations are then combined to give w_s (Eq. (0.6)).

1.7 References

- ASTM International (2010) Standard Test Methods for Specific Gravity of Soil Solids by Water Pycnometer, ASTM International. West Conshohocken, Pennsylvania, USA. doi:10.1520/D0854-10.2
- Barnard, P.L., Rubin, D.M., Harney, J., and Mustain, N. (2007) Field test comparison of an autocorrelation technique for determining grain size using a digital “beachball” camera versus traditional methods. *Sed. Geol.*, 201, 180–195. doi:10.1016/j.sedgeo.2007.05.016
- Berger, H. and Piper, D.J.W. (1972) Planktonic foraminifera: differential settling, dissolution and redeposition. *Limnol. Oceanogr.*, 17, 275–287.
- Berthois, L. and Calvez, L.E. (1960) Etude de la vitesse de chute des coquilles de foraminifères planctoniques dans un fluide comparativement a celle des grains de quartz. *Revue des Travaux de l'Institut des Pêches Maritimes*, 24, 293-301.
- Birch, G. and Taylor, S. (1999) Source of heavy metals in sediments of the Port Jackson estuary, Australia. *Sci. Total Environ.*, 227, 123 – 138.
- Blott, S.J. and Pye, K. (2001) GRADISTAT: a grain size distribution and statistics package for the analysis of unconsolidated sediments. *Earth Surf. Proc. Land.*, 26, 1237–1248. doi:10.1002/esp.261
- Blott, S.J. and Pye, K. (2006) Particle size distribution analysis of sand-sized particles by laser diffraction: An experimental investigation of instrument sensitivity and the effects of particle shape. *Sedimentology*, 53, 671–685. doi:10.1111/j.1365-3091.2006.00786.x
- Braithwaite, C. (1973) Settling behaviour related to sieve analysis of skeletal sands. *Sedimentology*, 20, 251–262. doi:10.1111/j.1365-3091.1973.tb02048.x
- Buscombe, D. (2008) Estimation of grain-size distributions and associated parameters from digital images of sediment. *Sed. Geol.*, 210, 1–10. doi:10.1016/j.sedgeo.2008.06.007
- Buscombe, D. (2013) Transferable wavelet method for grain-size distribution from images of sediment surfaces and thin sections, and other natural granular patterns. *Sedimentology*, 60, 1709–1732. doi:10.1111/sed.12049
- Buscombe, D. and Masselink, G. (2009) Grain-size information from the statistical properties of digital images of sediment. *Sedimentology*, 56, 421–438. doi:10.1111/j.1365-3091.2008.00977.x
- Buscombe, D. and Rubin, D.M. (2012) Advances in the simulation and automated measurement of well-sorted granular material: 1. Simulation. *J. Geophys. Res.*, 117, F02001. doi:10.1029/2011JF001974
- Buscombe, D., Rubin, D.M., and Warrick, J.A. (2010) A universal approximation of grain size from images of noncohesive sediment. *J. Geophys. Res.*, 115, 1–17. doi:10.1029/2009JF001477
- Buscombe, D., Rubin, D.M., Lacy, J.R., Storlazzi, C.D., Hatcher, G., Chezard, H., Wyland, R., and Sherwood, C.R. (2014) Autonomous bed-sediment imaging-systems for revealing temporal variability of grain size. *Limnol. Oceanogr.: Methods*, 12, 390–406. doi:10.4319/lom.2014.12.390
- Chang, F.-J. and Chung, C.-H. (2012) Estimation of riverbed grain-size distribution using image-processing techniques. *J. Hydrol.*, 440-441, 102–112. doi:10.1016/j.jhydrol.2012.03.032
- Cheetham, M.D., Keene, A.F., Bush, R.T., Sullivan, L.A., and Erskine, W.D. (2008) A comparison of grain-size analysis methods for sand-dominated fluvial sediments. *Sedimentology*, 55, 1905–1913. doi:10.1111/j.1365-3091.2008.00972.x
- Cheng, N.S. (1997) Simplified settling velocity formula for sediment particle. *J. Hydraul. Eng.*, 123, 149–152.
- Cheng, Z. and Liu, H. (2015) Digital grain-size analysis based on autocorrelation algorithm. *Sed. Geol.*, 327, 21–31. doi:10.1016/j.sedgeo.2015.07.008
- Collins, L.B., Zhu, Z.R., Wyrwoll, K.H., and Eisenhauer, A. (2003) Late Quaternary structure and development of the northern Ningaloo Reef, Australia. *Sedimentary Geology*, 159, 81-94.
- Corey, A.T. (1949) Influence of shape on the fall velocity of sand grains. Colorado A & M College, Fort Collins, unpub. Master’s thesis, 102 p.
- Cuttler, M., Lowe, R.J., Hansen, J.E., Falter, J.L., and Pomeroy, A.W.M. (2015) Grainsize, composition and bedform patterns in a fringing reef system. *Proc. Coastal Sed.*, San Diego, California, USA.
- Dawson, J.L., Hua, Q., and Smithers, S.G. (2012) Benthic foraminifera : Their importance to future reef island resilience. *Proc. 12th Int. Coral Reef Symp.*, Cairns, Australia.
- Di Maria, F., Bianconi, F., Micale, C., Baglioni, S., and Marionni, M. (2016) Quality assessment for recycling aggregates from construction and demolition waste: An image-based approach for particle size estimation. *Waste Management*, 48, 344 – 352.
- Di Stefano, C., Ferro, V., and Mirabile, S. (2010) Comparison between grain-size analyses using laser diffraction and sedimentation methods. *Biosystems Engineering*, 106, 205–215. doi:10.1016/j.biosystemseng.2010.03.013

- Dietrich, W.E. (1982) Settling velocity of natural particles. *Water Resour. Res.*, 18, 1615–1626. doi:10.1029/WR018i006p01615
- Diplas, P. and Sutherland, A.J. (1988) Sampling techniques for gravel sized sediments. *J. Hydraul. Eng.*, 114, 484–501.
- Diplas, P. and Fripp, J. B. (1992) Properties of various sediment sampling procedures. *J. Hydraul. Eng.*, 118, 955–970.
- Diplas, P., Kuhnle, R., Gray, J., Glysson, D. and Edwards, T. (2008) Sediment transport measurements. *Sedimentation Engineering: Theories, Measurements, Modeling, and Practice. ASCE Manuals and Reports on Engineering Practice*, 110, 165-252.
- Dyer, K.R. (1997) *Estuaries: A Physical Introduction*, 2nd ed. John Wiley & Sons Ltd, Chichester.
- Ferguson, R.I. and Church, M. (2004) A simple universal equation for grain settling velocity. *J. Sed. Res.*, 74, 933–937. doi:10.1306/051204740933
- Fok-pun, L. and Komar, P.D. (1983) Settling velocities of planktonic foraminifera : density variations and shape effects. *J. Foramin. Res.*, 13, 60–68.
- Folk, R.L. and Ward, W.C. (1957) Brazos River Bar : A study in the significance of grain size parameters. *J. Sed. Petrol.*, 27, 3–26.
- Gallagher, E.L., MacMahan, J., Reniers, A.J.H.M., Brown, J., and Thornton, E.B. (2011) Grain size variability on a rip-channeled beach. *Mar. Geol.*, 287, 43–53. doi:10.1016/j.margeo.2011.06.010
- Gibbs, R.J., Matthews, M.D., and Link, D.A. (1971) The relationship between sphere size and settling velocity. *J. Sed. Res.*, 41, 7–18. doi:10.1306/74d721d0-2b21-11d7-8648000102c1865d
- Graham, D.J., Rice, S.P., and Reid, I. (2005) A transferable method for the automated grain sizing of river gravels. *Water Resour. Res.*, 41, W07020. doi:10.1029/2004WR003868
- Graham, D.J., Rollet, A.J., Piégay, H., and Rice, S.P. (2010) Maximizing the accuracy of image-based surface sediment sampling techniques. *Water Resour. Res.*, 46, 1–15. doi:10.1029/2008WR006940
- Graham, D., Rollet, A.J., Rice, S.P. and Piégay, H. (2012) Conversions of Surface Grain-Size Samples Collected and Recorded Using Different Procedures. *J. Hydraul. Eng.*, 138, 839–849. doi:10.1061/(ASCE)HY.1943-7900.0000595
- Grigg, R.W. (1982) Darwin Point: A threshold for atoll formation. *Coral Reefs*, 1, 29–34. doi:10.1007/BF00286537
- Harney, J.N. and Fletcher, C.H. (2003) A budget of carbonate framework and sediment production, Kailua Bay, Oahu, Hawaii. *J. Sed. Res.*, 73, 856–868. doi:10.1306/051503730856
- Harney, J.N., Grossman, E.E., Richmond, B.M., and Fletcher III, C.H. (2000) Age and composition of carbonate shoreface sediments, Kailua Bay, Oahu, Hawaii. *Coral Reefs*, 19, 141–154.
- Hubbard, D.K., Miller, A.I., and Scaturro, D. (1990) Production and cycling of calcium carbonate in a shelf-edge reef system (St. Croix, U.S. Virgin Islands): Applications to the nature of reef systems in the fossil record. *J. Sed. Petrol.*, doi:10.1306/212F9197-2B24-11D7-8648000102C1865D
- Jell, J.S., Maxwell, W.H.G., and McKellar, R.G. (1965) The significance of the larger foraminifera in the Heron Island Reef Sediments. *J. Paleontol.*, 39, 273–279.
- Kellerhals, P. and Bray, D.I. (1971) Sampling procedures for coarse fluvial sediments. *J. Hydraul. Eng.*, 97, 1165–1180.
- Kench, P.S. (1997) Contemporary sedimentation in the Cocos (Keeling) Islands, Indian Ocean: interpretation using settling velocity analysis. *Sed. Geol.*, 114, 109–130.
- Kench, P.S. and Mclean, R.F. (1997) A comparison of settling and sieve techniques for the analysis of bioclastic sediments. *Sed. Geol.*, 109, 111–119.
- King, G.E., Herman, F., Lambert, R., Valla, P.G., and Guralnik, B. (2016) Multi-OSL-thermochronometry of feldspar. *Quaternary Geochronology*, doi:10.1016/j.quageo.2016.01.004
- Komar, P.D. (1981) The applicability of the Gibbs equation for grain settling velocities to conditions other than quartz grains in water. *J. Sed. Petrol.*, 51, 1125–1132.
- Komar, P.D. and Cui, B. (1984) The Analysis of Grain-Size Measurements by Sieving and Settling-Tube Techniques. *J. Sed. Petrol.*, 54, 603–614.
- Komar, P. and Clemens, K. (1986) The relationship between a grain's settling velocity and threshold of motion under unidirectional currents. *J. Sed. Res.*, 56, 258–266. doi:10.1306/212F88DC-2B24-11D7-8648000102C1865D
- Konert, M. and Vandenberghe, J. (1997) Comparison of laser grain size analysis with pipette and sieve analysis: a solution for the underestimation of the clay fraction. *Sedimentology*, 44, 523–535. doi:10.1046/j.1365-3091.1997.d01-38.x
- Land, L.S. (1979) The fate of reef-derived sediment on the north Jamaican island slope. *Mar. Geol.*, 29, 55–71.
- Le Roux, J.P. (1992) Settling velocity of spheres: a new approach. *Sed. Geol.*, 81, 11–16.

- Le Roux, J.P. (2002) Shape entropy and settling velocity of natural grains. *J. Sed. Res.*, 72, 363–366.
- Maiklem, W.R. (1968) Some hydraulic properties of bioclastic carbonate grains. *Sedimentology*, 10, 101–109.
- McCave, I.N. and Syvitski, J.P.M. (1991) Principles and methods of geological particle size analysis, in: Syvitski, J.P.M. (Ed.), Principles, Methods, and Application of Particle Size Analysis. Cambridge University Press, New York, p. 368.
- Michels, K.H. (2000) Inferring maximum geostrophic current velocities in the Norwegian-Greenland Sea from settling-velocity measurements of sediment surface samples: methods, applications and results. *J. Sed. Res.*, 70, 1036-1050.
- Miller, M.C., McCave, I.N., and Komar, P.D. (1977) Threshold of sediment motion under unidirectional currents. *Sedimentology*, 24, 507–527. doi:10.1111/j.1365-3091.1977.tb00136.x
- Morgan, K.M. and Kench, P.S. (2014) A detrital sediment budget of a Maldivian reef platform. *Geomorphology*, 222, 122–131. doi:10.1016/j.geomorph.2014.02.013
- Neumann, A.C. and Land, L.S. (1975) Lime mud deposition and calcareous algae in the Bight of Abaco, Bahamas: A budget. *J. Sed. Petrol.*, 45, 763-786.
- Paphitis, D., Collins, M.B., Nash, L. A., and Wallbridge, S. (2002) Settling velocities and entrainment thresholds of biogenic sands (shell fragments) under unidirectional flow. *Sedimentology*, 49, 211–225. doi:10.1046/j.1365-3091.2002.00446.x
- Powers, M.C. (1953) A new roundness scale for sedimentary particles. *J. Sed. Res.*, 23, 117 – 119.
- Rittenhouse, G. (1943) Relation of shape to the passage of grains through sieves. *Ind. Eng. Chem. Fundam.*, 15, 153–155.
- Rogers, C.S. (1990) Responses of coral reefs and reef organisms to sedimentation. *Mar. Ecol. Prog. Ser.*, 62, 185–202. doi:10.3354/meps062185
- Román-Sierra, J., Muñoz-perez, J.J., and Navarro-Pons, M. (2013) Influence of sieving time on the efficiency and accuracy of grain-size analysis of beach and dune sands. *Sedimentology*, 60, 1484–1497. doi:10.1111/sed.12040
- Rouse, H. (1937) Modern conceptions of the mechanics or fluid turbulence. *Trans. Am. Soc. Civ. Eng.* 102, 463–505.
- Rubin, D.M. (2004) A Simple Autocorrelation Algorithm for Determining Grain Size from Digital Images of Sediment. *J. Sed. Res.*, 74, 160–165. doi:10.1306/052203740160
- Sadd, J.L. (1984) Sediment transport and CaCO₃ budget on a fringing reef, Cane Bay, St. Croix, U.S. Virgin Islands. *Bull. Mar. Sci.*, 35, 221-238.
- Savitzky, A. and Golay, M.J.E. (1964) Smoothing and Differentiation of Data by Simplified Least Squares Procedures. *Anal. Chem.*, 36, 1627–1639. doi:10.1021/ac60214a047
- Sayles, R.S. and Thomas, T.R. (1978) Surface topography as a non-stationary random process. *Nature*, 271, 431-434.
- Sime, L.C. and Ferguson, R.I. (2003) Information on grain sizes in gravel-bed rivers by automated image analysis. *Res. Methods Pap.*, 73, 630–636. doi:10.1306/112102730630
- Smith, D.A. and Cheung, K.F. (2002) Empirical Relationships for Grain Size Parameters of Calcareous Sand on Oahu, Hawaii. *J. Coastal Res.*, 18, 82–93.
- Smith, D.A. and Cheung, K.F. (2003) Settling Characteristics of Calcareous Sand. *J. Hydraul. Eng.*, 129, 479–483. doi:10.1061/(ASCE)0733-9429(2003)129:6(479)
- Stearn, C.W., Scoffin, T.P., and Martindale, W. (1977) Calcium Carbonate Budget of a Fringing Reef on the West Coast of Barbados. *Bull. Mar. Sci.*, 27, 479–510.
- Storlazzi, C.D., Norris, B., Rosenberger, K.J. (2015) The influence of grain size, grain color, and suspended-sediment concentration on light attenuation: Why fine-grained terrestrial sediment is bad for coral reef ecosystems. *Coral Reefs*, 34, 967-975.
- Syvitski, J.P.M., Smith, J.N., Calabrese, E.A., and Boudreau, B.P. (1988) Basin sedimentation and the growth of prograding deltas. *J. Geophys. Res.*, 93, 6895 – 6908.
- Warrick, J.A., Rubin, D.M., Ruggiero, P., Harney, J.N., Draut, A.E., and Buscombe, D. (2009) Cobble cam: grain-size measurements of sand to boulder from digital photographs and autocorrelation analyses. *Earth Surf. Proc. Land.*, 34, 1811 – 1821.
- Yamano, H., Miyajima, T., and Koike, I. (2000) Importance of foraminifera for the formation and maintenance of a coral sand cay: Green Island, Australia. *Coral Reefs*, 19, 51–58. doi:10.1007/s003380050226

2 Sediment transport in the presence of large reef bottom roughness²

Abstract

The presence of large bottom roughness, such as that formed by benthic organisms on coral reef flats, has important implications for the size, concentration, and transport of suspended sediment in coastal environments. A three-week field study was conducted in approximately 1.5 m water depth on the reef flat at Ningaloo Reef, Western Australia, to quantify the cross-reef hydrodynamics and suspended sediment dynamics over the large bottom roughness (~20–40 cm) at the site. A logarithmic mean current profile consistently developed above the height of the roughness; however, the flow was substantially reduced below the height of the roughness (canopy region). Shear velocities inferred from the logarithmic profile and Reynolds stresses measured at the top of the roughness, which are traditionally used in predictive sediment transport formulations, were similar but much larger than that required to suspend the relatively coarse sediment present at the bed. Importantly, these stresses did not represent the stresses imparted on the sediment measured in suspension and are therefore not relevant to the description of suspended sediment transport in systems with large bottom roughness. Estimates of the bed shear stresses that accounted for the reduced near-bed flow in the presence of large roughness vastly improved the relationship between the predicted and observed grain sizes that were in suspension. Thus the impact of roughness, not only on the overlying flow but also on bed stresses, must be accounted for to accurately estimate suspended sediment transport in regions with large bottom roughness, a common feature of many shallow coastal ecosystems.

2.1 Introduction

The presence of large bottom roughness over coral reefs directly modifies the nearbed hydrodynamics that are responsible for sediment transport. For typical wave-exposed reefs, cross-reef mean flows (currents) are generated by radiation stress gradients induced by incident short (sea-swell) waves breaking in the surf zone (i.e., waves with periods 5–25 s) and the associated mean water level gradients (wave setup) (e.g., Hench et al., 2008; Lowe et al., 2009b; Symonds et al., 1995). Smaller incident waves that do not break in the surf zone are transmitted across reef flats as depth-limited waves (e.g., Hardy and Young, 1996), with infragravity waves that emanate from the surf zone also propagating across the reef (e.g., Pomeroy et al., 2012). The large bottom roughness of reefs can impose substantial drag forces on the mean wave-driven currents, and also attenuate wave heights by frictional dissipation as they propagate shoreward across the reef (e.g., Lowe et al., 2005a; Pomeroy et al., 2012; Rosman and Hench, 2011). Thus, the hydrodynamic processes that prevail within reef systems are determined by the specific roughness characteristics of a reef, which in turn controls how sediment is transported in these environments.

Suspended sediment at high concentrations can adversely affect a variety of benthic reef organisms via multiple mechanisms. As sediment concentrations in the water column increase, light is attenuated and the spectrum is altered, reducing the efficiency of photosynthetic processes that many reef primary producers rely on for energy production (see Roth, 2014 for a review). In addition, when the rate of sedimentation is higher than the rate at which sediment is expelled, coral communities become smothered. This inhibits biotic particle feeding and nutrient uptake rates (e.g., Anthony, 2000) and can eventually lead to mortality (e.g., Weber et al., 2012).

For open (bare) sediment beds lacking large immobile bed roughness, the initiation of sediment transport is directly related to the shear stresses that are exerted on the sediment bed (τ_{bed}). Motion is initiated when these

² Published as Pomeroy, A., Lowe, R., Ghisalberti, M., Storlazzi, C., Symonds, G., Roelvink, D. (2017) *Journal of Geophysical Research: Oceans*, doi:10.1002/2016JC011755

bed stresses exceed a critical threshold that is dependent upon sediment properties, namely grain size and sediment density (i.e., as expressed in various forms of the classic Shields equation (Shields, 1936)). When the vertical velocity component of turbulent eddies are sufficiently large to overcome the particle fall velocity (w_s), sediment is lifted into suspension where it can be more efficiently transported (e.g., Bagnold, 1966; Francis, 1973; Van Rijn, 1984). Vertical turbulent velocity fluctuations associated with these eddies scale with the horizontal bed stresses, or alternatively the shear velocity ($u_* = \sqrt{\tau_{bed} / \rho_w}$) based on seawater density (ρ_w); therefore, relationships used to predict whether transport occurs usually depend on the magnitude of w_s relative to u_* . Within the water column, in a conventional steady-state 1D (vertical) model, the upward diffusion of sediment is balanced by downward settling. This diffusion is described by the vertical gradient in concentration and a sediment mixing coefficient (ε_s), which can be inferred from various turbulence closure models (e.g., Van Rijn, 1993). Irrespective of the closure model assumed, ε_s is dependent upon the turbulent shear stresses within the bottom boundary layer - the region where sediment particles are predominantly suspended and transported. Hence τ_{bed} (or u_*) is assumed to control many components of the overall sediment transport process, including (a) whether sediment will initially move, (b) whether that sediment will be suspended, and (c) the vertical distribution of suspended sediment concentration in the water column. Collectively, these components form the basis for modern suspended sediment transport models.

When sediment is interspersed within immobile bed roughness, such as on coral reefs as well as within aquatic vegetation such as a seagrass meadow, the mean and turbulent flow structure is substantially modified adjacent to the bed (i.e., within a 'roughness sublayer' or 'canopy', defined as the region where the flow is locally modified by individual roughness elements; (Raupach et al., 1991)). While the overlying flow may experience increased hydraulic resistance as a result of this roughness, the flow that actually interacts with the underlying bed can be substantially attenuated, which in turn reduces the bed shear stresses (e.g., Le Bouiteiller and Venditti, 2015). In aquatic canopies, this flow attenuation can promote sediment deposition, especially when canopy densities are high (e.g., Gacia et al., 1999; James et al., 2004). A limited number of laboratory studies have quantified how sediment transport is modified by large immobile roughness. Of these studies, most only consider bulk sediment transport quantities (e.g., total transport) and do not explicitly consider how modifications to flow by roughness will alter sediment transport mechanisms that make up these bulk transport rates (e.g., Baptist, 2005; Chen et al., 2012; James et al., 2002; James et al., 2004; Kothiyari et al., 2009). In field experiments, the primary focus of most studies has been on how suspended sediment concentrations (SSCs) and/or suspended sediment fluxes (SSFs) measured at specific point locations in the water column are empirically correlated to the local wave and/or current conditions (e.g., Ogston et al., 2004; Storlazzi et al., 2009; Storlazzi et al., 2004; Suhayda and Roberts, 1977). Although such correlations may exist, they do not provide fundamental insight into the quantitative links between the hydrodynamic processes, immobile bottom roughness, and rates of sediment transport. Thus, the dynamics of suspended sediment transport in the presence of large roughness elements, such as coral reefs, remains poorly quantified in natural coastal environments and motivates the present study.

We hypothesize that the drag forces exerted by large immobile roughness overlying a coral reef can significantly reduce shear stresses that are directly exerted on an underlying sediment bed, and as a consequence, traditional measures of bottom stresses on a reef are poor predictors of SSCs and SSFs. The objectives of this study were to: (1) assess the 'rough-wall' boundary layer flow dynamics and turbulent shear stresses over a coral reef flat; (2) quantify the grain-size distribution and concentrations of suspended sediment in the water column; and (3) evaluate how modifications to the mean and turbulent flow structure alter suspended sediment grain sizes, SSCs, and SSFs over a rough coral reef flat, including the implications for making robust sediment transport predictions within reef environments.

In Section 2, we review rough boundary layer theory and establish how near-bed flow and bed shear stresses are reduced within the roughness elements of a reef, and in turn how this may modify sediment transport. In Section 3, we then describe the field experiment conducted on a fringing reef, the instrument configurations, and the data analysis methodologies. The results are described in Section 4, and in Section 5 we discuss how large immobile roughness affects both SSCs and SSFs. In Section 6, we conclude with a discussion of implications

of this study for making robust prediction of suspended sediment transport on coral reefs and other analogous benthic ecosystems with large bottom roughness.

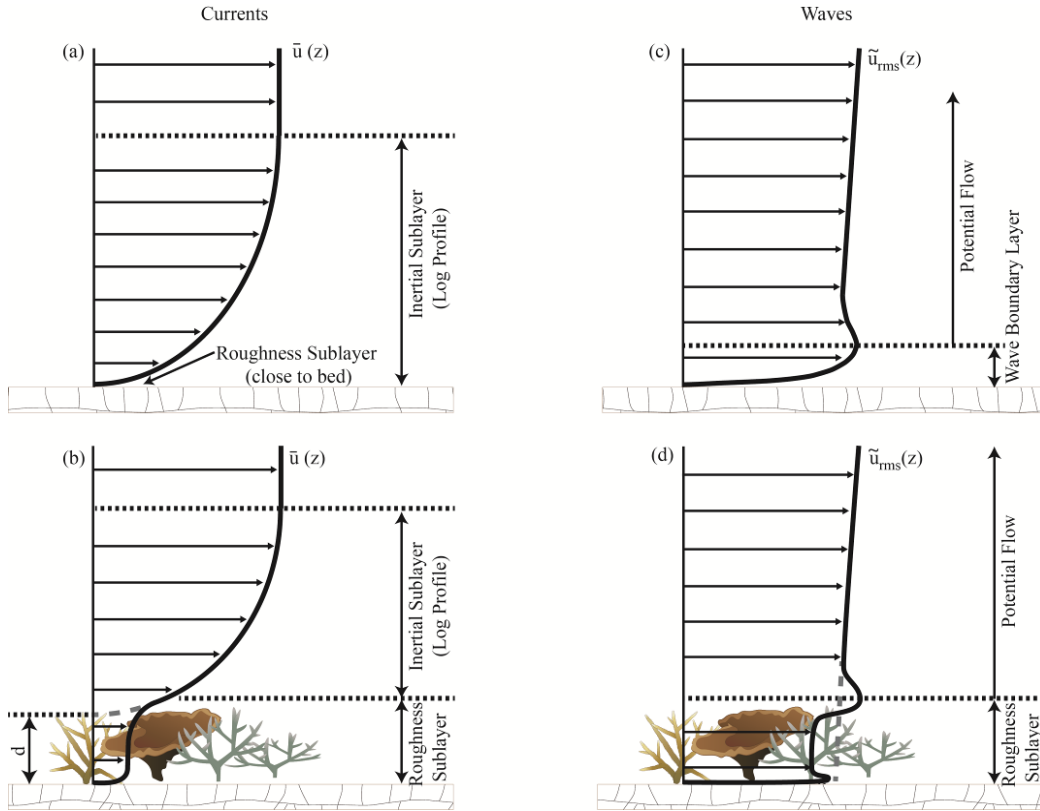


Figure 2.1. Conceptual model of the boundary layer flow structure for (top) bare beds and (bottom) beds with large roughness under (left) unidirectional (current) and (right) wave-dominated (oscillatory) flow conditions.

2.2 Background: flow structure and sediment transport within rough-wall boundary layers

Unidirectional flow

A rough-wall turbulent boundary layer associated with a unidirectional current can be partitioned into an inertial sublayer and roughness sublayer (Figure 2.1a). The inertial sublayer, often called the logarithmic layer, develops above the roughness sublayer where the individual roughness elements no longer directly affect the flow and the mean velocity (\bar{u}) profile tends to be governed by the ‘law of the wall’ (e.g., Raupach et al., 1991):

$$\bar{u} = \frac{u_{*c}}{\kappa} \log\left(\frac{z-d}{z_0}\right) \quad (1.1)$$

where z is height above the bed; κ is Von Karman’s constant; d is the vertical displacement of the mean velocity profile that relates to the penetration of momentum into the roughness; and z_0 is a hydraulic roughness parameter. In Eq. (2.1), the shear velocity u_{*c} is a measure of the turbulent shear stress at the top of the roughness and thus is equivalent to the resistance imposed by the roughness on the overlying current (note the subscript c will denote variables associated with currents).

The roughness sublayer is strongly influenced by the drag imposed by the roughness elements, which if modeled as simple geometric elements (e.g., cubes, cylinders) can be described as a function of the roughness height h , frontal area per unit volume a and a drag coefficient C_D (e.g., Nepf et al., 2007). When the bottom roughness is relatively small (i.e., $C_D ah$ is less than $O(10^{-2})$), such as over a flat sandy bed, the mean height of momentum absorption is located near the base of the roughness ($d \approx 0$) and $u_{*c} \approx u_{*c,bed}$, where $u_{*c,bed}$ is the bed shear velocity (Figure 2.1a). However, when the roughness is relatively large (i.e., $C_D ah$ exceeds $O(10^{-2})$), the drag

forces exerted by the roughness elements attenuate the spatially-averaged flow (see reviews by Finnigan, 2000; Nepf, 2012). This attenuation results in an inflection of the mean velocity profile at the top of the roughness where the maximum turbulent Reynolds shear stresses are also located. In this case, u_{*c} in Eq. (2.1) no longer describes the shear stress acting on the bed, but rather the local turbulent shear stress at the top of the roughness (i.e., $u_{*c} \approx u_{*c,rough}$, Figure 2.1b). Thus, within the roughness sublayer (or canopy), the reduction in flow can substantially reduce the shear stresses that are exerted on an underlying sediment bed ($\tau_{c,bed}$).

Wave-dominated flow

When surface waves propagate over a rough seafloor, a wave boundary layer (WBL) of thickness δ_w develops close to the bed (note the subscript w will denote variables associated with waves). Due to the oscillatory nature of the flow, wave-generated turbulence within the WBL can only experience limited vertical growth. A variety of forms for the eddy viscosity within the WBL have been proposed, but one of the simplest and most widely-used is that of Grant and Madsen (1979), where a representative (time-invariant) value is assumed. Based on this description, when the roughness is relatively small, δ_w is governed by the maximum shear velocity imposed by the wave flow (u_{*w}) and the wave angular frequency (ω); i.e. $\delta_w \sim \kappa u_{*w} / \omega$. The thin nature of the WBL generates larger bed shear stresses ($\tau_{w,bed}$) when compared to a unidirectional current of equivalent magnitude (Figure 2.1c).

Most research with waves has investigated how large roughness modifies the phase-dependent wave flow structure within the canopy region. Laboratory experiments with idealized canopies (e.g., Lowe et al., 2005b; Lowe et al., 2008; Luhar et al., 2010) and field experiments in seagrass canopies (e.g., Infantes et al., 2012) have demonstrated that the attenuation of the root-mean-squared (RMS) wave orbital velocities within the canopy is always less than that of a unidirectional flow of equivalent magnitude. This is due to the wave-driven oscillatory pressure gradient, which is opposed by both canopy drag and inertial forces (e.g., Lowe et al., 2005b; Zeller et al., 2015). Furthermore, wave phase-dependent Reynolds stresses are enhanced near the top of the roughness and then decrease towards zero within the canopy before they increase again near the bed (e.g., Lowe et al., 2008; Luhar et al., 2010). This stress profile suggests that for large roughness, two WBLs develop: a larger WBL near the top of the canopy (or roughness layer) and another, thinner, WBL near the bed (Figure 2.1d).

Wave-current boundary layers

The superposition of both waves and mean currents nonlinearly combine to modify the turbulent flow structure near the bed and enhance bed shear stresses. Over a wave cycle, the mean of these enhanced stresses (τ_m) is larger than pure current stresses (τ_c), and the maximum of the enhanced stresses (τ_{max}) is larger than the vector summation of τ_c and τ_w (e.g., Soulsby and Clarke, 2005).

A variety of wave-current interaction models have been proposed. Most of these models describe the turbulent flow structure over a bed with relatively small bed roughness, i.e., where the roughness height is small relative to the wave-current boundary layer thickness. These models are generally based on semi-empirical eddy viscosity profiles (see Wiberg, 1995 for a review). Under combined wave-current flow, a thin WBL of thickness δ_{max} exists that is controlled by u_{*max} . Above this WBL ($z > \delta_{max}$), the mean velocity profile maintains a logarithmic form described by Eq. (1); however, with u_{*c} instead replaced with the wave-enhanced mean velocity (u_{*m}) and z_0 replaced with an apparent roughness length (z_{0a}) that is also enhanced by the wave-induced turbulence near the bed relative to a pure unidirectional current (e.g., Grant and Madsen, 1979).

The dynamics of wave-current interactions that occur within large roughness (canopies) are still not well-established. However, it is reasonable to assume that the drag imposed by large roughness elements will cause greater attenuation of the current-component of the flow relative to the wave-component, which is supported by experimental observations (e.g., Lowe et al., 2005b; Lowe et al., 2008; Zeller et al., 2015). Thus, under wave-current conditions the flow within the roughness should be more strongly influenced by the contribution of the waves than the current. Similar arguments can be made to describe the flow structure near the top of the roughness and further up in the water column. At a sufficient height above a canopy, the flow structure should be analogous to a classic rough-wall wave-current boundary layer, with a logarithmic mean current profile

defined by u_{*m} and z_{0a} that are enhanced by wave-induced turbulence generated within the canopy.

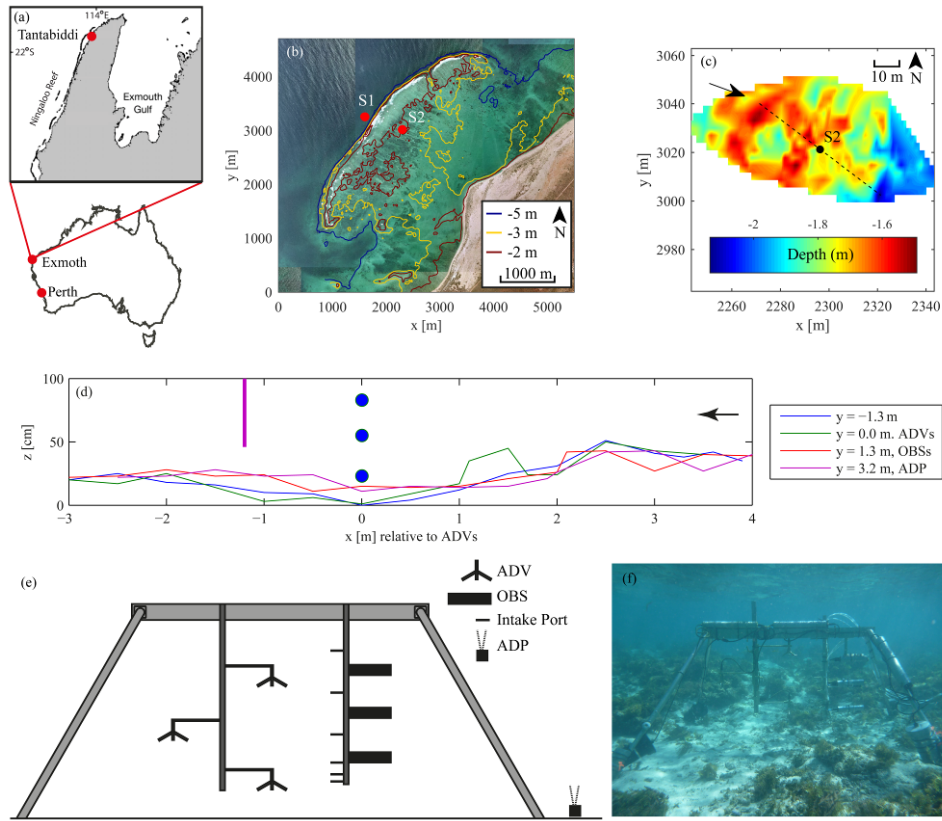


Figure 2.2. (a) The location of Tantabiddi within Ningaloo Reef in northern Western Australia. (b) An aerial view of the site (origin: 21.89248°S, 113.96203°E) with the location of the instruments relevant to this study and key contours indicated. (c) Interpolated sonar bathymetry around the high-resolution sampling site on the reef flat relative to the mean water level, with the mean flow direction indicated. The dashed line indicates the cross-reef direction. (d) Bathymetry transects measured perpendicular to the sawhorse frame from south to north and relative to the location of the vertical ADV array (blue dots). The vertical line indicates the vertical range of the ADP profiler within the vertical scale of the figure. The arrow denotes the mean flow direction during the experiment. (e) Schematic illustration of the sawhorse frame deployed in the experiment and (f) an underwater image of the site with the deployed instrumentation.

Sediment transport in the presence of large roughness

The total resistance experienced by the overlying flow (τ_{total}) is often partitioned into two components: (1) a bed stress component (τ_{bed}) that is due to the stress imposed by *sediment grains at the bed*; and (2) a *form drag component* (τ_{drag}) that is due to drag forces either by mobile bed forms (e.g., Van Rijn, 2007) or by immobile roughness (e.g., coral structures or aquatic vegetation (e.g., Le Bouteiller and Venditti, 2015).

$$\tau_{total} = \tau_{bed} + \tau_{drag} \quad (1.2)$$

In the presence of relatively small roughness (e.g., the sand grains themselves), τ_{drag} is small and $\tau_{total} \approx \tau_{bed}$; thus the shear stress exerted on overlying flow is equally relevant to the assessment of sediment transport. However, when the roughness is large, τ_{drag} can be substantially greater than τ_{bed} ; in this case the shear stress estimated from hydrodynamic measurements obtained higher in the water column, which includes the large form drag exerted by the roughness (i.e., τ_{total}), is not necessarily related to the stress exerted on the sediment. This has been demonstrated in idealized laboratory experiments where stresses inferred from law-of-the-wall fitting of the velocity profile above roughness have been shown to significantly overestimate bedload sediment transport (e.g., Le Bouteiller and Venditti, 2015), as well as the capacity of a unidirectional flow to suspend and transport sediment when compared to the same flow over a bare sediment bed (e.g., Bouma et al., 2007). Thus,

while the mobilization and suspension of sediment from the bed is broadly governed by the same physical processes (irrespective of whether the roughness is either large or small), these key differences between bed shear stresses should have important implications for rates of sediment transport, and notably the applicability of existing predictive formulae to environments with large roughness.

2.3 Methods

Site description

A 3-week field experiment (27 July–14 August 2013) was conducted in the northern region of Ningaloo Reef in Western Australia, focusing on a ~5 km section of reef near Tantabiddi (21°52'6"S, 113°58'58"E, Figure 2.2a). The study specifically focused on a section of reef bounded to the north and south by shore-normal channels (~6 m deep) that cut into the reef crest and outer reef flat. At this site, the cross-shore orientation of the reef is ~130° (defined as clockwise from true north), with the reef crest located 2.0–2.5 km from the shoreline. The reef flat is ~0.6–1.5 m below mean sea level and is ~500 m wide. The lagoon varies in width along the coast due to the presence of a shoreline salient, and is generally ~3 m deep. In contrast to many parts of southern Ningaloo Reef that typically have near 100% coral coverage, this site was specifically chosen as, like many reef systems worldwide, it contained a mix of macro-algae, coralline algae, sand, and some live coral (Cuttler et al., 2015).

Table 2.1. Instrument site information and sampling configuration[#]

Site and Depth		Instrument	Sampling Information
S1	(forereef ~10.5 m)	Nortek AWAC	1 Hz with 2048 s burst every 3600 s; current profile every 5 min, 30 bins at 0.5 m; velocity sample height: 1.04 m
		RBRVirtuoso D	Continuous sampling at 1 Hz; pressure sample height: 0.2 m
S2	(reef flat ~1.5 m)	Nortek ADV	8 Hz with 2048 s burst every 3600 s; velocity sample height: 0.23 m, 0.53 m and 0.85 m.
		Nortek ADP-HR	Continuous 1 Hz current profile, 31 cells at 25 mm, velocity sample height: 0.22 m; pressure sample height: 0.07 m
		Wetlabs FLNTU	0.29 Hz with 462 samples every 3600 s; sample heights: 0.37, 0.64, 0.90 m
		Suction samples	Hourly during daylight; SSC sample heights: 0.22, 0.27, 0.34, 0.51, 0.76, 1.02 m.

[#] Samples heights are relative to the seabed

Field study

The field study consisted of two main components: (1) a detailed study of the hydrodynamics and sediment transport of the reef flat, and (2) a broader-scale hydrodynamic and sediment transport study throughout the reef and lagoon (Pomeroy, 2016). The results presented in this paper focus on the first component, which was based on intensive sampling conducted on the reef flat (S2, Figure 2b) that was designed to quantify the fine-scale sediment dynamics over the reef.

A ‘sawhorse’ instrument frame was deployed at S2 in a water depth of ~ 1.5 m (Figure 2.2e,f). Here the bed roughness is ~ 20 – 40 cm high. Hydrodynamic measurements were obtained using three vertically-distributed Nortek acoustic Doppler velocimeters (ADV). The bottom ADV was located within the roughness sublayer ($z = 0.2$ m), the middle ADV was located near the top of the roughness elements ($z = 0.5$ m) and the top ADV was located high in the water column ($z = 0.8$ m). The ADVs sampled at 8 Hz for 2048 s each hour. In addition to the ADVs, an upward facing Nortek high-resolution acoustic Doppler profiler (ADP) located slightly to north (~ 2 m) of the sawhorse frame sampled continuously at 1 Hz using 25 mm bins with the bottom bin located 0.22 m above the bed. Suspended sediment concentrations were inferred from three WetLabs ECO-FLNTU optical backscatter sensors (OBSs) that sampled at 0.3 Hz for 20 min each hour. Suspended sediment samples were collected *in situ* using a suction sampling array that consisted of six 5 mm diameter intakes that were vertically positioned with logarithmic spacing, oriented perpendicular to the dominant mean flow direction, with water pumped to a scaffold platform nearby. Based on the intake diameter and volume flow rate, the intake flow velocity was approximately 0.6 m s^{-1} , or 2–3 times greater than measured root-mean-squared (RMS) velocities (see below); therefore, errors due to inefficiencies or bias in particle capture are expected to be small (Bosman et al., 1987). A summary of the instrumentation and sampling information is provided in Table 2.1.

In an $\sim 40 \text{ m} \times 40 \text{ m}$ region surrounding the sawhorse frame, a fine-scale topographic survey was used to quantify the bottom roughness. The bathymetry was measured (Figure 2.2c) with single-beam acoustic sonar (Humminbird 798c) and supplemented with four manually-measured roughness transects spaced at ~ 1.5 m horizontally (Figure 2.2d). Each manual transect was defined by an 8 m wire that was tensioned and levelled. The distance between the bed and the wire was measured every 1 m horizontally with 1 cm vertical resolution. The roughness survey indicates that the coverage in benthic roughness varied and consequently the roughness characteristics were somewhat patchy with slightly larger roughness elements (in vertical dimension) located upstream of the sampling site.

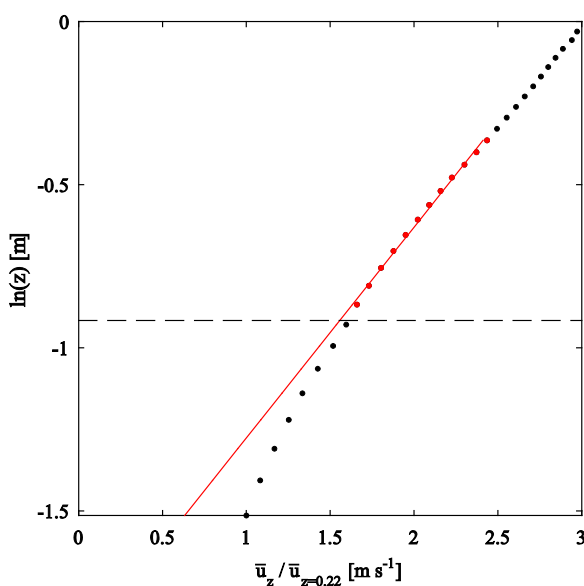


Figure 2.3.

A logarithmic fit of Eq. (2) (red) to the mean of the individual 15-min time-averaged velocity profiles measured during the experiment. The velocity measurements are normalized by the velocity measurement closest to the bed. The red dots denote the points used in the fit and the horizontal dashed line indicates 0.4 m above the bed, the approximate height of the roughness observed at the site.

Data analysis

Hydrodynamic data

Offshore wave conditions (wave height, period and direction) were measured on the foreereef (S1) using a Nortek acoustic wave and current meter (AWAC) with acoustic surface tracking (AST); whereas wave conditions on the reef flat were obtained from pressure time series converted to surface elevations using linear wave theory. From the wave spectra, the root-mean-squared (RMS) wave-heights for the shorter-period (5–25 s) sea-swell waves ($H_{rms,sw}$) and longer period (25–250 s) infragravity ($H_{rms,ig}$) waves, as well as the peak period (T_p), were calculated through integration of the energy within these respective bands.

The raw ADV and ADP velocity measurements were initially filtered based on low signal correlations (< 60%) before velocity spikes (e.g., caused by bubbles or debris in the sample volume) were removed using a kernel-based despiking algorithm (Goring and Nikora, 2002). The direction of the waves and currents were computed separately so that the angle between the waves and currents could be considered in the calculation of the bed shear stresses imposed by the wave-current boundary layer. For each 15-minute burst of data, the mean current (\bar{u}) speed and direction were computed. The reef flat free-stream velocity (\bar{u}_∞) was defined as the depth-averaged current speed of the top five ADP cells unaffected by the free surface (i.e. roughly 0.7–0.8 m above the sediment bed). The mean current vector was then removed from each velocity record and the (residual) oscillatory velocity data rotated into a coordinate system that maximized the velocity variance along the primary axis. In this coordinate system, the wave (\tilde{u}) and RMS velocities (\tilde{u}_{rms}) were determined.

Across a range of conditions, a logarithmic velocity profile was consistently observed within a region approximately 0.5–0.8 m (~12 data points) above the bed (

Figure 2.3). Above the upper height, the flow profile at times deviated from a logarithmic form as it approached a free-stream velocity; below the lower height, the flow profile was often inflected, consistent with a canopy flow (e.g., Figure 2.1). This transition towards the in-canopy flow occurred at an elevation that was comparable to the measured height of the roughness near the site (~20–40 cm). To determine the mean shear velocity above the roughness sublayer ($u_{*m,rough}$) for the combined wave-current flow (see Section 2.3), a least-squares best fit of Eq. (1) against the time-averaged 15 min bursts of the ADP data within the logarithmic region (0.5–0.8 m above bed) was conducted. To ensure a robust logarithmic profile existed, we only retained estimates of $u_{*m,rough}$ from profiles with a $R^2 > 0.95$, with the vast majority (~90%) of the bursts satisfying this criterion. The boundary layer theory of Grant and Madsen (1979) and the implementation described by Madsen (1994) was used to calculate $u_{*max,rough}$. We used \bar{u} and u_{rms} measured above the logarithmic layer ($z = 0.8$) and the z_{0a} from the logarithmic fit to define an equivalent Nikuradse roughness (i.e., $k_N = 30z_{0a}$).

Estimates of $u_{*m,rough}$ were compared to those calculated from the turbulence data measured by the ADVs. Here we further separated the measured horizontal and vertical data into wave (\tilde{u} and \tilde{w}) and turbulent velocity (u' and w') components. We used data from the top and middle ADVs for this decomposition, whereby the turbulent motion was obtained by removing correlated motions between the two instruments (i.e., waves) (Shaw and Trowbridge, 2001). The mean shear velocity enhanced by waves and currents was then determined from the Reynolds stresses ($u_{*m,rough}^2 = -\overline{u'w'}$) at the middle ADV ($z = 0.5$ m). At this elevation, the Reynolds stresses are expected to be slightly below the inertial sublayer (logarithmic) region and representative of the shear velocity just above the roughness elements.

The bottom ADV located below the roughness height was of poorer quality, so it was only used to evaluate the mean current and wave velocities, but not to obtain direct estimates of the Reynolds stresses. To estimate the magnitude of the mean ($u_{*m,bed}$) and maximum wave-current shear velocity ($u_{*max,bed}$) at the sediment bed (at the base of the canopy, Figure 2.1d), we again used the approach described by Madsen (1994) but now with the velocities measured by the bottom ADV. For this flow within the canopy, the roughness was defined with the Nikuradse sand grain roughness ($k_N = 2.5D_{50}$) determined from the median bed grain size measured at the bed level between the roughness elements ($D_{50} \cong 240 \mu\text{m}$, Figure 2.8b).

Suspended sediment grain sizes and concentrations

Suspended sediment grain sizes and concentrations were determined from suction samples at hourly intervals during daylight hours. The water samples were collected with peristaltic pumps via intake ports located perpendicular to the dominant cross-reef flow direction (Bosman et al., 1987) and stored in 2 L bottles. The samples were vacuum filtered onto pre-weighed membrane filters (Whatman ME27, 0.8 μm), dried (75°C for 24 hrs) and weighed in order to calculate SSCs. The dried filters were then imaged under a microscope to obtain ~50 evenly spaced images of the filter surface that were obtained with an accuracy of 2 pixels : 1 μm . For each image, the sediment grains were manually identified under a microscope and their location recorded on the image. A Canny edge detection algorithm (Canny, 1986) was then used in MATLAB to detect the edge of the particles in each image based on local maxima of the image intensity gradient. The largest and smallest dimension of the irregularly shape particles was manually identified in order to determine the size of the particles. Particles with dimensions <50 μm were omitted, as it was often difficult to identify a clearly defined particle boundary and thus these particles could not be reliably measured.

To relate the suspended sediment grain size distribution to the shear stresses above and within the canopy, we determined the equivalent grain size that could be suspended by a given shear velocity based on the downward particle fall velocity (w_s):

$$(1.3)$$

where α represents the different stages of suspension and ranges from bursts of sediment in suspension when $\alpha \leq 1$ to fully-developed suspension when $\alpha \gg 1$ (Bagnold, 1966; Van Rijn, 1984). Note that this ratio is related to the inverse of the Rouse number. We set $\alpha = 1$ based on the following arguments: (1) For a specific grain size to be suspended from the bed it must have experienced a shear stress that was sufficient to enable it to be mobilized from the bed. (2) For the range of sediment grain sizes measured in suspension in this experiment, once these grains are mobilized they (theoretically) directly enter a state of suspension (e.g., Bagnold, 1966; Francis, 1973). (3) The state of suspension (i.e., whether sediment is in a burst or fully-developed suspension) is not relevant for the current analysis. Here we use the Soulsby (1997) formulation to estimate w_s as:

$$w_s = \frac{\nu}{D} \left(\sqrt{10.36^2 + 1.049 D_*^3} - 10.36 \right) \quad (1.4)$$

where ν is the kinematic viscosity of the water ($9.35 \times 10^{-7} \text{m}^2 \text{s}^{-1}$), D is the particle size of interest and D_* is the dimensionless grain size ($D_* = (g(s-1)/\nu^2)^{1/3} D$) with g the gravitational acceleration constant and s is the ratio of the carbonate sediment grain density ($\rho_s = 2600 \text{kg m}^{-3}$) estimated by gravitational displacement (Cuttler et al., 2015) to water density ($\rho_w = 1026 \text{kgm}^{-3}$) from sediment samples obtained at the site.

The OBS and ADP backscatter data were calibrated with the SSC measurements obtained by suction sampling. The known SSCs obtained through filtration were related via linear regression (Table 2.2) to the measured backscatter, time-averaged over the duration when the suction samples were obtained. For the OBS instruments, the suction sample intake port that was closest (vertically) to the optical measurement elevation was used in the calibration, whereas for the ADP data (corrected for acoustic decay (e.g., Ha et al., 2011)) we related three measurement cells to their adjacent intake ports and then applied the mean linear-fit equation to the data. The Root Mean Squared Error (RMSE) of the calibrated OBS and ADP backscatter was ~0.20 mg L^{-1} for all instruments, except for the middle OBS that was slightly lower (~0.13 mg L^{-1}); these errors were much smaller than the typical measurements that ranged from 0.5–8 mg L^{-1} (Section 4.2.2). The calibrated backscatter therefore provided a reasonably accurate measure of SSCs in this experiment due to the narrow distribution of fine sediment at low concentration that we observed (see below) (e.g., Francois and Garrison, 1982; Richards et al., 1996).

Table 2.2. Calibration parameters used for the linear conversion of the ADP and OBS backscatter data (B_k) to suspended sediment concentrations (SSC). For the ADP, the nearest cell to the suction port was used in the calibration while the nearest port to the OBS sample cell was used for the OBS calibration.

$z_{\text{instrument}}^{\#}$ (m)	z_{port} (m)	Calibration Equation (mg L^{-1})	R^2	p	n
ADP					
0.52	0.51	$SSC = 0.052 B_k - 2.68$	0.61	<0.001	35
0.77	0.76	$SSC = 0.062 B_k - 3.25$	0.64	<0.001	31
1.02	1.01	$SSC = 0.067 B_k - 3.53$	0.61	<0.001	28
OBS					
0.37	0.34	$SSC = -0.95 B_k + 6.59$	0.76	<0.001	10
0.64	0.76	$SSC = -0.64 B_k + 4.72$	0.73	<0.001	11
0.90	1.02	$SSC = -2.73 B_k + 9.52$	0.51	0.109	5

[#]cell height corrected for difference in bathymetry between suction sample ports and ADP which is estimated to be ~0.20 m.

2.4 Results

Hydrodynamic conditions

During the first part of the experiment (1–5 August 2013), the offshore RMS wave heights ($H_{rms,sw}$) measured on the forereef at S1 were small and relatively consistent (~0.5–0.8 m, Figure 2.4b). Two larger swell events (6–8 August 2013 and 9–11 August 2013) occurred during the latter part of the experiment, with maximum wave heights reaching ~1.7 m during both events. Peak periods (T_p) ranged from 12 s during lower wave conditions to up to 19 s during the larger swell events (Figure 2.4b). There was a large reduction in sea-swell wave heights ($H_{rms,sw}$) on the reef flat at S2 (Figure 2.4d). Variations in the water depth, predominantly driven by the tide (Figure 2.4a,c), strongly modulated $H_{rms,sw}$ on the reef flat through depth-limited wave breaking (Figure 2.4d); however, the infragravity wave heights ($H_{rms,ig}$) were not strongly modulated by the water depth, responding much more to the offshore $H_{rms,sw}$. As a consequence, the $H_{rms,sw}$ on the reef flat were larger than $H_{rms,ig}$ during high tide, but were similar or smaller than $H_{rms,ig}$ at low tide during the larger swell events.

Mean free-stream current velocities (\bar{u}_{∞}) on the reef flat varied in response to the offshore wave conditions (~0.05–0.45 m s^{-1}) as a result of the dominant wave-driven currents on the reef flat, with only small variability associated with the tides (typically by $\pm 0.05 \text{ m s}^{-1}$) (Figure 2.4e). Thus, during the first part of the experiment the flows tended to be dominated by wave orbital velocities ($\bar{u}_{\infty}/\tilde{u}_{rms} < 1$, where \tilde{u}_{rms} is the RMS value of the wave velocity, Figure 2.4f). At low tide, the combined effect of smaller waves and the relative increase in mean flow resulted in mixed wave-current conditions ($\bar{u}_{\infty}/\tilde{u}_{rms} \sim 1$). During the larger offshore swell events, due to the depth-limitation of wave heights on the reef flat and stronger wave-driven mean currents, the reef flat became current-dominated ($\bar{u}_{\infty}/\tilde{u}_{rms} > 1$) over much of this period.

Hydrodynamic conditions

Above the roughness

The mean current profile above the roughness was consistently logarithmic over the full range of current and wave conditions (~90% of the data conformed to Eq. (2.1) with an acceptance threshold of $R^2 > 0.95$). The mean shear velocities ($u_{*m,rough}$) estimated from Eq. (2.1) usually agreed well with those derived from the ADV-derived Reynolds stresses throughout the experiment (Figure 2.5a). When these $u_{*m,rough}$ values are converted to a bottom friction coefficient ($C_f = u_{*m,rough}^2/\bar{u}_{\infty}^2$), the mean value for the duration of the experiment was 0.035 (standard deviation 0.012). These C_f are within the range (O(0.01)) that are typically reported for other

reef flats (e.g., Lowe and Falter, 2015 for a review). This suggests that the dynamics observed in this experiment are unlikely to be unique to this site.

Values of $u_{*m,rough}$ estimated from the log-fitting increased approximately linearly with mean current speed and were maximum when $\bar{u}_{\infty} \sim 0.3 \text{ m s}^{-1}$; however, appeared to slightly decrease for the largest values of \bar{u}_{∞} , albeit with more scatter (Figure 2.5b). Furthermore, for a given value of \bar{u}_{∞} , $u_{*m,rough}$ increased as the hydraulic roughness (z_{0a}) increased. This increase in z_{0a} occurred as the conditions became more wave-dominated (Figure 2.5c). The increase in both $u_{*m,rough}$ and z_{0a} under stronger wave conditions is consistent with the enhancement of the mean bottom stresses (and apparent bottom roughness) by waves. We note that the current direction varied slightly throughout the experiment (only by $\pm 10\text{--}20^\circ$), thus changes in upstream roughness may also affect the estimated bottom stress and could account for some of the scatter observed.

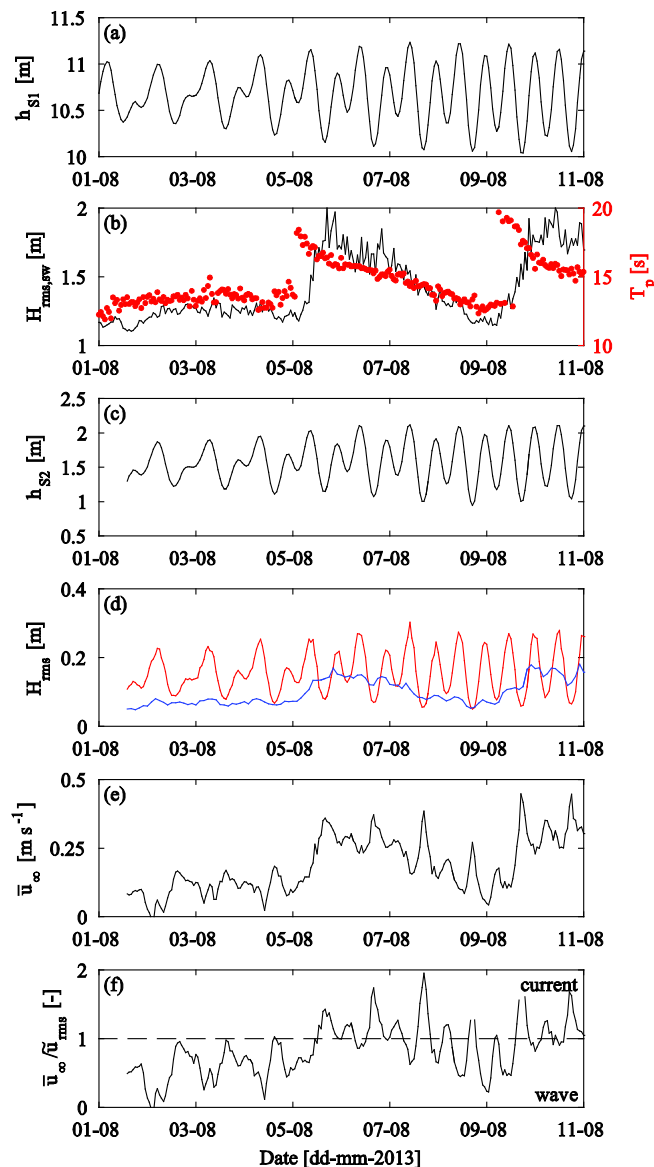


Figure 2.4. The fore reef S1 (a) water depth and (b) swell root-mean-squared (RMS) wave height $H_{rms,sw}$ and peak wave period T_p , along with the intensive sampling reef flat S2 site (c) water depth, (d) sea-swell ($H_{rms,sw}$, red) and infragravity ($H_{rms,ig}$, blue) RMS wave height, the (e) free-stream velocity defined as the depth-averaged velocity above the identified logarithmic region and (f) the relative importance of the free-stream mean flow versus the RMS wave-induced flow. The dashed horizontal line indicates the threshold above which the conditions are current-dominated.

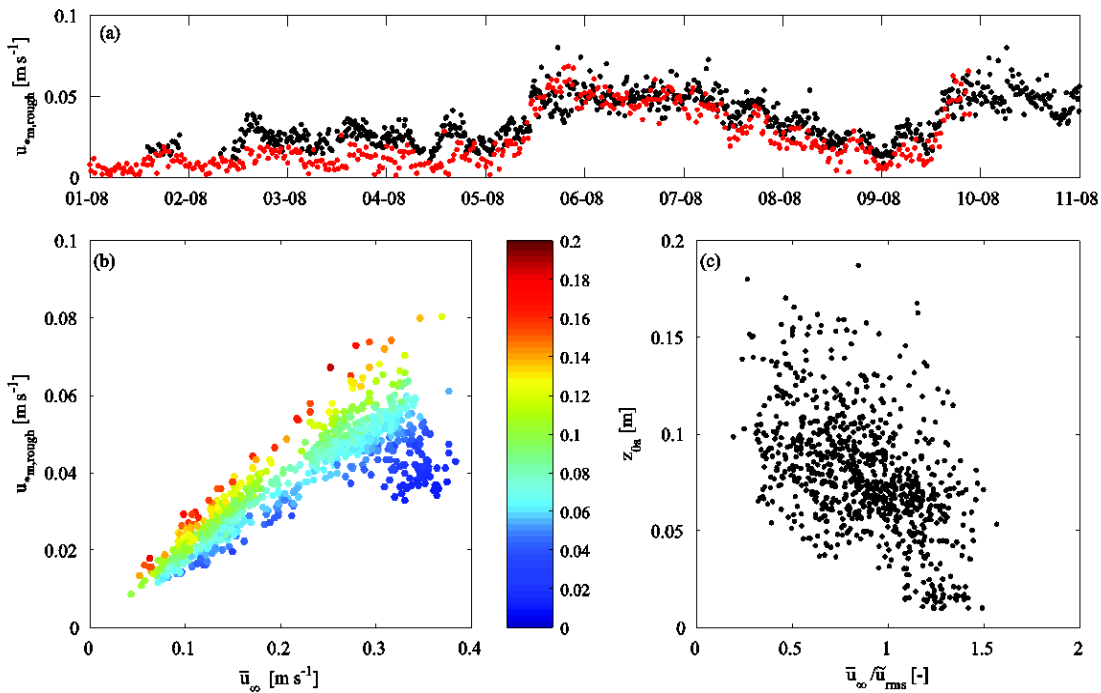


Figure 2.5. The shear velocity ($u_{*m,rough}$) estimated from the middle ADV Reynolds stress (red) compared with the $u_{*m,rough}$ estimated from the ADP time-averaged velocity profiles with Eq. (1) (black). (b) $u_{*m,rough}$ as a function of the free-stream velocity (\bar{u}_{∞}). The colorbar denotes values of the roughness length scale (z_{0a}) (d) The roughness length scale (z_{0a}) as a function of the current-wave ratio ($\bar{u}_{\infty}/\tilde{u}_{rms}$). Note that all values in (b) and (c) are based on estimates from the ADP data.

Within the roughness

Within the roughness (canopy) region, there was greater attenuation of the mean current relative to free stream values when compared to the wave velocities (Figure 2.6). In this near-bed region, the currents were generally reduced to only $\sim 25\%$ of the free-stream velocity (Figure 2.6 a,b), whereas the RMS wave velocities generally remained $\sim 75\%$ of the free stream values (Figure 2.6 c,d).

The estimated mean shear velocity imposed on the underlying sediment bed ($u_{*m,bed}$) was approximately four times smaller than the mean shear velocity at the top of the roughness ($u_{*m,rough}$, Figure 2.7a). Similarly, the maximum wave-induced shear velocity was much larger at the top of the canopy ($u_{*max,rough}$) than at the bed ($u_{*max,bed}$, Figure 2.7b). When the shear velocities at the bed were compared, $u_{*max,bed}$ was approximately twice as large as $u_{*m,bed}$ (Figure 2.7c). We note here that while there is some spatial variability in the velocity measured by the ADV and ADP (Figure 2.6), likely due to fine-scale spatial variations in the roughness, this velocity variability is small. Thus, any differences in shear stresses estimated by the ADV and ADP will also be small, relative to the large vertical differences in the shear stress (i.e., at the bed and at the top of the canopy).

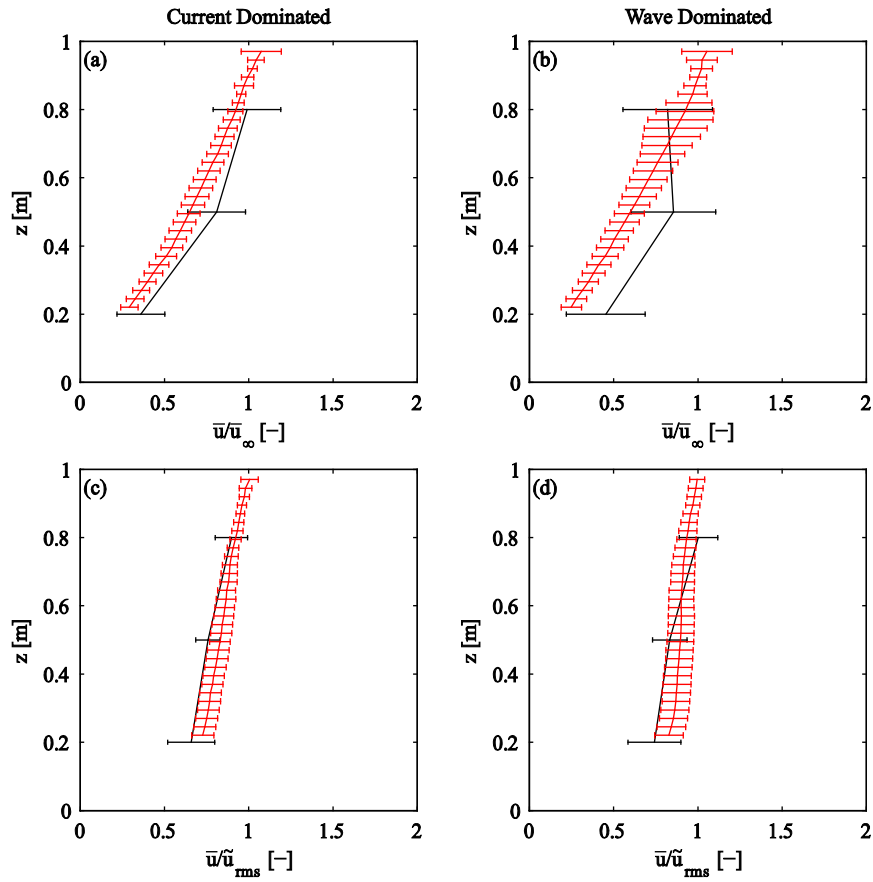


Figure 2.6. Mean current (\bar{u}) profiles for (a) current- and (b) wave-dominated conditions along with RMS velocity (\tilde{u}_{rms}) profiles for (c) current- and (d) wave-dominated conditions. For all profiles, the ADP measurements are shown in red and the ADV measurements are shown in black with the horizontal error bars denoting ± 1 standard deviation. The mean current profiles have been normalized by the free-stream current (\bar{u}_∞) and the RMS velocity profiles have been normalized by \tilde{u}_{rms} above the roughness.

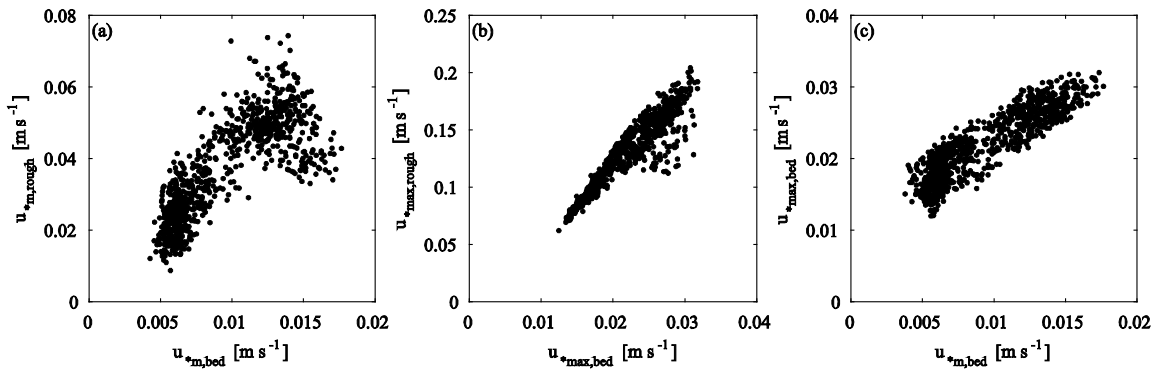


Figure 2.7. (a) The mean shear velocity at the bed ($u_{*m,bed}$) compared to the mean shear velocity at the top of the roughness ($u_{*m,rough}$). (b) The maximum shear velocity at the bed ($u_{*max,bed}$) compared to the maximum shear velocity at the top of the roughness ($u_{*max,rough}$). (c) $u_{*m,bed}$ compared to $u_{*max,bed}$.

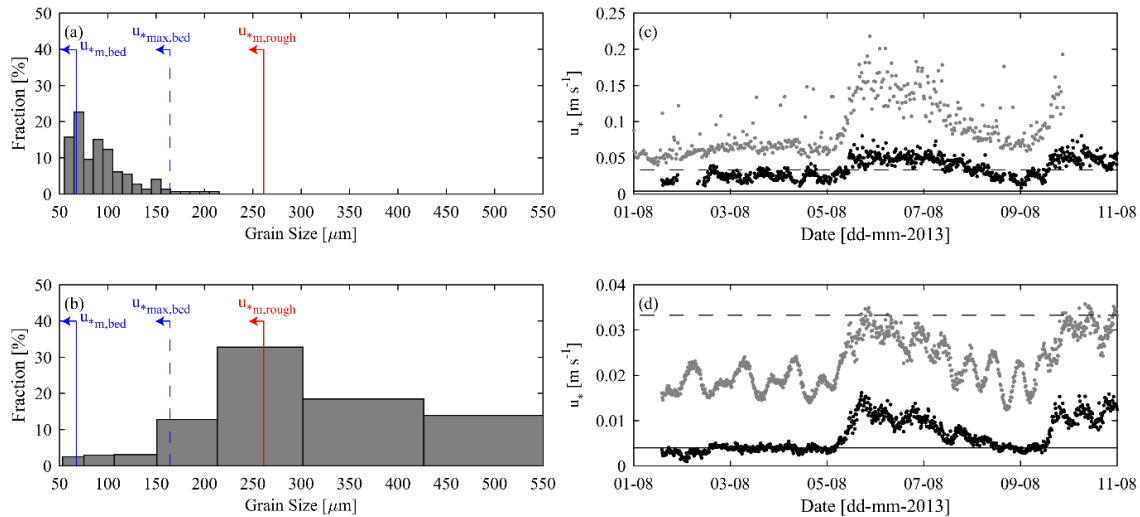


Figure 2.8. Grain size distribution from (a) suction samples obtained at the port closest to the bed ($z = 0.23$ m) and (b) determined from a bed surface sample obtained on the reef flat at S2. The histogram in (a) represents the distribution from a sample obtained at 15:00 on 2 August 2013 (local time). The vertical lines indicate the equivalent sediment diameter that could be suspended by the mean ($u_{*m,bed}$) (solid blue) and maximum ($u_{*max,bed}$) (dashed blue) wave-induced bed shear velocities, and the mean shear velocity ($u_{*m,rough}$) (solid red) at the top of the roughness (canopy) layer. Note that the equivalent grain size that could be maintained in suspension by the maximum wave-induced shear velocity ($u_{*max,rough}$) at the top of the roughness layer is ~ 830 μm and is not indicated on the figure. The maximum (grey) and mean (black) shear velocity at the top of the roughness layer (c) and within the roughness layer (d) are shown for the entire experiment. The horizontal dashed line indicates the shear velocity required to suspend the median bed grain size, while the solid grey line indicates the shear velocity required to suspended the median grain size observed in the suction samples.

Suspended sediment

Grain size distributions

The grain size distributions obtained from the suction samples were similar across the various samples analyzed in the experiment. Although a small number of larger grains were identified in the microscope analysis, $\sim 50\%$ of the grains were within the range of 60–85 μm , with a typical median grain size (D_{50}) of ~ 70 μm (Figure 2.8a). We expect there to be some material that is finer than 50 μm (the lower limit of the analysis) that would shift the median slightly finer; however, we only observed a very small amount of material at 50 μm , so we do not expect this contribution to affect the results. The maximum contribution of the larger grains (>150 μm) was consistently less than 10% for each of the analyzed samples. This is in contrast to the distribution of the bed sediment at this site, which was dominated by much coarser sediment mostly ranging from ~ 150 –500 μm ($D_{50} = 240$ μm) (Figure 2.8b).

The $u_{*m,rough}$ was predicted to be well-beyond what was needed to maintain much of the bed sediment in suspension, as determined from the fall velocity in Eq. (3) (red solid line, Figure 2.8b); however, these larger grain sizes were notably absent from the water column (Figure 2.8a). The absence of these large size fractions in suspension indicates that the shear stress applied to the sediment was substantially smaller than the mean shear at the top of the roughness. This discrepancy is even greater if we consider $u_{*max,rough}$, which would be capable of suspending sediment up to $D_{50}=550$ –1000 μm (off the scale in Figure 2.8a).

The grain sizes observed in the water column were much closer to the equivalent grain size that could be maintained in suspension by $u_{*m,bed}$ (blue solid line, Figure 2.8a). However, we also note that a substantial proportion of the suspended sediment distribution remained above this estimate. If the enhanced shear velocity due to waves ($u_{*max,bed}$) is considered, the range of grain sizes that could be maintained in suspension encompasses almost the entire suspended sediment distribution that was observed (blue dashed line, Figure 2.8a).

The relationship between the shear velocities and the measured SSC samples were also consistent throughout the duration of the experiment: $u_{*m,rough}$ was sufficient to suspend the observed D_{50} that was in suspension and the seabed D_{50} during the swell events; $u_{*max,rough}$ was consistently large enough to suspend the seabed D_{50} (Figure 2.8c). Within the roughness, $u_{*m,bed}$ alone was sufficient to suspend the observed D_{50} that was in suspension, however the addition of the wave component of the enhanced bed stress is clearly evident throughout the time series but remained insufficient (except at the peak of the swell events) to suspend the seabed D_{50} (Figure 2.8d).

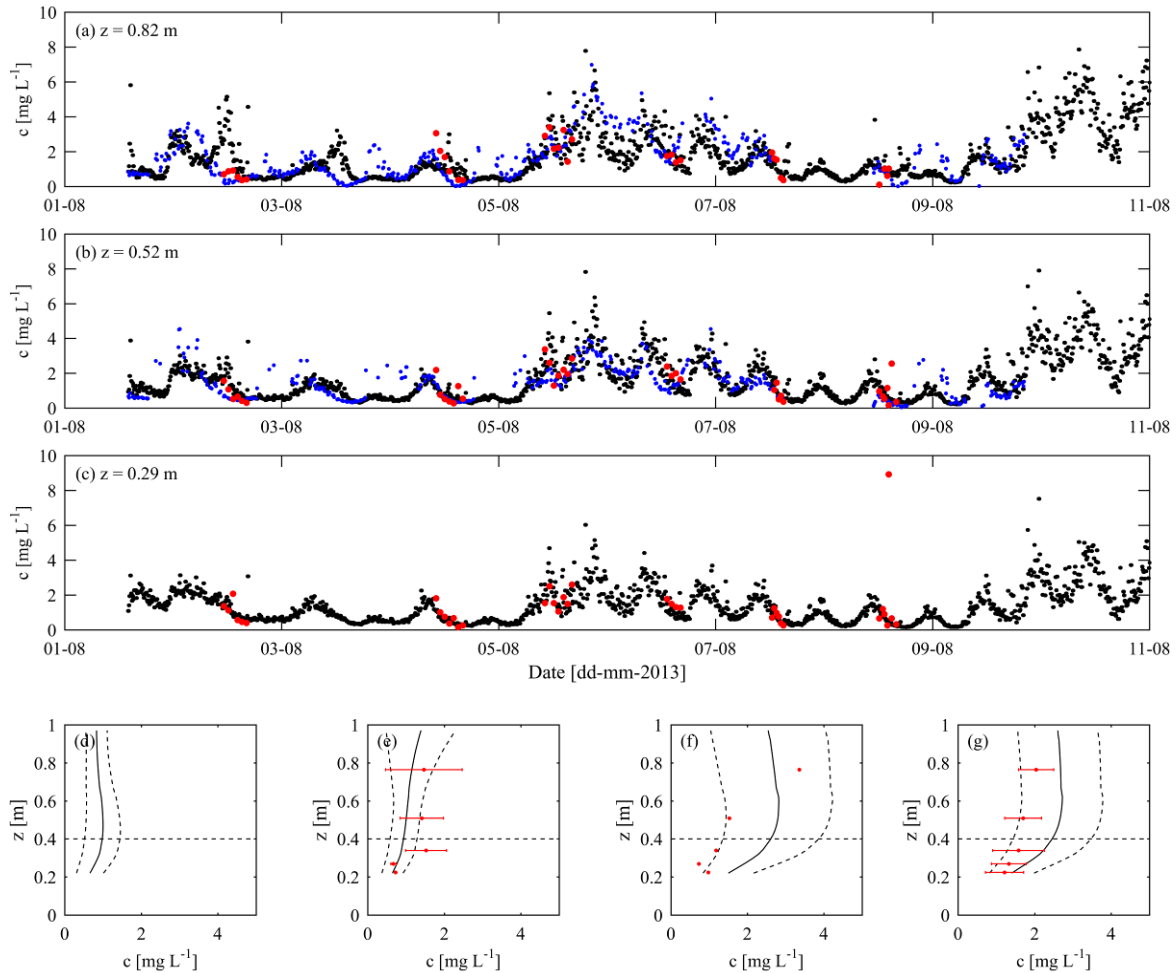


Figure 2.9. Suspended sediment concentration (SSC) time series measured at (a) $z = 0.82$ m, (b) $z = 0.52$ m and (c) $z = 0.29$ m above the bed. The black dots indicate the SSC estimated from the calibrated ADP, blue dots the OBS backscatter and the red dots indicate the directly measured SSC from the suction samples. The mean SSC profile measured by the calibrated ADP (black line) and directly from the suction samples (red dots) for the forereef conditions: (d) low waves and rising tide (note: no suction samples were obtained for this condition), (e) low waves and falling tide, (f) high waves and rising tide and (g) high waves and falling tide. The vertical dotted lines and error bars indicate one standard deviation in the measured data. The horizontal dotted line indicates the approximate height of the roughness.

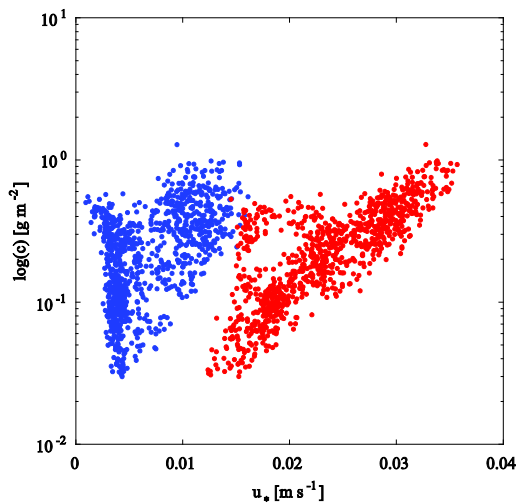


Figure 2.10. Depth-integrated suspended sediment concentration (SSC) within the roughness ($z = 0.2\text{--}0.4\text{m}$) determined from the ADP backscatter compared to the mean bed shear velocity (blue) and maximum bed shear velocity (red).

Sediment concentrations and fluxes

The calibrated ADP and OBS backscatter data were consistent with the SSCs measured directly by suction sampling throughout the experiment (Figure 2.9a-c). Early in the experiment when the waves were low (1–6 Aug), the SSC varied from $\sim 0.5\text{ mg L}^{-1}$ at low tide to $\sim 2\text{--}3\text{ mg L}^{-1}$ at high tide. During the larger swell events spanning 5–8 Aug and 9–12 Aug, the SSCs were consistently higher and peaked at $\sim 8\text{ mg L}^{-1}$ but continued to vary with tidal phase.

The form of the concentration profile defined by the ADP backscatter and the suction samples was grouped according to four hydrodynamic conditions: (I) low offshore waves and rising tide (Figure 2.9d), (II) low offshore waves and falling tide (Figure 2.9e), (III) high offshore waves and rising tide (Figure 2.9f) and (IV) high offshore waves and falling tide (Figure 2.9g). For condition (I), no direct suction samples were obtained during the field experiment, so only profiles derived from the calibrated ADP are shown. For each of the remaining conditions, the time-averaged SSC profile inferred from the calibrated ADP backscatter was comparable in structure to the mean SSC profile described by the suction samples. Each concentration profile exhibited similar features: near the bed, the concentration was low but increased slightly with height above the bed; then above the roughness sublayer, a near constant concentration was observed. There was a very strong relationship between the depth-integrated SSC within the roughness ($z = 0.2\text{--}0.4\text{ m}$) and both $u_{*m,bed}$ and $u_{*max,bed}$ (

Figure 2.10). However, no clear relationship was observed when $u_{*m,bed}$ was small ($<0.005\text{ m s}^{-1}$), i.e. when the wave contribution was also small.

2.5 Discussion

Few studies have directly measured sediment transport over large roughness, especially in a natural field setting. However, the presence of roughness has been thought to decrease sediment transport rates through the attenuation of velocity and turbulence within the roughness sublayer (i.e., the canopy) in terrestrial (e.g., Prosser et al., 1995), riverine (e.g., Neary et al., 2011), and estuarine (e.g., Ward et al., 1984) environments. Of the studies that have specifically considered sediment transport within canopies, most have been from unidirectional laboratory-based experiments that only consider bulk sediment transport rates from changes in the bed morphology or sediment traps, with most attention also focused on emergent canopies (e.g., Baptist, 2005; Jordanova and James, 2003; Le Bouteiller and Venditti, 2015; Widdows et al., 2008). This present study provides new quantitative insight into how suspended sediment grain sizes, SSCs, and SSFs are modified by the presence of submerged roughness on a coral reef flat that is subject to both waves and currents.

Typically, field studies conducted on reefs have empirically related sediment transport rates to shear velocities estimated from hydrodynamics measurements above the roughness (i.e. a measure of the total flow resistance,

including the effect of form drag) (e.g., Ogston et al., 2004; Presto et al., 2006). In this present study we make a direct connection between the observed suspended sediment grain sizes and the reduced hydrodynamic forces present at the sediment bed at the base of the immobile roughness. From these suspended sediment observations, we then determined the shear velocity at the bed required to suspend the observed sediment. Both the mean ($u_{*m,rough}$) and maximum ($u_{*max,rough}$) shear velocities determined from the hydrodynamics above the roughness layer were approximately an order of magnitude larger than those required to suspend the observed grain sizes within the bed, despite none of this material being observed in suspension. Therefore, $u_{*m,rough}$ and $u_{*max,rough}$ were poor predictors of the actual sediment grain sizes that were observed in suspension, whereas estimates obtained using the reduced bed friction velocities ($u_{*m,bed}$ and $u_{*max,bed}$) were much more consistent with the observations.

Although some studies have previously considered how large immobile roughness on the bed can reduce overall bulk sediment transport rates (e.g., Bouma et al., 2007; Le Bouteiller and Venditti, 2015), how this roughness influences suspended sediment transport has remained poorly understood. In the present study, $u_{*m,bed}$ was still not large enough to explain the suspended sediment D_{50} . However, when $u_{*max,bed}$ was considered, almost the entire range of the observed suspended sediment grain sizes were predicted to be in suspension. This suggests that the range and relative proportions of grain sizes in suspension are explained by the wave orbital velocities within the roughness (canopy), and also differences between how wave and current motions dynamically interact within a canopy.

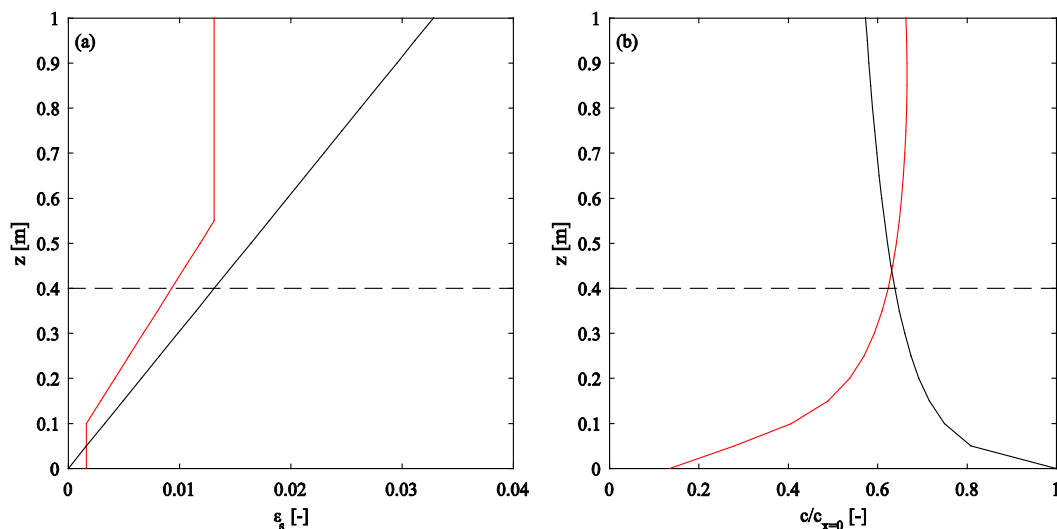


Figure 2.11. (a) Sediment mixing (diffusion) profile (ϵ_s) used in the advection-diffusion model. (b) Suspended sediment concentration (SSC) profiles from the advection-diffusion model with the concentration (c) normalized by the upstream boundary concentration ($c_{x=0}$). (black) no roughness layer in the model and (red) with a roughness layer in the model. The horizontal dotted line denotes the approximate height of the roughness in the model.

The influence of roughness on suspended sediment concentration profiles

The observation of persistently elevated sediment concentrations near the top of the roughness, relative to values near the bed, contrasts with a multitude of observations in other environments (e.g., beaches and rivers) of monotonically decreasing concentration with height above the bed. While this profile may at first appear counter-intuitive, the hydrodynamic influence of the large roughness provides a possible explanation (explored in this section) for the development of this profile.

In flow over an erodible bed for which the ratio w_s / u_* is small, sediment will be entrained from the bed into the water column, where it will be transported (advected) as suspended sediment. At equilibrium, sediment

suspension balances sediment deposition; otherwise, the sediment concentration will vary with streamwise distance until an equilibrium profile is attained. The distribution of sediment in suspension is typically modelled as a vertical diffusive process, which can be described by the advection-diffusion equation:

$$\underbrace{\frac{\partial(uc)}{\partial x}}_1 - \underbrace{\frac{\partial(w_s c)}{\partial z}}_2 - \underbrace{\frac{\partial}{\partial z} \left(\varepsilon_s \frac{\partial c}{\partial z} \right)}_3 = 0 \quad (1.5)$$

In Eq. (2.5), Term 1 describes the horizontal advection of sediment, Term 2 gravitational settling and Term 3 the vertical diffusion of sediment. Here, ε_s is the sediment mixing (diffusion) parameter, which can be approximated (in various forms) as a function of the turbulent eddy viscosity (ν_t) or u_* (e.g., Van Rijn, 1984).

The development of suspended sediment concentration profiles over erodible beds with and without roughness is obtained by solving Eq. (2.5) with an upwind numerical scheme. We consider the case of a uniform sediment concentration upstream of the roughness ($c_{x=0}$) due to, e.g., wave breaking in an upstream surf zone. To solve Eq. (2.5), two boundary conditions are required: (i) at the upper boundary (the free surface) there is zero vertical flux, and (ii) at the bed ($z = 0$), the upward diffusive flux balances gravitational settling (i.e., $w_s c = -\varepsilon_s \partial c / \partial z$). Typically, a near-bed reference concentration (c_0) is used to specify this bottom boundary condition. Many formulations have been developed for c_0 , most of which functionally depend on the shear stress applied to the sediment bed (e.g., Lee et al., 2004; Smith and McLean, 1977). Here, we specified a spatially-constant (i.e., in the stream-wise direction x) c_0 using the formulation proposed by Lee et al. (2004):

$$c_0 = A[\theta u_* / w_s]^B \quad (1.6)$$

where c_0 is defined at a reference height $z_{ref} = 0.01$ m above the bed, θ is the grain roughness Shields parameter and u_* is the shear velocity at the sediment bed. We use $A = 2.58$ and $B = 1.45$ for the two empirically-derived constants, but recognize that there is some uncertainty around these values (Lee et al., 2004).

For comparison, we first determine the concentration profile over a bare erodible bed (i.e. without roughness). Typical values of the uniform mean current ($\bar{u} = 0.3$ m s⁻¹), uniform grain size in suspension (70 μ m) and bed friction velocity ($u_* = 0.08$ m s⁻¹) are used. The sediment diffusivity (ε_s) is assumed to increase linearly with height above the bed (i.e. $\varepsilon_s = \nu_t = \kappa u_{*max,rough} z$, Figure 2.11a). With this diffusivity profile, the initially uniform concentration profile, which in this example we initialize with c_0 , evolves downstream to form a classic exponentially-decaying profile above the bed (Figure 2.11b).

In this study, we typically observed a four-fold difference between $u_{*max,rough}$ and $u_{*max,bed}$ due to the large bottom roughness. The presence of large roughness therefore has two important modifications to the solution to Eq. (2.5). Firstly, τ_{bed} is reduced and consequently so is c_0 . For comparison with the bare bed case, we assume the same maximum value of u_* here at the height of the roughness (i.e. $u_{*max,rough} = 0.08$ m s⁻¹) and a reduced value for $u_{*max,bed}$ (which is used in Eq. 6 to determine c_0) of 0.02 m s⁻¹; as a consequence c_0 is also lower in the presence of the roughness. Secondly, flume experiments have shown that in unidirectional flow over large roughness, the turbulent diffusivity decreases linearly from a maximum value near the top of the roughness to a diminished value deep within the roughness (e.g., Ackerman and Okubo, 1993; Ghisalberti, 2007; Ghisalberti and Nepf, 2004). Accordingly, a two-layer distribution of ε_s was assumed here (Figure 2.11a), where ε_s is lower within the roughness than above it.

The solution to Eq. (2.5) in the presence of large roughness was obtained by assuming the same uniform mean current, suspended sediment grain size, and the initializing condition as in the bare bed case. For this case, the SSC profile evolves from the uniform upstream concentration to a shape where the concentration increases with height above the bed (Figure 2.11b). This is qualitatively consistent with the SSC profiles observed in this experiment (Figure 2.9). Eventually (far downstream) the solution will converge to an exponential profile,

analogous to that observed over a bare sandy bed but with a much lower concentration; for the fine suspended sediments (low settling velocity) observed in this study, that development would occur over large distances.

Thus, a likely explanation for the SSC profiles observed in the field experiment is that the narrow but high energy surf zone located ~ 400 m upstream near the reef crest initially creates a well-mixed distribution of fine suspended sediment that slowly settles out of the water column. This sediment is advected by the cross-reef mean flows over and within the roughness. The reduced bed shear stress within the roughness leads to a reduction in c_o , resulting in a net downward sediment flux by both diffusion and gravitational settling; the divergence in the vertical sediment flux is balanced by a convergence in the horizontal advective flux. It is this reduction in c_o when compared to a larger upstream concentration that results in the reduced SSC values near the bed. These results suggest that the fine sediments ($D_{50} = 70 \mu\text{m}$; coarse silt to fine sand) observed in suspension would likely include contributions from both local resuspension and sediment sourced upstream by advection. The fact that the coarse local bed sediment ($D_{50} = 240 \mu\text{m}$) is not in suspension is also consistent with this model, as the reduced bed shear stress within the roughness was found to be incapable of suspending this coarse sediment fraction.

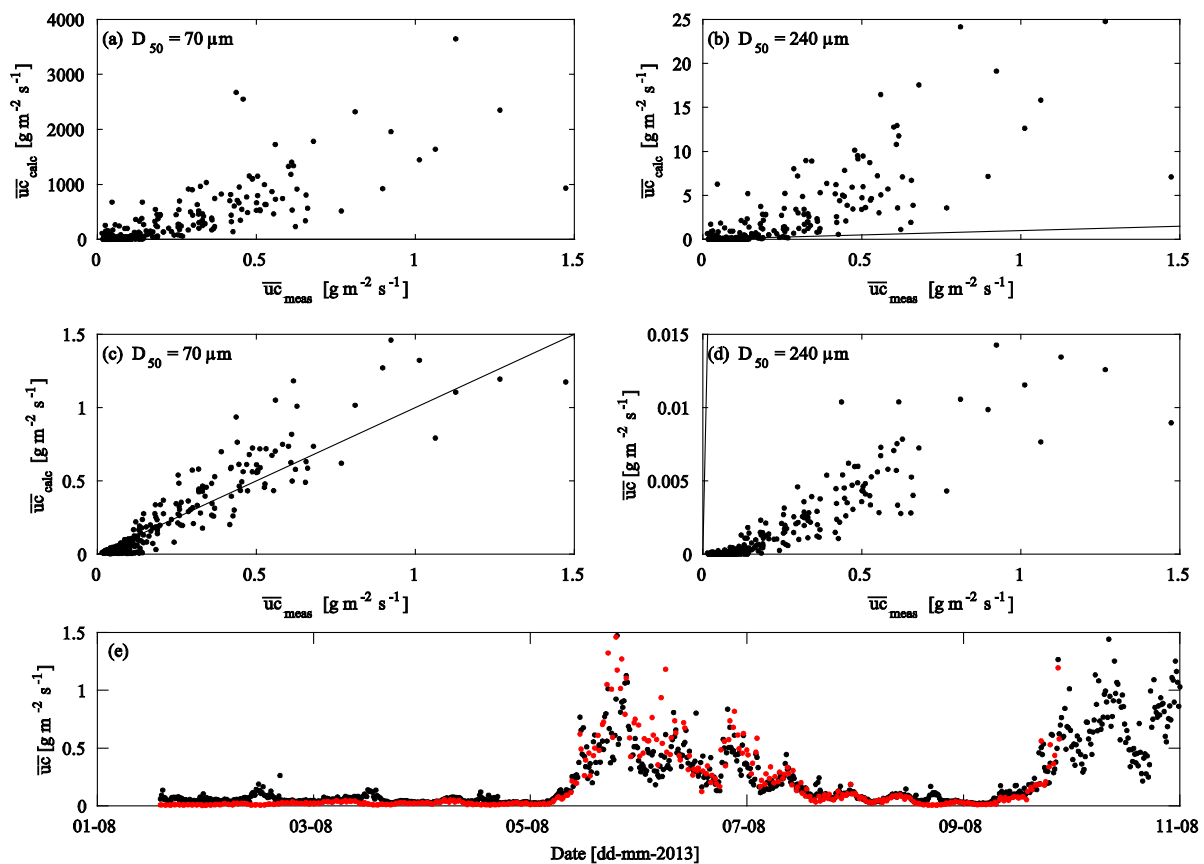


Figure 2.12. (a)-(d) Suspended sediment flux (SSF) on the reef flat compared with the SSF estimated using a power-law profile with the reference concentration (C_o) formulation of Lee et al. (2004), $D_{50} = 70 \mu\text{m}$ or $240 \mu\text{m}$ and (top) $u_{*max,rough}$ and (middle) $u_{*max,bed}$. The solid black line indicates 1:1 agreement. (e) Estimated SSF (red) and measured SSF (black) for the duration of the experiment.

Estimated versus measured suspended sediment fluxes

Physical relationships that describe the hydrodynamics of bare sandy beds are still regularly applied to obtain quantitative estimates of sediment transport within ecosystems with large bottom roughness. It is therefore of particular interest to assess the sensitivity of predictions of SSFs (which integrate the effects of the modified concentration and velocity profiles), to these different definitions of the shear velocity. It is not our intention to conduct an exhaustive review of the applicability of key formulae, but instead to apply the different u_* values from this study in a one-dimensional (vertical) concentration profile model to simply assess the sensitivity of SSF predictions.

The depth-integrated Eulerian-mean SSFs were calculated from local estimates of SSF ($\bar{u}\bar{c}$) that were determined from time-averaged concentrations (\bar{c}) measured directly from the suction sample array and the co-located current velocity data (\bar{u}) measured at the time of sediment sampling by the ADP. We assume that the SSF at the lowest measurement point was representative of the fluxes further below, but recognize the flux could also be higher in this region. These discrete estimates were supplemented with SSFs calculated using 15-min bursts of velocity and the indirectly measured SSCs (calibrated backscatter) from the ADP.

In order to predict the SSF for different u_* values, a SSC profile must be determined, which in turn requires prescription of the near-bed reference concentration (c_0). We specify the reference concentration using the same empirical model of Lee et al. (2004) used earlier (Eq. 2.6). The form of the SSC profile is commonly represented by various solutions to Eq. (2.5) (e.g., exponential, power law, Rouse). We note that such SSC profiles only consider the diffusion and gravitational settling of sediment and do not take into account the advection of sediment from other areas. Here, a commonly employed power-law formulation was used:

$$c(z) = c_0 \left(\frac{z}{z_{ref}} \right)^{-P} \quad (1.7)$$

where z is the height above the bed and $P = w_s / \kappa u_{*,max}$ is the Rouse parameter. We note that this formulation results in a lower SSC higher in the water column than at the bed, which is not consistent with the observations in this experiment. However, we re-emphasize here that the purpose of the present analysis is to evaluate the extent to which the SSF estimates from established approaches (such as the one described by Eq. (2.7)) may deviate from the observations to assess the errors that can be introduced by applying conventional sediment transport formulations to these environments.

The horizontal velocity (\bar{u}) used to estimate the SSF was based on values measured by the ADP and we determined the SSFs following what was done earlier with the field data. We evaluated four cases, where the u_* that was used to calculate c_0 taken as either $u_{*,max,rough}$ or $u_{*,max,bed}$ and with the sediment grain size as either the D_{50} in suspension (70 μm) or the seabed D_{50} (240 μm). The shear velocity used to calculate the Rouse parameter was $u_{*,m,rough}$, which represents the greater mixing expected in the water column.

With the $D_{50}=70 \mu\text{m}$ observed in suspension, the SSFs estimated using $u_{*,max,rough}$ are three orders of magnitude larger than those observed (Figure 2.12a), while for the seabed $D_{50}=240 \mu\text{m}$ the estimated SSF is approximately 1–2 orders of magnitude too large (Figure 2.12b). In contrast, the SSF estimated using the reduced $u_{*,max,bed}$ within the roughness and $D_{50}=70 \mu\text{m}$ observed in suspension was of the correct order of magnitude (Figure 2.12c), an agreement that persisted throughout the experiment (Figure 2.12e). The SSF estimated with the reduced $u_{*,max,bed}$ and the seabed $D_{50}=240 \mu\text{m}$ was underestimated by 1–2 orders of magnitude (Figure 2.12d).

This sensitivity analysis demonstrates that established methods used to estimate SSF will substantially overestimate the flux when the shear stresses are estimated from hydrodynamic measurements that include the large form drag exerted by the roughness (i.e., when the impact of the roughness layer is not specifically considered). However, if the flow structure within the roughness is considered, the estimated SSF for this experiment was much closer and of the correct order of magnitude when the appropriate D_{50} in suspension is considered.

Implications for sediment transport predictions

Existing studies of sediment dynamics in benthic ecosystems with large bottom roughness (e.g., coral reefs) still tend to focus on the long-standing framework for how sediment dynamics operate over bare sediment beds (e.g. as occurs on sandy beaches). There have been considerable advances in predicting how hydrodynamic processes in coral reefs are modified by the presence of large bottom roughness (i.e., how the roughness affects circulation and wave transformation) with emphasis in these hydrodynamic studies generally on correctly representing the hydrodynamic properties above the roughness. This has typically been achieved by adjusting empirical friction

parameters (e.g., by adjusting bottom drag coefficients in models to account for the large bottom roughness (e.g., Lowe et al., 2009a; Van Dongeren et al., 2013)). While this approach may yield a more ‘correct’ reproduction of the hydrodynamic processes (at least above the canopy), this approach will greatly overestimate the bed stresses that act on the sediment, which are directly responsible for driving sediment transport. Therefore, while the presence of the large roughness has the effect of increasing the predicted “bottom” stresses in hydrodynamic models, in reality the roughness would actually have the opposite effect on the sediment transport; that is, the roughness reduces bed shear stresses and thus suppresses sediment transport. While more research is required to develop robust predictive models of sediment transport in the presence of canopies, including how roughness modifies both the turbulent flow structure and bed shear stresses, as a starting point this study has demonstrated how reef roughness can result in a persistence of finer suspended sediments, lower SSCs and lower SSFs than would be predicted from using existing bare-bed sediment transport formulations.

2.6 Conclusions

The importance of sediment suspension and transport within coral reef ecosystems is well established; however, detailed measurements of sediment suspension and transport processes in these environments have been historically very limited. Consequently, the physics employed to describe these processes is typically based upon principles developed for sandy beach environments that are extended to reefs with large roughness (canopies) without a firm theoretical basis. We show that such models are likely to inaccurately quantify (at even an order of magnitude level) both suspended sediment concentrations and sediment fluxes.

In this study, we conducted a detailed field experiment to investigate the turbulent flow structure, SSCs, rates of suspended sediment transport, and size distributions of suspended sediment in a coral reef environment under combined wave-current flow conditions. The key results of this study are as follows:

1. A clear logarithmic velocity layer developed above the reef canopy but did not extend into the canopy; instead the velocity profile was inflected and hence the flow was reduced in the roughness (canopy) region adjacent to the bed.
2. The shear stresses that arise from the large canopy drag forces imposed on the overlying flow do not represent the actual shear stress imparted on the underlying bed sediment. The actual shear stress is substantially smaller than that on a bare bed, as demonstrated by the fineness of the suspended fraction and low SSC concentrations, which could not have been predicted by traditional models.
3. Simple estimation of the wave and current shear stress above and within large roughness vastly improves the predictive capability of established formulae for the grain size and concentration of suspended sediment in reef systems. However, further research is required to improve predictions of the concentration profiles observed in this experiment (higher concentrations above the roughness than within it) and to develop robust sediment transport formulations that can be applied to coral reefs and other analogous ecosystem with large bottom roughness.

2.7 References

- Ackerman, J. D., and A. Okubo (1993), Reduced mixing in a marine macrophyte canopy, *Functional Ecology*, 7(3), 305-309, doi:10.2307/2390209.
- Anthony, K. (2000), Enhanced particle-feeding capacity of corals on turbid reefs (Great Barrier Reef, Australia), *Coral Reefs*, 19(1), 59-67.
- Bagnold, R. (1966), An approach to the sediment transport problem from general physics, *US Geol. Surv. Prof. Pap.*, 422-I, 11-137.
- Baptist, M. J. (2005), *Modelling floodplain biogeomorphology*, TU Delft, Delft University of Technology.
- Bosman, J. J., E. T. J. M. van der Velden, and C. H. Hulsbergen (1987), Sediment concentration measurement by transverse suction, *Coast. Eng.*, 11(4), 353-370, doi:10.1016/0378-3839(87)90033-0.
- Bouma, T., L. van Duren, S. Temmerman, T. Claverie, A. Blanco-Garcia, T. Ysebaert, and P. Herman (2007), Spatial flow and sedimentation patterns within patches of epibenthic structures: Combining field, flume and modelling experiments, *Cont. Shelf. Res.*, 27(8), 1020-1045.
- Canny, J. (1986), A Computational Approach to Edge Detection, *Pattern Analysis and Machine Intelligence, IEEE Transactions on, PAMI-8(6)*, 679-698, doi:10.1109/TPAMI.1986.4767851.
- Chen, Z., A. Ortiz, L. Zong, and H. Nepf (2012), The wake structure behind a porous obstruction and its implications for deposition near a finite patch of emergent vegetation, *Water Resources Research*, 48(9), doi:10.1029/2012WR012224.
- Cuttler, M., R. Lowe, J. Hansen, J. Falter, and A. W. M. Pomeroy (2015), Grainsize, composition and bedform patterns in a fringing reef system, *The Proceedings of Coastal Sediments*.
- Finnigan, J. (2000), Turbulence in plant canopies, *Ann. Rev. Fluid. Mech.*, 32(1), 519-571.
- Francis, J. (1973), Experiments on the motion of solitary grains along the bed of a water-stream, *Proc. Roy. Soc. London, Series A*, 332(1591), 443-471.
- Francois, R., and G. Garrison (1982), Sound absorption based on ocean measurements. Part II: Boric acid contribution and equation for total absorption, *The Journal of the Acoustical Society of America*, 72(6), 1879-1890, doi:10.1121/1.388673.
- Gacia, E., T. C. Granata, and C. M. Duarte (1999), An approach to measurement of particle flux and sediment retention within seagrass (*Posidonia oceanica*) meadows, *Aquatic Botany*, 65(1-4), 255-268, doi:10.1016/S0304-3770(99)00044-3
- Ghisalberti, M. (2007), The impact of submerged canopies on open-channel hydrodynamics, *Proceedings of the 5th International Symposium on Environmental Hydraulics*.
- Ghisalberti, M., and H. Nepf (2004), The limited growth of vegetated shear layers, *Water Resources Research*, 40(7), W075021-W0750212.
- Goring, D., and V. Nikora (2002), Despiking Acoustic Doppler Velocimeter Data, *J. Hydraul. Eng.*, 128(1), 117-126, doi:10.1061/(ASCE)0733-9429(2002)128:1(117).
- Grant, W. D., and O. S. Madsen (1979), Combined wave and current interaction with a rough bottom, *J. Geophys. Res. Oceans*, 84(C4), 1797-1808.
- Ha, H., J.-Y. Maa, K. Park, and Y. Kim (2011), Estimation of high-resolution sediment concentration profiles in bottom boundary layer using pulse-coherent acoustic doppler current profilers, *Mar. Geol.*, 279(1-4), 199-209, doi:10.1016/j.margeo.2010.11.002
- Hardy, T. A., and I. R. Young (1996), Field study of wave attenuation on an offshore coral reef, *J. Geophys. Res. Oceans*, 101(C6), 14311-14326, doi:10.1029/96jc00202.
- Hench, J. L., J. J. Leichter, and S. G. Monismith (2008), Episodic circulation and exchange in a wave-driven coral reef and lagoon system, *Limnol. Oceanogr*, 53(6), 2681-2694.
- Infantes, E., A. Orfila, G. Simarro, J. Terrados, M. Luhar, and H. Nepf (2012), Effect of a seagrass (*Posidonia oceanica*) meadow on wave propagation, *Marine Ecology Progress Series*, 456, 63-72.
- James, C., A. Jordanova, and C. Nicolson (2002), Flume experiments and modelling of flow-sediment-vegetation interactions, *International Association of Hydrological Sciences, Publication(276)*, 3-9.
- James, W. F., J. W. Barko, and M. G. Butler (2004), Shear stress and sediment resuspension in relation to submersed macrophyte biomass, *Hydrobiologia*, 515(1-3), 181-191.
- Jordanova, A., and C. James (2003), Experimental Study of Bed Load Transport through Emergent Vegetation, *J. Hydraul. Eng.*, 129(6), 474-478, doi:10.1061/(ASCE)0733-9429(2003)129:6(474).
- Kothyari, U. C., H. Hashimoto, and K. Hayashi (2009), Effect of tall vegetation on sediment transport by channel flows, *J. Hydraul. Res.*, 47(6), 700-710.

- Le Bouteiller, C., and J. Venditti (2015), Sediment transport and shear stress partitioning in a vegetated flow, *Water Resources Research*, 51(4), 2901-2922.
- Lee, G. h., W. B. Dade, C. T. Friedrichs, and C. E. Vincent (2004), Examination of reference concentration under waves and currents on the inner shelf, *J. Geophys. Res. Oceans*, 109(C2).
- Lowe, R. J., and J. L. Falter (2015), Oceanic Forcing of Coral Reefs, *Annu. Rev. Mar. Sci.*, 7(18), 1-25, doi:10.1146/annurev-marine-010814-015834.
- Lowe, R. J., J. L. Falter, M. D. Bandet, G. Pawlak, M. J. Atkinson, S. G. Monismith, and J. R. Koseff (2005a), Spectral wave dissipation over a barrier reef, *J. Geophys. Res. Oceans*, 110(C04001), doi:10.1029/2004jc002711.
- Lowe, R. J., J. L. Falter, S. G. Monismith, and M. J. Atkinson (2009a), A numerical study of circulation in a coastal reef-lagoon system, *J. Geophys. Res.*, 114, C06022, doi:10.1029/2008jc005081.
- Lowe, R. J., J. L. Falter, S. G. Monismith, and M. J. Atkinson (2009b), Wave-Driven Circulation of a Coastal Reef-Lagoon System, *J. Phys. Oceanogr.*, 39, 873-893.
- Lowe, R. J., J. Koseff, and S. G. Monismith (2005b), Oscillatory flow through submerged canopies: 1. Velocity structure, *J. Geophys. Res. Oceans*, 110(C10016), 1-17, doi:10.1029/2004JC002788.
- Lowe, R. J., U. Shavit, J. L. Falter, J. R. Koseff, and S. G. Monismith (2008), Modeling flow in coral communities with and without waves: A synthesis of porous media and canopy flow approaches, *Limnology and Oceanography*, 53, 2668-2680, doi:10.4319/lo.2008.53.6.2668.
- Luhar, M., S. Coutu, E. Infantes, S. Fox, and H. Nepf (2010), Wave-induced velocities inside a model seagrass bed, *J. Geophys. Res. Oceans*, 115(C12).
- Luhar, M., J. Rominger, and H. Nepf (2008), Interaction between flow, transport and vegetation spatial structure, *Environmental Fluid Mechanics*, 8(5-6), 423-439, doi:10.1007/s10652-008-9080-9.
- Neary, V. S., S. Constantinescu, S. Bennett, and P. Diplas (2011), Effects of vegetation on turbulence, sediment transport, and stream morphology, *J. Hydraul. Eng.*, 138(9), 765-776.
- Nepf, H. M. (2012), Flow and transport in regions with aquatic vegetation, *Ann. Rev. Fluid. Mech.*, 44, 123-142.
- Ogston, A. S., C. D. Storlazzi, M. E. Field, and M. K. Presto (2004), Sediment resuspension and transport patterns on a fringing reef flat, Molokai, Hawaii, *Coral Reefs*, doi:10.1007/s00338-004-0415-9.
- Pomeroy, Andrew W. M. (2016), Tantabiddi Sediment Dynamics Experiment (Ninglao Reef): Hydrodynamic and suspended sediment data, *Zenodo*, Available from: <http://doi.org/10.5281/zenodo.126670>
- Pomeroy, A. W. M., R. J. Lowe, G. Symonds, A. Van Dongeren, and C. Moore (2012), The dynamics of infragravity wave transformation over a fringing reef, *J. Geophys. Res. Oceans*, 117(C11022), doi:10.1029/2012JC008310.
- Presto, M. K., A. S. Ogston, C. D. Storlazzi, and M. E. Field (2006), Temporal and spatial variability in the flow and dispersal of suspended-sediment on a fringing reef flat, Molokai, Hawaii, *Estuarine, Coastal and Shelf Science*, 67, 67-81, doi:10.1016/j.ecss.2005.10.015.
- Prosser, I. P., W. E. Dietrich, and J. Stevenson (1995), Flow resistance and sediment transport by concentrated overland flow in a grassland valley, *Geomorphology*, 13(1), 71-86.
- Raupach, M. R., R. A. Antonia, and S. Rajagopalan (1991), Rough-Wall Turbulent Boundary Layers, *Applied Mechanics Reviews*, 44(1), 1-25, doi:10.1115/1.3119492.
- Richards, S., A. Heathershaw, and P. Thorne (1996), The effect of suspended particulate matter on sound attenuation in seawater, *The Journal of the Acoustical Society of America*, 100(3), 1447-1450.
- Rosman, J. H., and J. L. Hench (2011), A framework for understanding drag parameterizations for coral reefs, *J. Geophys. Res. Oceans*, 116(C08025), doi:10.1029/2010jc006892.
- Roth, M. S. (2014), The engine of the reef: photobiology of the coral-algal symbiosis, *Frontiers in microbiology*, 5.
- Shaw, W. J., and J. H. Trowbridge (2001), The direct estimation of near-bottom turbulent fluxes in the presence of energetic wave motions, *Journal of Atmospheric and Oceanic Technology*, 18(9), 1540-1557.
- Shields, A. (1936), Application of similarity principles and turbulence research to bed-load movement.
- Smith, J. D., and S. McLean (1977), Boundary layer adjustments to bottom topography and suspended sediment, *Elsevier Oceanography Series*, 19, 123-151.
- Soulsby, R. (1997), *Dynamics of Marine Sands: A Manual for Practical Applications*, Thomas Telford, London.
- Soulsby, R., and S. Clarke (2005), Bed shear-stresses under combined waves and currents on smooth and rough beds, *HR Wallingford, Report TR137*.

- Storlazzi, C. D., M. E. Field, M. H. Bothner, M. K. Presto, and A. E. Draut (2009), Sedimentation processes in a coral reef embayment: Hanalei Bay, Kauai, *Mar. Geol.*, 264, 140-151, doi:10.1016/j.margeo.2009.05.002.
- Storlazzi, C. D., A. S. Ogston, M. H. Bothner, M. E. Field, and M. K. Presto (2004), Wave- and tidally-driven flow and sediment flux across a fringing coral reef: Southern Molokai, Hawaii, *Cont. Shelf. Res.*, 24(12), 1397-1419, doi:10.1016/j.csr.2004.02.010.
- Suhayda, J. N., and H. H. Roberts (1977), Wave action and sediment transport on fringing reefs, paper presented at 3rd International Coral Reef Symposium, Miami.
- Symonds, G., K. P. Black, and I. R. Young (1995), Wave-driven flow over shallow reefs, *J. Geophys. Res.*, 100, 2639-2648, doi:10.1029/94jc02736.
- Van Dongeren, A., R. Lowe, A. Pomeroy, D. M. Trang, D. Roelvink, G. Symonds, and R. Ranasinghe (2013), Numerical modeling of low-frequency wave dynamics over a fringing coral reef, *Coast. Eng.*, 73, 178-190, doi:10.1016/j.coastaleng.2012.11.004.
- van Katwijk, M. M., A. R. Bos, D. C. R. Hermus, and W. Suykerbuyk (2010), Sediment modification by seagrass beds: Muddification and sandification induced by plant cover and environmental conditions, *Estuarine, Coastal and Shelf Science*, 89(2), 175-181, doi:10.1016/j.ecss.2010.06.008.
- Van Rijn, L. C. (1984), Sediment transport, Part II: Suspended load transport, *J. Hydraul. Eng.*, 110(11), 1613-1641.
- Van Rijn, L. C. (1993), *Principles of sediment transport in rivers, estuaries and coastal seas*, Aqua publications Amsterdam, Amsterdam.
- Van Rijn, L. C. (2007), Unified view of sediment transport by currents and waves. I: Initiation of motion, bed roughness, and bed-load transport, *J. Hydraul. Eng.*, 133(6), 649-667.
- Ward, L. G., W. M. Kemp, and W. R. Boynton (1984), The influence of waves and seagrass communities on suspended particulates in an estuarine embayment, *Mar. Geol.*, 59(1), 85-103.
- Weber, M., D. de Beer, C. Lott, L. Polerecky, K. Kohls, R. M. Abed, T. G. Ferdelman, and K. E. Fabricius (2012), Mechanisms of damage to corals exposed to sedimentation, *Proceedings of the National Academy of Sciences*, 109(24), E1558-E1567.
- Wiberg, P. L. (1995), A theoretical investigation of boundary layer flow and bottom shear stress for smooth, transitional, and rough flow under waves, *J. Geophys. Res. Oceans*, 100(C11), 22667-22679.
- Widdows, J., N. D. Pope, M. D. Brinsley, H. Asmus, and R. M. Asmus (2008), Effects of seagrass beds (*Zostera noltii* and *Z. marina*) on near-bed hydrodynamics and sediment resuspension, *Marine Ecology Progress Series*, 358, 125.
- Zeller, R. B., F. J. Zarama, J. S. Weitzman, and J. R. Koseff (2015), A simple and practical model for combined wave-current canopy flows, *Journal of Fluid Mechanics*, 767, 842-880.

3 Hydrodynamic drivers of spatial and temporal variability of sediment transport patterns in a fringing coral reef³

Abstract

Despite increased sedimentation pressures on reef ecosystems worldwide, the physical processes that drive spatial and temporal patterns in sediment transport on coral reefs remain poorly understood. The aim of this study was to investigate hydrodynamic drivers of suspended-sediment concentrations and fluxes throughout a fringing reef-lagoon system in order to determine how suspended sediment transport pathways vary in response to variability in local benthic habitat characteristics and hydrodynamic conditions (waves and currents) throughout a reef. A 3 week field experiment (27 July – Aug 14 2013) was conducted in the northern region of Ningaloo Reef (Western Australia), focusing on an ~4 km section of reef near Tantabiddi. This section of reef was specifically chosen as it contained a mix of coral, algal, and other reef communities that were deemed more similar to reef systems in northwestern Australia (including in the Pilbara) rather than the near 100% coral coverage characteristic of many parts of southern Ningaloo Reef. The field sampling consisted of 12 sites where we deployed an acoustic wave and current meter (AWAC) that measured wave conditions on the fore reef, 2 acoustic Doppler current profilers (ADCPs) measuring the water-column current profiles in the channels, 5 acoustic Doppler profilers (ADPs) that measured the current profiles on the reef and within the lagoon, and 5 wave gauges distributed across the reef. In addition, most sites had co-located optical backscatter sensors (OBSs) that were deployed to infer suspended-sediment concentrations (7 in total). The results revealed that suspended sediment concentrations on the reef flat and in the lagoon remained low throughout the experiment despite the variation in incident offshore wave conditions. In contrast, the suspended sediment concentrations in the channels were substantially larger and varied with the incident reef conditions. A detailed assessment of the hydrodynamic processes that drove transport indicated that on the reef flat, sea-swell waves combined with currents was the main contributor to the nearbed velocity skewness that contributed to cross-shore sediment transport. However, as the water level on the reef flat decreased, longer infragravity waves as well as the mean current become relatively more important. Thus, sea-swell waves, infragravity waves and currents may all contribute to sediment transport processes on the reef flat. In the lagoon, the sediment transport was overwhelmingly driven the mean currents. Suspended sediment variability on the reef flat was smaller than in the lagoon or channels. However, throughout the system a majority of the SSC variability could be explained by variations over sub-tidal timescales with less variance in the concentration occurring at intra-tidal timescales.

3.1 Introduction

Coral reefs modify the spatial and temporal variability of hydrodynamic processes along many of the world's tropical coastlines. Such processes (i.e., waves and currents) can play an important role in controlling rates and pathways of sediment transport, which can strongly influence adjacent coastal morphology and cause shoreline changes.

In reef environments, the rapid transition in depth from relatively deep to shallow water on the forereef transforms and attenuates incident waves, predominantly by wave breaking but also due to bottom friction (e.g., Monismith, 2007b). Incident waves that do not break on the forereef are limited by the reef flat water depth

³ Published as Pomeroy, A., Lowe, R., Ghisalberti, M., Storlazzi, C., (2018) Spatial variability of sediment transport processes over intra- and subtidal timescales within a fringing coral reef system, *Journal of Geophysical Research – Earth Surface*, accepted, <https://doi.org/10.1002/2017JF004468>.

(e.g., Gourlay, 1994b; Hardy and Young, 1996b). As these waves propagate across the reef flat and into the lagoon, they are attenuated by drag imposed by large bottom roughness (e.g., Lowe et al., 2005c) as well as by nonlinear wave-wave interactions (e.g., Sheremet et al., 2011; Péquignet et al., 2014). Ultimately the wave spectrum becomes bi-modal across many reefs (Hardy and Young, 1996b) and is usually characterised by depth limited short sea-swell waves with periods 5-25 s and longer free infragravity waves (periods 25-250 s) that propagate across the reef (e.g., Lugo-Fernández et al., 1998b; Pomeroy et al., 2012d; Harris et al., 2015).

Spatial gradients in radiation stress that result from incident wave breaking on the forereef (Longuet-Higgins and Stewart, 1964b) are balanced by cross-shore pressure gradients that induce wave setup and mean bottom stresses associated with cross-reef currents (e.g., Gourlay, 1996b, 1996d; Massel and Gourlay, 2000; Jago et al., 2007). For a one-dimensional reef without a lagoon, the relative magnitude of the wave-driven currents depend on radiation stress forcing and are modulated by the incident wave variability, changes in the water depth due to the tide, the bottom roughness, and the reef flat width (e.g., Symonds et al., 1995; Hearn, 1999; Gourlay and Colleter, 2005). For fringing reefs, these cross-reef currents enter a bounded lagoon where a spatial variations in the lagoon sea-level (that decreases towards any channels / gaps in the reef (Lowe et al., 2009b, 2009d)) establishes an alongshore pressure gradient that drives currents that return to the surrounding ocean (e.g., Coronado et al., 2007; Taebi et al., 2011).

Sediment motion is initiated when bed shear stresses τ imposed by currents and waves on sediment particles exceed a critical threshold that predominantly depends on the grain size and sediment density (Shields, 1936). If the bed is bare (i.e. lacking large immobile roughness associated with reef communities), the stresses imposed on the sediment can be directly estimated from the incident currents and waves (e.g., see Nielsen, 1992). However, in the presence of large immobile roughness (often referred to as canopies) these stresses can be substantially less due to attenuation of the current and waves by the roughness (e.g., Pomeroy et al., submitted; Le Bouteiller and Venditti, 2015; Stocking et al., 2016). Once sediment motion has been initiated, the sediment is initially transported as bedload, which may include the migration of bed forms (e.g., ripples) (e.g., Van Rijn, 1984a; Traykovski et al., 1999). When the vertical component of turbulent eddies generated near the bed are sufficiently large to overcome the particle fall velocity (w_s), sediment can be lifted into suspension (e.g., Bagnold, 1966; Francis, 1973; Van Rijn, 1984b). If ripples are present, organized vortex shedding can also suspend sediment from the bed (e.g., Thorne et al., 2003; O'Hara Murray et al., 2012). Sediment in suspension is transported by mean currents or by nonlinear waves until it can no longer be supported by the upward vertical component of the turbulent eddies or vortices; this sediment then settles out of the water column and is deposited on the bed. Thus, the magnitude and duration, as well as the frequency, of sediment transport are directly related to the spatial and temporal variability of the hydrodynamic processes and the roughness properties of the seabed.

We hypothesize that the variable hydrodynamic forcing in fringing coral reef environments will result in distinct patterns in sediment suspension and affect the rates and direction of suspended sediment transport. The objectives of this study were thus to: (1) assess the variability of sea-swell waves, infragravity waves and mean currents at different locations and timescales in a fringing reef; (2) quantify the magnitude as well as the spatial and temporal variability of suspended sediment concentrations; and (3) evaluate how the suspended sediment concentrations that were observed relate to the prevailing hydrodynamic processes.

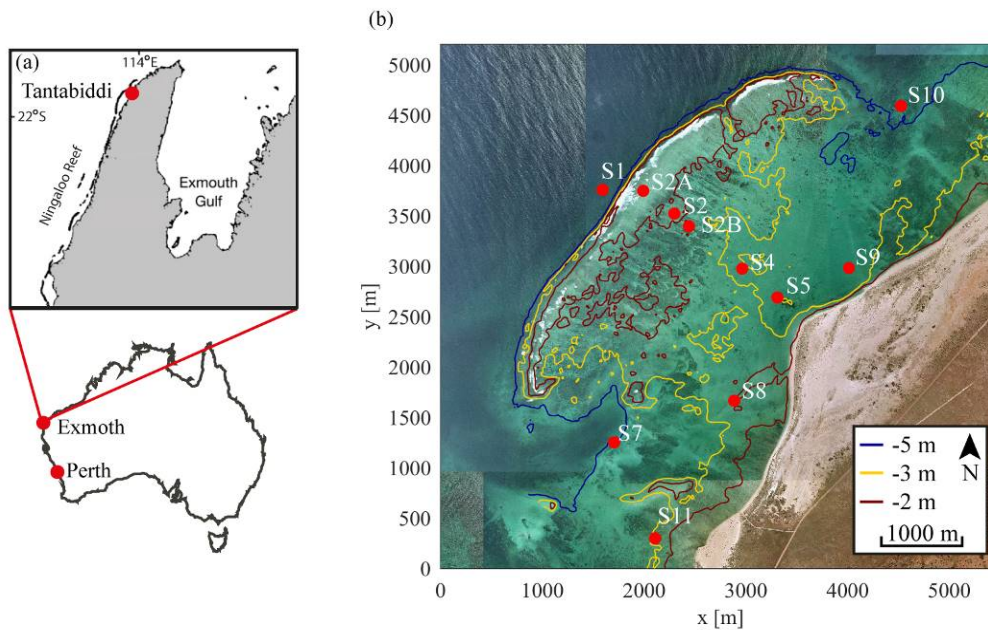


Figure 3.1. (a) The field study site at Tantabiddi within Ningaloo Reef in north-western Australia. (b) An aerial view of the site (origin: 21.89699°S, 113.96212°E) with the locations of the instruments relevant to this study and key bathymetric contours indicated.

3.2 Methods

Site description

The field study focused on an ~5 km section of reef near Tantabiddi (21°52'6.03"S, 113°58'58.26"E, Figure 3.1) in Ningaloo Reef, Western Australia that (1) was exposed to temporally variable incident forcing; (2) had a spatially variable reef structure (reef flat with clearly define breaks and a sandy lagoon); and (3) exhibited roughness that was representative of many reef environments worldwide. This section of reef had a cross-shore orientation of ~130° (defined as clockwise from true north) and is bounded to the north and south by shore-normal channels that cut into the reef crest and outer reef flat. Due to the presence of the large salient at the shoreline in the lee of the reef, the location of the reef crest relative to the shoreline varies from 2.0-2.5 km. The reef flat is ~0.6-1.5 m below mean sea level and is ~500 m in width. The lagoon is generally ~3 m deep with channels that are up to ~6 m deep. In contrast to many parts of southern Ningaloo Reef that typically have near 100% coral coverage, this site is characterised by a mix of macro-algae, coralline algae, sand, and some live coral (Cuttler et al., 2015), which makes it typical of many tropical reef systems worldwide.

Table 3.1. Instrument site information and sampling configuration#

	Site and Depth	Instrument	Sampling Information
S1	(forereef ~10.5 m)	Nortek AWAC	1 Hz with 2048 s burst every 3600 s; current profile every 5 min, 0.5 m cells; velocity sample height: 1.04 m
		RBR Virtuoso D	Continuous sampling at 1 Hz; pressure sample height: 0.2 m
SSA	(reef flat ~1.3 m)	RBR TWR-2050	4096 samples at 2 Hz every 3600 ; pressure sample height: 0.1 m
S2	(reef flat ~1.5 m)	Nortek ADP-HR	Continuous 1 Hz current profile, 25 mm cells, velocity sample height: 0.22 m; pressure sample height: 0.07 m
		Wetlabs FLNTU	0.29 Hz with 462 samples every 3600 s; sample heights: 0.37, 0.64, 0.90 m
		Suction samples	Hourly during daylight; SSC sample heights: 0.23, 0.27, 0.34, 0.51, 0.76, 1.02 m.
S2B	(reef flat ~2.1 m)	RBR Virtuoso D	Continuous sampling at 1 Hz; pressure sample height: 0.05 m
S4	(lagoon ~ 2.7 m)	RBR Virtuoso D	turbidity samples continuously every 15 s, height 0.28 m
		Wetlabs FLNTU	0.29 Hz with 462 samples every 3600 s; sample heights: 0.37, 0.64, 0.90 m
S5	(salient ~ 3.5 m)	Nortek ADP	Continuous 1 Hz current profile, 10 cm cells, velocity sample height: 0.40 m; pressure sample height: 0.14 m
		Aquatec 210-TY	turbidity samples continuously every 10 s, height 0.55 m
S7	(south channel ~ 5.4 m)	RDI ADCP	Continuous 1 Hz current profile, 30 cm cells, velocity sample height: 1.07 m; pressure sample height: 0.33 m
		Aquatec 210-TY	turbidity samples continuously every 10 s, height 0.67 m
S8	(south salient ~ 2.3 m)	Nortek ADP	current profile averaged over 180 s every 300 s, 10 cm cells, velocity sample height: 0.40 m; 2048 pressure samples at 2 Hz every 3600 s, height: 0.2 m
S9	(north salient ~ 3.6 m)	Nortek ADP	current profile averaged over 180 s every 300 s, 10 cm cells, velocity sample height: 0.40 m; 2048 pressure samples at 2 Hz every 3600 s, height: 0.2 m
S10	(north channel ~7.4 m)	RDI ADCP	Continuous 1 Hz pressure sample height: 0.75 m. Velocity measurements were not obtained due to an instrument fault.
		Aquatec 210-TY	turbidity samples continuously every 10 s, height 0.77 m
S11	(south channel ~2.3 m)	RBR T-Duo	2048 samples at 1 Hz every 3600 s; pressure sample height: 0.05 m

elevation are relative to the sea bed

Field study

A 3-week field experiment was conducted that consisted of two main components: (1) a detailed study of the hydrodynamics and sediment transport on the reef flat (Section 2), and (2) a broader-scale hydrodynamic and sediment transport study throughout the reef and lagoon. The results presented in this paper focus on the second component and are based on a large instrument array that quantified hydrodynamic processes and sediment concentrations spatially throughout the study site (Pomeroy, 2016). Detailed sampling information for

each instrument is included in Table 3.1 and a summary follows.

The instrument array (Figure 3.1b) was deployed for a period of 19 days during the austral winter of 2013 (27 July to 14 August). Incident wave conditions were measured on the forereef at S1 with a 1 MHz Nortek AWAC directional wave gauge/current profiler. A cross-shore transect from near the reef crest to the tip of the shoreline salient measured the properties of waves that propagated toward the shoreline. In addition to the wave measurements, current profiles were measured by upward facing acoustic Doppler profilers (ADP) towards the back of the reef flat (S2) as well as near the shoreline at the tip of the salient (S5). To evaluate the spatial variability in the hydrodynamics due to the reef structure, Acoustic Doppler Current Profilers (ADCP) were deployed in the southern and northern reef breaks (S7 and S10). We note that due to an instrument failure, only waves from the pressure sensor were derived at S10. Close to the shoreline, ADPs measured current profiles and waves on either side of the salient (S8 and S9), and a wave gauge measured the wave conditions near the shoreline adjacent to the southern break in the reef (S11). The wave gauge at S3 failed and site S6 is located south of the study area and thus both have been excluded from this study. The wind was measured at the Milyerling weather station, approximately 20 km north of the site (Australian Institute of Marine Science, 2013).

Temporal variability in suspended sediment concentrations (SSC) was measured on the reef flat (S2), in the lagoon (S4), near the salient (S5) and in the channels (S7 and S10) with optical backscatter sensors (OBSs) (Table 3.1). On the reef flat, these instruments were calibrated with direct *in situ* suction samples that were obtained via a 5 mm diameter intake that was oriented perpendicular to the dominant mean flow direction and pumped to a scaffold platform nearby (Section 2). Based on the intake diameter and volume flow rate, the intake flow velocity was approximately 0.6 m s^{-1} , or 2-3 times greater than measured root-mean-squared (RMS) velocities (see below); therefore, errors due to inefficiencies or bias in particle capture are expected to be small (Bosman et al., 1987). The remaining OBSs were calibrated with *in situ* samples obtained with Niskin bottles during the field experiment.

In addition to the fixed instrument array, Lagrangian drifters (9-10), similar in design to those described by Schmidt et al. (2005), were deployed under various conditions to spatially measure transport pathways and velocities. The position of each drifter was recorded at 0.3 Hz by internal Garmin GPS devices (eTrex 10). The drifters were deployed from a boat in pre-defined arrangements to distinguish regions of different flow intensities and were permitted to drift until they exited a predefined area, became stranded on the beach or drifted past predefined boundaries offshore from the channel. Ten drifter deployments (~2-4 hrs each) were conducted under various wave, wind, and tidal conditions. A subset of these measurements are considered in this study.

Data analysis

Hydrodynamic data

Offshore wave conditions (wave height, period and direction) were measured on the forereef (S1) directly by the AWAC acoustic surface tracking, whereas wave conditions on the reef flat and in the lagoon were determined from the pressure time-series using linear wave theory. Directional wave spectra were computed on the forereef as well at the sites where ADPs were deployed using the Maximum Likelihood Method (Emery and Thomson, 2001). One-dimensional surface elevation spectra were derived from pressure time-series at the other locations. From the spectra, the zeroth-moment (significant) wave heights for the shorter-period (5-25 s) sea-swell waves ($H_{m0,sw}$) and longer period (25-250 s) infragravity waves ($H_{m0,ig}$) were calculated, as well as both the peak period (T_p) and the weighted-mean sea-swell wave direction (θ) where co-located velocity measurements were available.

Suspended sediment concentrations

Suspended sediment concentrations on the reef flat were determined from suction samples obtained at hourly intervals during daylight hours (see Section 2 for details). The water samples were collected with peristaltic pumps via intake ports located perpendicular to the dominant cross-reef flow direction (Bosman et al., 1987) and stored in 2 L bottles. In the lagoon, concentration samples were obtained with 2.5 L Niskin Bottle samples

adjacent to the OBS instruments. The samples were vacuum filtered onto pre-weighed membrane filters (Whatman ME27, 0.8 μm), dried (75°C for 24 hrs) and weighed in order to calculate SSCs. The known SSCs along with resuspended bed samples obtained at each instrument were then related to the backscatter measured by the instruments via linear regression. We note that for the ADP, this backscatter was corrected for acoustic decay (e.g., Ha et al., 2011) prior to the regression analysis.

The SSC variability at short time scales (< 1 hr) was quantified by calculating the 1st and 3rd concentration quartiles from the hourly bursts of data. To evaluate the SSC variability over longer timescales, the means of shorter bursts of data (15 min) were calculated to form a decimated time-series that was then analysed with the Singular-Spectrum Analysis technique (e.g., Vautard et al., 1992; Schoellhamer, 2002). This technique identifies a set of uncorrelated time-dependent variables that describe different fractions of the original signal variance. An advantage of this analysis technique in comparison to other techniques (such as Empirical Orthogonal Analysis) for suspended sediment concentration analysis is that this technique enables trends as well as periodic or quasi-periodic components to be identified that may also be amplitude modulated. In our analysis we use a window period of $M=36$ h, which enabled the decomposed SSC to be compared with the hydrodynamic data and periodicities within the range of ~ 7 -36 hours to be identified (e.g., Vautard et al., 1992).

Table 3.2. Calibration parameters used for the linear conversion of the ADP and OBS backscatter data (B_k) to suspended sediment concentrations (SSC).

Site (instrument)	Calibration Equation (mg/L)	R ²	n
S2 (ADP)	$SSC = 0.052 B_k - 2.68$	0.61	35
S5 (OBS)	$SSC = 21.34 B_k - 2.22$	0.99	12
S7 (OBS)	$SSC = 4.78 B_k + 0.59$	0.99	9
S10 (OBS)	$SSC = 11.67 B_k - 3.21$	0.99	12

Note: calibration for the OBS instruments was conducted between the measured concentration and the instrument's recorded FTU.

Shear stresses imposed on sediment grains

Close to the seabed, the resistance (τ_{total}) experienced by waves and currents is often partitioned into two components: (1) a bed stress component (τ_{bed}) that is due to the stress imposed by sediment grains at the bed; and (2) a form drag component (τ_{drag}) that is due to bed roughness that may be mobile (e.g., sand ripples (e.g., Van Rijn, 2007)) or immobile (e.g., coral structures or aquatic vegetation (e.g., Le Bouteiller and Venditti, 2015)):

$$\tau_{total} = \tau_{bed} + \tau_{drag} \quad (2.1)$$

In the presence of relatively small roughness (e.g., sand grains), τ_{drag} is small and $\tau_{total} \approx \tau_{bed}$; the shear stress exerted on hydrodynamic processes by the bed roughness is equally relevant to the assessment of sediment transport and can be reasonably estimated from hydrodynamic measurements higher in the water column. However, when the bed roughness is large, τ_{drag} can be substantially greater than τ_{bed} and the shear stress estimated from hydrodynamic measurements obtained above the roughness is larger than the stress exerted on the sediment (see Section 2). Thus, the suspension and transport of sediment by waves and currents is reduced when compared to the same processes over a bare sediment bed.

At each of the sites where OBS measurements were obtained, the shear velocity ($u_* = \sqrt{\tau/\rho_w}$), based on seawater density (ρ_w), imposed on sediment at the bed was estimated. The wave-current boundary layer theory of Grant and Madsen (1979) was used to calculate u_* as it accounts for the enhancement of the bed shear velocity due to the nonlinear superposition of both waves (u_{*w}) and mean currents (u_{*c}). The mean of the enhanced shear velocity (u_{*m}) is larger than pure current shear velocity, and the maximum of the enhanced shear velocity (u_{*max}) is larger than the vector summation of u_{*c} and u_{*w} (e.g., Soulsby and Clarke, 2005). The Grant and

Madsen (1979) approach was generalized for spectral conditions by Madsen et al. (1988) and Madsen (1994), where representative parameters are used that place more weight on the frequency components that contain more wave energy. To understand the relative importance of sea-swell and low-frequency waves to the shear stress imposed on the bed, we also calculated shear velocity for both sea-swell u_{*sw} and low-frequency u_{*ig} waves in the presence of a current.

The direction of the waves and currents were computed separately so that the angle between the waves and currents could be considered in the calculation of u_* . For each hourly burst of data, the mean current (\bar{u}) speed and direction were computed. The mean current vector was then removed from each velocity record and the (residual) oscillatory velocity data rotated into a coordinate system that maximized the velocity variance along the primary axis. In this coordinate system, the wave (\tilde{u}) velocities were determined.

For each frequency band, a representative maximum near-bed horizontal orbital velocity $\tilde{u}_{b,r}$ was calculated (Madsen et al., 1988; Madsen, 1994):

$$\tilde{u}_{b,r} = \sqrt{\sum_{n=1}^N \tilde{u}_{b,n}^2} \quad (2.2)$$

where $\tilde{u}_{b,n}$ is the horizontal orbital velocity measurement of the n th component. On the reef flat (S2), where large bottom roughness affects the waves and currents close to the bed, the velocity measurement obtained within the roughness was used (consistent with Section 2). In the lagoon (where there was an absence of large roughness near the measurement locations), the velocity measured closest to the bed was used at S5 and S7, while at S10 $\tilde{u}_{b,n}$ was calculated from the pressure data using linear wave theory due to the absence of high-frequency velocity measurements:

$$\tilde{u}_{b,n} = \frac{a_n \omega_n}{\sinh k_n h} \quad (2.3)$$

where ω_n is the radian frequency and a_n is the n th component of the wave amplitude as determined by $a_n = \sqrt{2S_n df}$. The representative wave radian frequency was defined as:

$$\omega_r = \frac{\sum_{n=1}^N \omega_n \tilde{u}_{b,n}^2}{\sum_{n=1}^N \tilde{u}_{b,n}^2} \quad (2.4)$$

To determine the representative wave friction factor f_{wc} , we followed Madsen (1994) and assumed that the monochromatic friction formulae (such as that proposed by Swart (1974)) can be extended to spectrally distributed waves by applying such formulae to each frequency component. In this study, we used the revised friction formulae proposed by Madsen (1994) to calculate f_{wc} for the representative periodic wave defined by sea-swell and infragravity frequencies. Implicit in this assumption is that the representative hydraulic roughness length k_r is constant, which was found to be valid in laboratory experiments by Mathisen and Madsen (1999) and reasonable in a field observations over a coral reef flat by Lowe et al (2005c).

In Section 2, it was demonstrated that the stresses imposed by large immobile roughness on the waves and currents above the roughness are unrelated to the suspension and transport of sediment on the reef flat at S2. Rather, the size of the sediment grains within the roughness was more relevant. To evaluate the spatial differences in the shear stresses imposed on sediment grains, we defined k_r using the Nikuradse roughness ($k_r = k_N = 2.5D_{50}$) with a constant median grain size ($D_{50} = 240 \mu\text{m}$) so that the spatial variability in u_* is only due to differences in hydrodynamics at different locations. On the reef flat, the D_{50} used in this analysis was similar to that measured on the bed between the large immobile roughness, while in the lagoon the sediment on the bed was typically finer.

Relative importance of waves and currents

As simple first approximation to evaluate the importance of mean currents, sea-swell waves and infragravity waves to the transport of sediment, we assumed that the transport of sediment responds in a quasi-steady manner to the time-varying flow induced by waves as they propagate over the reef towards the shore. In this context, the third velocity moment (u^3) was decomposed (see also Section 2) on the reef flat (at S2) and in the lagoon near the salient (at S5). This velocity moment quantifies the nonlinearity of the near-bed velocity, which contributes the transport sediment either onshore or offshore (e.g., Bailard, 1981; Guza and Thornton, 1985; Roelvink and Stive, 1989). To evaluate the contributions of mean currents, sea-swell waves and infragravity waves to this moment, the velocity (u) measured in the three cells closest to the bed was bandpass filtered to obtain mean (\bar{u}), sea-swell (\tilde{u}_{sw} , 0.04-0.2Hz) and infragravity (\tilde{u}_{ig} , 0.004-0.04Hz) wave contribution to the velocity. The velocity signals were then substituted into u^3 and expanded to produced 10 terms that are described in Table 3.1. These terms are often used to describe different sediment transport processes (in a wave-averaged sense) whereby each terms consists of a component that can be associated with an 'entrainment' process ($\tau \propto u^2$) and an advection process (u) (e.g., Roelvink and Stive, 1989; Marino-Tapia et al., 2007; see also Section 2). We note that each of these decomposed terms cannot be directly compared as they do not account for the frequency dependent nature of bed shear stress or the complex processes within the near-bed boundary layer; rather they indicate the physical processes that may contribute to the transport of sediment. Each term was normalized by the velocity variance, which enabled the data to be compared across the experiment duration.

Table 3.1. Third order moment decomposition of the velocity (u). The dominant terms are later found to be those highlighted by the *.

Term	Composition	Description
M1*	\bar{u}^3	mean velocity cubed
M2	$\langle \tilde{u}_{sw}^2 \tilde{u}_{sw} \rangle$	skewness of sea-swell waves
M3*	$3\langle \tilde{u}_{sw}^2 \tilde{u}_{ig} \rangle$	correlation of sea-swell wave variance and infragravity wave velocity
M4	$3\langle \tilde{u}_{ig}^2 \tilde{u}_{sw} \rangle$	correlation of infragravity variance and sea-swell wave velocity
M5	$\langle \tilde{u}_{ig}^2 \tilde{u}_{ig} \rangle$	skewness of infragravity waves
M6*	$3\langle \tilde{u}_{sw}^2 \rangle \bar{u}$	entrainment by sea-swell waves and transport by mean flow
M7*	$3\langle \tilde{u}_{ig}^2 \rangle \bar{u}$	entrainment by infragravity waves and transport by mean flow
M8	$6\langle \tilde{u}_{sw} \tilde{u}_{ig} \rangle \bar{u}$	six way correlation
M9	$3\langle \tilde{u}_{sw} \rangle \bar{u}^2$	time-average of sea-swell wave oscillatory component
M10	$3\langle \tilde{u}_{ig} \rangle \bar{u}^2$	time-average of infragravity wave oscillatory component

3.3 Results

Forcing conditions

During the first part of the experiment (1-5 August 2013), the offshore wave heights ($H_{m0,sw}$) measured on the forereef at S1 were small and relatively consistent (~ 0.7 - 1.2 m, Figure 3.2a). Two larger swell events (6-8 August 2013 and 9-11 August 2013) occurred during the latter part of the experiment, with maximum wave heights reaching ~ 2.5 m in both events. T_p ranged from 12 s during lower wave conditions to up to 19 s during the larger swell events (Figure 3.2b). The $H_{m0,sw}$ measured throughout the experiment originated from $\sim 280^\circ$ ($\sim 30^\circ$ from the cross-reef direction which is 309° , Figure 3.2c) with very little variation in θ observed when the swell events occurred ($< 10^\circ$). The water depth (Figure 3.2d) varied over the duration of the experiment and ranged from ~ 0.6 - 1.2 m near spring tide. The wind (Figure 3.2e,f) predominantly consisted of two states: (1) offshore wind and (2) an approximately alongshore wind. Periods with offshore-directed winds persisted for a large proportion of the experiment with speeds of 2 - 8 m s^{-1} . Later in the experiment, distinct periods of alongshore winds with speeds of 4 - 5 m s^{-1} were measured. Overall, the wind tended to be greater at the start and end of the experiment and did not increase with the first swell; however, the wind increased with the arrival of the second swell event.

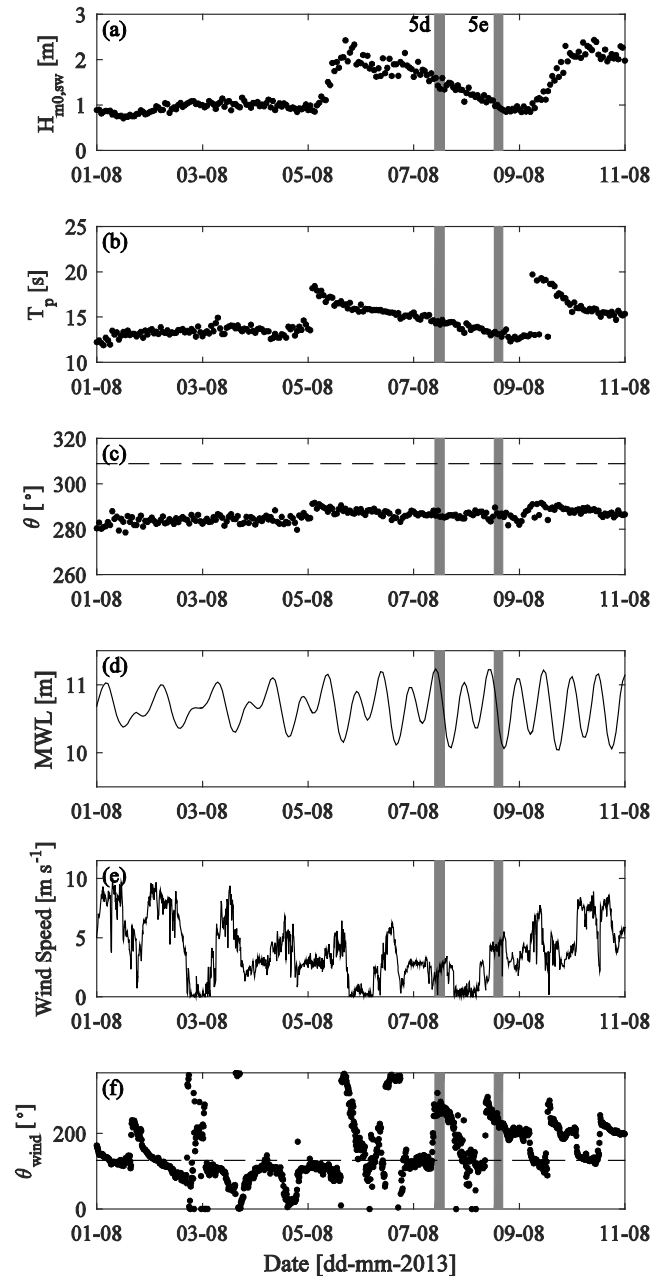


Figure 3.2. The offshore (a) swell wave height $H_{m0,sw}$, (b) peak wave period T_p , (c) peak incident wave direction θ , and (d) water depth measured on the forereef at S1. The horizontal dashed line in (c) denotes the cross-reef direction. (e) The 10 min mean wind speed and (f) the direction θ_{wind} measured at Milyering weather station. The horizontal dashed line in (f) indicates the offshore wind direction. The shaded bars refer to drifter deployments in Figure 3.5

Waves and currents

Sea-swell waves

The height of the sea-swell waves ($H_{m0,sw}$) was rapidly dissipated near the reef crest, which resulted in a fairly consistent wave climate on the reef and in the lagoon (Figure 3.3a). The $H_{m0,sw}$ measured on the reef flat were depth limited, correlated with the reef flat water depth ($R=0.99$) and were only $\sim 25\%$ of the $H_{m0,sw}$ measured on the forereef at S1. The waves on the reef flat consistently propagated from $\sim 280^\circ$. In contrast, the waves that entered through the channels were approximately twice as large as those measured on the reef flat and were linearly correlated ($R=0.97-0.99$) to the offshore forereef $H_{m0,sw}$; the waves did not exhibit as much tidal modulation as observed on the reef flat (Figure 3.3c). While the $H_{m0,sw}$ measured in the center of the lagoon

(S4) was smaller than on the reef flat and in the channels ($\sim 14\%$ of the $H_{m0,sw}$ measured at S1), closer to the shoreline the $H_{m0,sw}$ slightly increased again due to refraction of the waves that originated from the channels toward the salient (e.g., at S8, Figure 3.3c). This refraction resulted in some wave direction variability at the tip of the salient but on either side of the salient the wave direction was almost perpendicular to the shoreline. While the $H_{m0,sw}$ along the shoreline was similar throughout the study site ($\sim 20\%$ of the $H_{m0,sw}$ at S1), directly behind the reef the $H_{m0,sw}$ were correlated with the reef flat water depth ($R=0.80-0.92$) while opposite the break in the reef (S11) the waves were correlated ($R=0.98$) with the forereef $H_{m0,sw}$.

Infragravity waves

The height of the infragravity waves ($H_{m0,ig}$) were largest on the reef flat near the reef crest (S2A, Figure 3.3b) and, in contrast to the $H_{m0,sw}$, were not strongly modulated by the tidal elevation but instead were correlated ($R=0.95$) with offshore $H_{m0,sw}$ (Figure 3.3d). As a consequence, the $H_{m0,sw}$ on the reef flat were larger than the $H_{m0,ig}$ during high tide, but were similar or smaller in height at low tide as well as during the larger swell events. The $H_{m0,ig}$ in the channels were also correlated ($R=0.88-0.97$) with the $H_{m0,sw}$ at S1 but were smaller than the $H_{m0,ig}$ measured on the reef flat (typically $\sim 60-70\%$ of the $H_{m0,ig}$ measured at S2A, Figure 3.3b). The $H_{m0,ig}$ decreased as the waves propagated through the lagoon towards the shoreline where the waves were $\sim 50-70\%$ of the height measured at S2A.

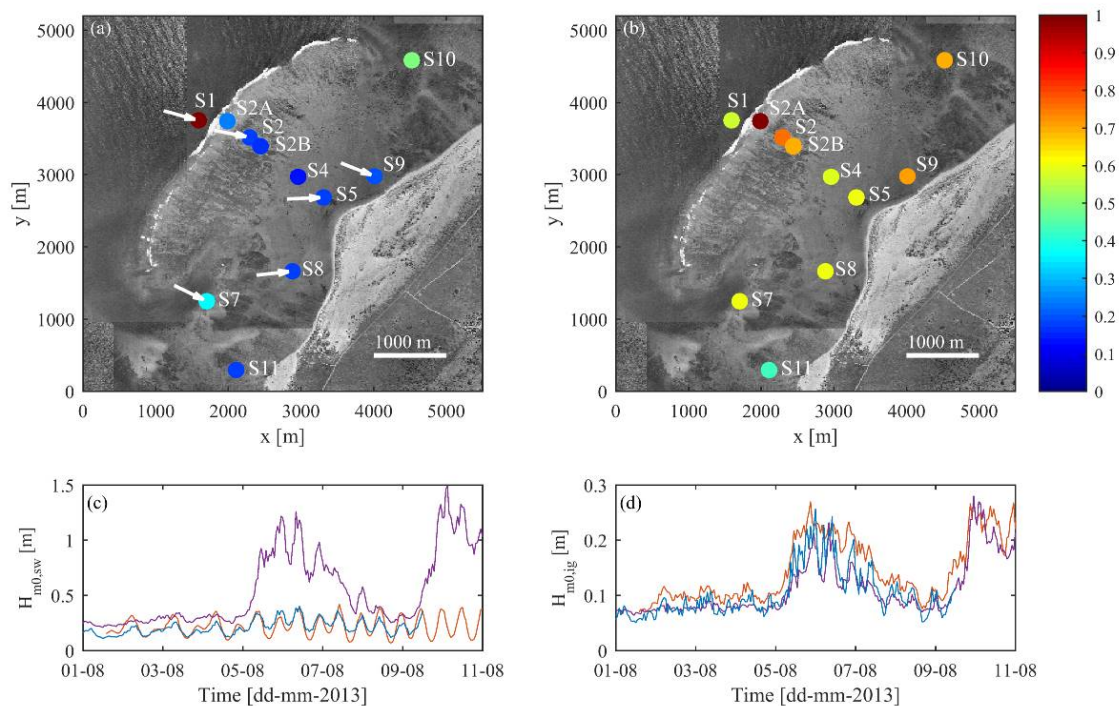


Figure 3.3. The (a) swell wave height $H_{m0,sw}$ normalized by $H_{m0,sw}$ at S1 with the mean wave direction indicated by the white arrows (b) infragravity wave height $H_{m0,ig}$ at different measurement locations normalized $H_{m0,ig}$ at S2A. Timeseries of the (c) $H_{m0,sw}$ and (d) $H_{m0,ig}$ on the reef flat at S2 (red), in the lagoon at S8 (blue) and in the channel at S7 (purple). The normalized wave height is indicated by the colorbar (no units).

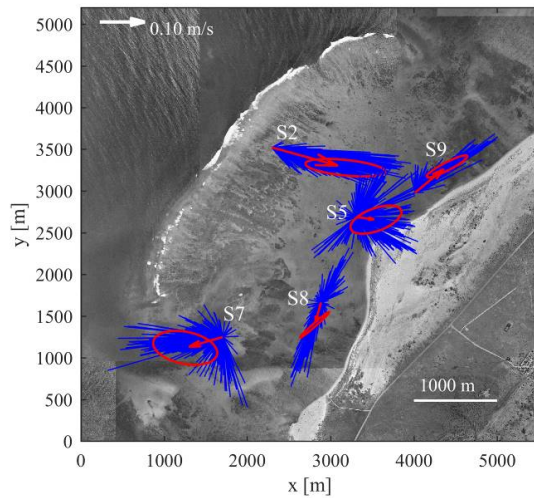


Figure 3.4. Hourly mean depth-averaged current data (blue) with the experiment-averaged mean current vector indicated by the arrows. The ellipses (red) indicate the direction of the major and minor semi-axes of variability. The scale of the ellipse represents one standard deviation along each semi-axis.

Mean currents

The mean currents on the reef flat (S2) were consistently cross-shore directed throughout the duration of the experiment (

Figure 3.4). In contrast, the mean currents varied considerably in magnitude and direction near the salient (S5), while on either side of the salient at S8 and S9 the mean flow remained smaller than at S2 and was oriented mostly parallel to the shoreline. Less directional variability was observed at S9 than at S8. In the southern channel (S7), the mean flow was offshore through the channel but at shorter timescales could be directed either offshore or onshore.

The sub-tidal (low pass filtered) component of the flow revealed two flow patterns. The first flow pathway was directed across the reef flat towards the salient where it diverged near the salient and returned to the ocean via the two channels (Figure 3.5a); thus similar to the experiment-averaged current vectors in

Figure 3.4 as well as the path of the Lagrangian drifters shown in Figure 3.5d. This mode accounted for ~95% of the current variability (Figure 3.5a, Mode 1). The amplitude time series indicated that this pathway was prevalent throughout most of the experiment and was intensified during the swell events (Figure 3.5b). The amplitude time series also had a strong correlation ($R=0.97$) to the forereef $H_{m0,sw}$, which was maximum at zero phase lag (Figure 3.5c).

The second flow pathway identified by the sub-tidal analysis (Mode 2, Figure 3.5a) was consistently directed northward along the shoreline. However, for much of the experiment this mode was insignificant except at both the start and end of the experiment (Figure 3.5b). For this mode to dominate the flow variability, the forereef waves needed to be small (so that the cross-reef flow was also reduced) and the alongshore wind relatively strong. Early in the experiment (prior to 02 Aug) these conditions were satisfied (Figure 3.5c), although we note that there was a lag in the response of the lagoon flow and the alongshore wind. Later in the experiment (08-09 Aug) the response is clearer and the maximum correlation indicated that the alongshore wind and lagoon flow were in-phase (Figure 3.5c). It was during these conditions that the drifters also measured a northward flow (Figure 3.5e). We note that the wind was directed in a similar direction to flow mode 1 with approximately the same magnitude; but only the offshore wave height differed.

The intra-tidal current variability could also be mostly described by two flow patterns. The first flow pattern,

which accounted for $\sim 54\%$ of the intra-tidal current variability, was directed through the channel and northward within the lagoon (Mode 1, Figure 3.6a). Very little cross reef flow, where the water depth is shallower and friction larger, was associated with this flow pattern. The amplitude of this mode (Figure 3.6b) was predominantly associated with the semi-diurnal tidal constituent ($R=0.80$) and led the tidal surface elevation (Figure 3.6c) by 3 hrs. The second flow pathway (Mode 2, Figure 3.6a) was across the reef flat, along the shoreline and through the channels. The amplitude of this mode was 180° out-of-phase with the tidal surface elevation (Figure 3.6c, $R=0.71$). The magnitude of the flow was highest at low water depths and decreased as the water depth on the reef flat increased, which is consistent with flow induced by wave-breaking on the reef.

Thus, while currents measured on the reef and in the lagoon are modulated at intra-tidal timescales, it is evident that the mass transport pathways are predominantly due to wave-driven currents generated by the incident wave conditions at sub-tidal timescales. However, as the waves decrease in magnitude, the relative importance of wind stress increases and the circulation occasionally become wind driven.

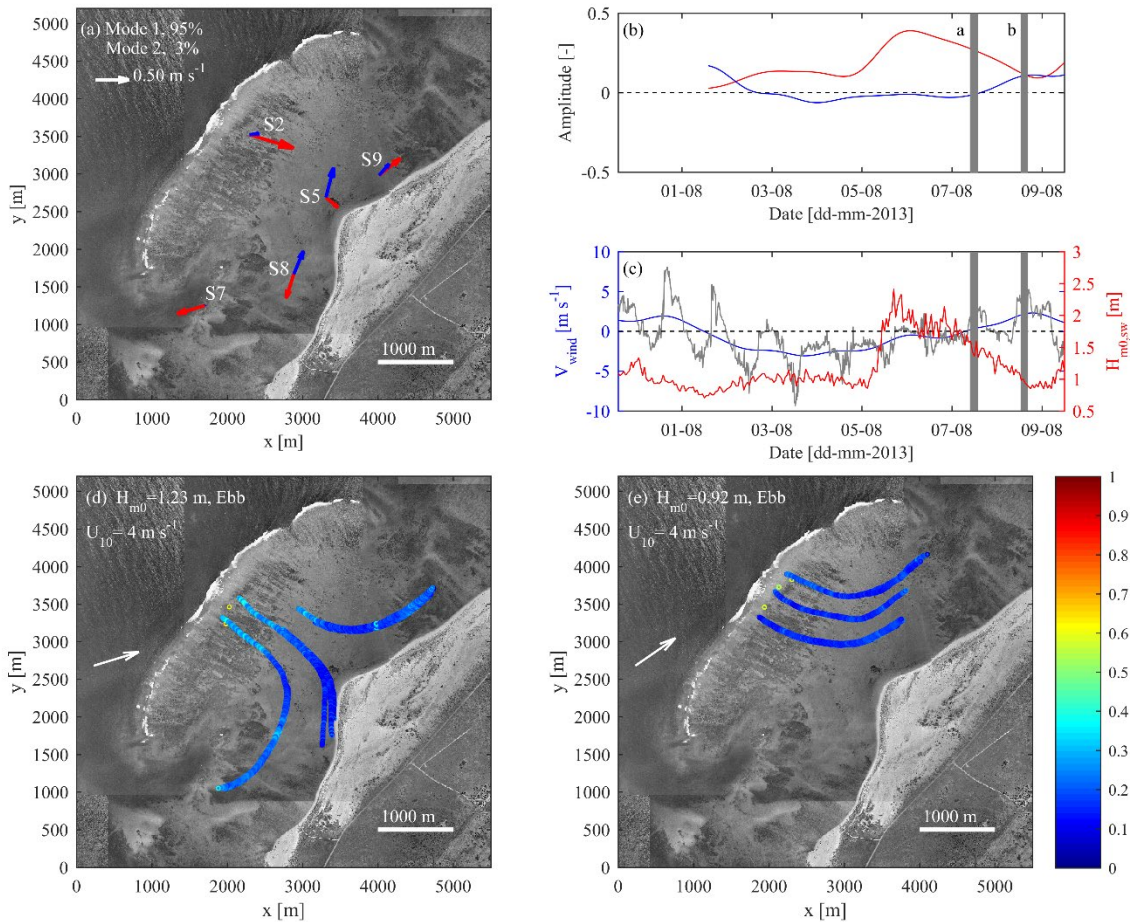


Figure 3.5. (a) The first (red) and second (blue) 36 hr empirical mode of sub-tidal current variability along with (b) the amplitude of the respective modal amplitude time-series from the EOF analysis. To facilitate comparison of the two modes, the amplitude of the arrows and amplitude time-series have been scaled to that the arrows are equal in magnitude at S8 (c) The alongshore wind speed V_{wind} and (grey) averaged over 10 min and (blue) at sub-tidal temporal scales. (red) The forereef sea-swell wave height ($H_{m0,sw}$). The grey shading indicates the drifter experiments shown in (d) and (e). (d-e) Surface current Lagrangian drifter trajectories measured for different forcing and tidal states (indicated in Figure 3.2). The white arrow denotes the wind magnitude and direction. The velocity of the drifters is indicated by the colour of the drifter track and described by the colourbar (in m s^{-1}).

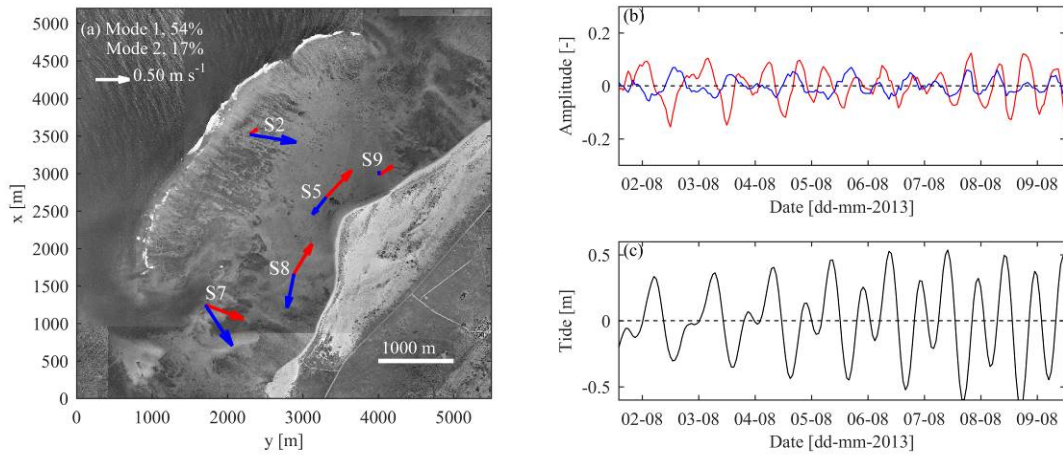


Figure 3.6. (a) The first (red) and second (blue) empirical model intra-tidal current variability along with (b) the respective modal amplitude time-series. To facilitate comparison of the two modes, the amplitude of the arrows and amplitude time-series have been scaled to that the arrows are equal in magnitude at S8. (c) The tidal variation measured on the fore reef.

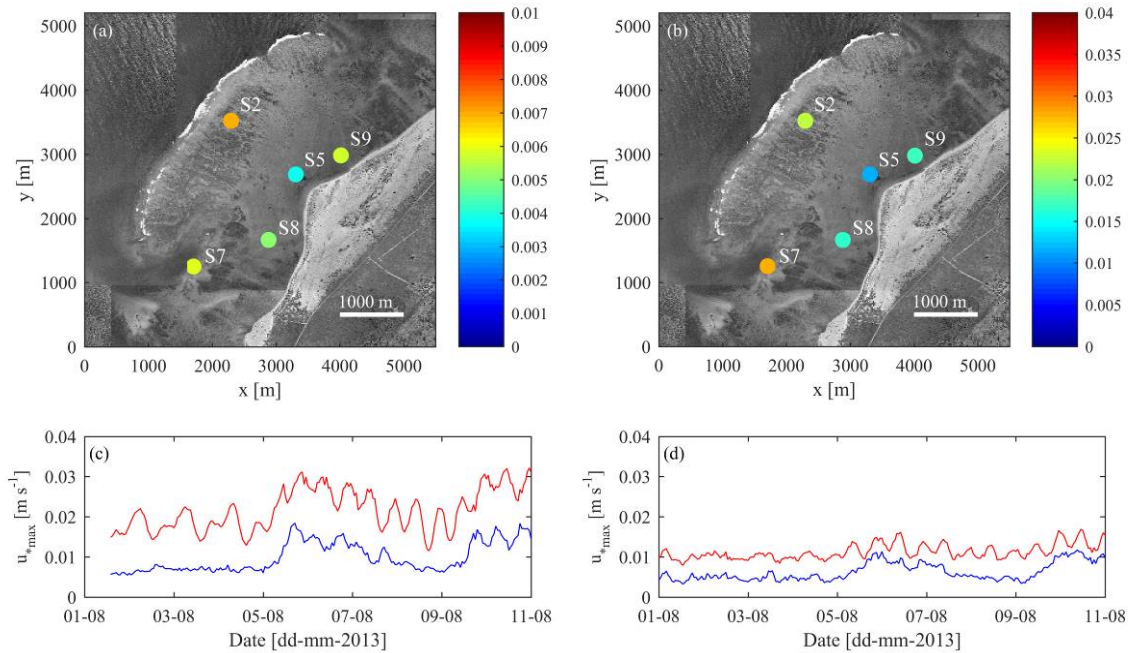


Figure 3.7. The (a) mean wave-current shear velocity u_{*m} and the (b) maximum wave-current shear velocity u_{*max} . The colorbars denote the shear velocities in $m\ s^{-1}$. Note (a) and (b) have a different color scale. The maximum wave-current shear velocities near the bed on the reef flat at S2 within the roughness (red) and in the lagoon near the tip of the salient at S5 (blue) for (c) sea-swell wave-current conditions $u_{*max,sw}$ and (d) infragravity wave-current conditions $u_{*max,ig}$.

Shear velocities

The mean wave-current shear velocity u_{*m} was greatest on the reef flat at S2 while in the lagoon the u_{*m} near the tip of the salient at S5 was substantially smaller (~55% of the u_{*m} measured at S2, Figure 3.7a). North and south of the salient, less reduction was observed despite these sites being located at a similar distance from the shoreline as well as in a similar water depth as S5. The u_{*m} in the southern channel at S7 was slightly higher than the lagoon stations but remained smaller than at S2. A similar spatial distribution was observed for the maximum wave-current shear stress u_{*max} , except that the largest values were observed at S7 in the channel where the waves were larger and not at S2 (Figure 3.7b).

The maximum shear stress for sea-swell wave frequencies combined with currents $u_{*max,sw}$ was modulated by

the tide and consistently greater at S2 than at S5 (Figure 3.7c). The maximum enhanced shear stress for infragravity wave frequencies combined with currents $u_{*max,ig}$ was also larger at S2 (Figure 3.7d), but at both locations the $u_{*max,ig}$ was always less than $u_{*max,sw}$ despite the increased importance of infragravity wave frequencies to the wave height in the lagoon at different times during the experiment (Figure 3.3). Tidal modulation of $u_{*max,ig}$ was also observed, however this modulation was weak and predominantly occurred during the two swell events. In addition to tidal modulation, both $u_{*max,sw}$ and $u_{*max,ig}$ were enhanced during the swell events.

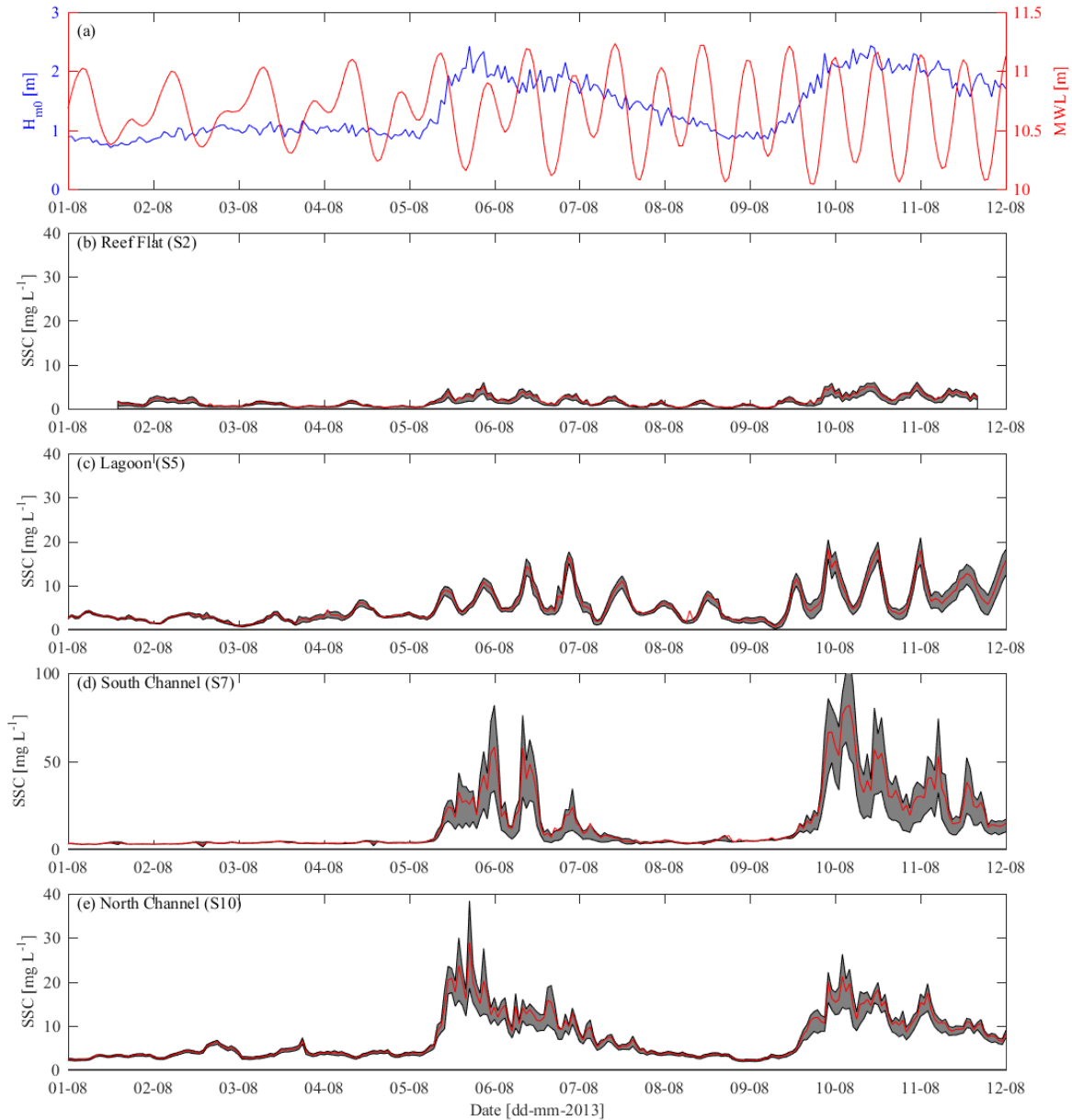


Figure 3.8. (a) Incident wave forcing (H_{m0}) and tidal conditions (MWL) on the forereef at S1. Hourly mean suspended sediment concentrations are shown in red on (b) the reef flat at S2, (c) in the lagoon at S5, (d) in the southern channel at S7 and (e) in the northern channel at S10. The lower limit represents the 1st quartile while the upper limit indicates the 3rd quartile for each hourly burst of data. Note the different y-axis scale in (d).

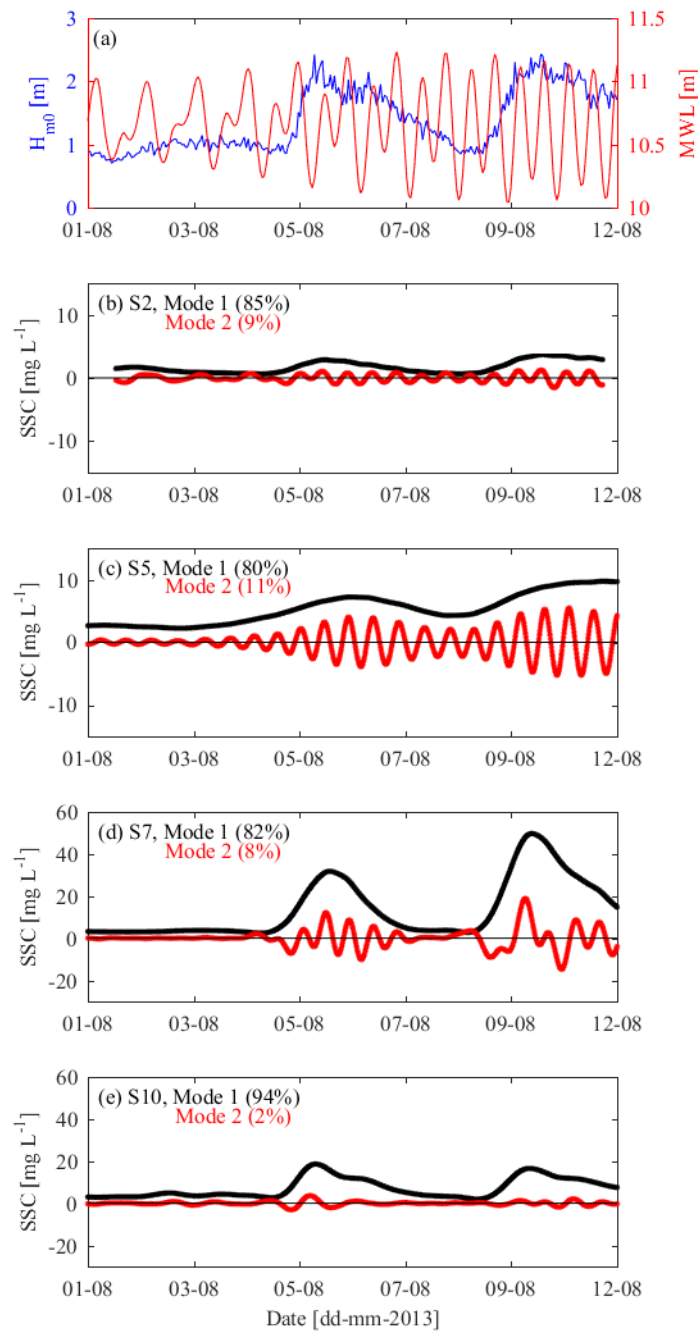


Figure 3.9. (a) Incident wave forcing (H_{m0}) and tidal conditions (MWL) on the forereef at S1. Reconstructed time-series from Singular Spectral Analysis ($M=36$ hrs) of the two modes that explained the majority of signal variance (b) reef flat at S2, (c) lagoon at S5, (d) southern channel at S7 and (e) northern channel at S10.

Suspended sediment concentration variability

Early in the experiment when the waves were low (1–6 Aug), the SSC on the reef flat at S2 varied from $\sim 0.5 \text{ mg L}^{-1}$ at low tide to $\sim 2\text{--}3 \text{ mg L}^{-1}$ at high tide (Figure 3.8b). During the larger swell events spanning 5–8 Aug and 9–12 Aug, the SSCs were consistently higher and peaked at $\sim 8 \text{ mg L}^{-1}$ but continued to vary with tidal phase (Figure 3.8a). In contrast, in the lagoon near the tip of the salient (S5), the suspended sediment was almost twice as large and ranged from $\sim 2 \text{ mg L}^{-1}$ at low swell conditions to $\sim 4\text{--}20 \text{ mg L}^{-1}$ during the larger swell events (Figure 3.8c). The influence of the large swell events can be clearly distinguished as well as the tidal variability that was also observed at S2, although at S5 the tidal signal was much stronger.

The temporal decomposition of the SSC time-series at S2 using Singular-Spectrum Analysis (SSA) revealed that ~94% of the variability is described by two modes (Figure 3.9b). The first mode accounted for ~85% of the variance in the SSC, and was strongly correlated with sub-tidal variability in the offshore wave conditions ($R=0.96$) with zero lag between the forereef $H_{m0,sw}$ (Figure 3.9a) and the SSC. A further ~9% of the SSC variance occurred at semi-diurnal tidal timescales (Figure 3.9b). Similar modes of SSC variability were also observed in the measurements at S5 (Figure 3.9c), where ~90% of the variability could again be explained by two modes that consisted of a dominant sub-tidal mode that varied with the offshore wave conditions ($R=0.88$) and a semi-diurnal tidal mode. In contrast to the SSC measured at S2, the SSC at S5 was consistently higher and exhibited greater variability with both the tidal phase and the two offshore swell events measured in the experiment.

The SSC measured in the southern channel (S7) ranged from ~3 mg L⁻¹ at low tide to ~5 mg L⁻¹ at high tide when the waves were small Figure 3.8d). However, during the larger swell events (Figure 3.9a), the concentration was substantially greater with a peak hourly mean of ~80 mg L⁻¹. This was an order of magnitude larger than what was measured at S2 and approximately four times larger than that measured at S5. A similar pattern in the SSC variability was also measured at S10, except that the magnitude was smaller (Figure 3.8e). At both channel locations, temporal decomposition of the SSC time-series using SSA revealed that most of the SSC variability occurred at sub-tidal timescales (82-93%, Mode 1 in Figure 3.9d and e). During the swell events, modulation of the SSC was also observed over shorter time periods (particularly at S7) where the SSC varied at semidiurnal timescales, however this variability only accounted for 8% of the total SSC variability (Mode 2 in Figure 3.9d). Similar variability was also observed during the swell events at S10 but this signal was very weak.

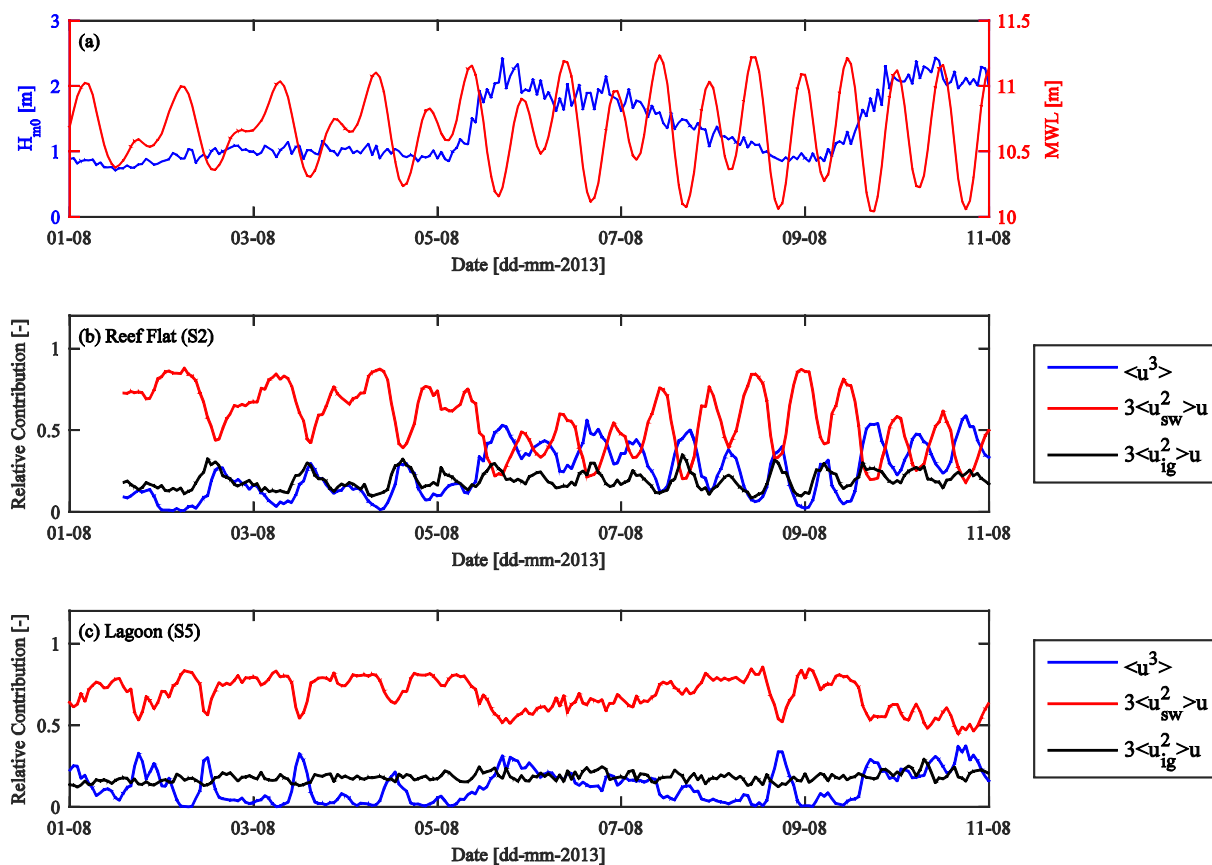


Figure 3.10. (a) Incident wave forcing (H_{m0}) and tidal conditions (MWL) on the forereef at S1. The normalized magnitude of the decomposed third velocity moment terms on (a) the reef flat at S2 and (b) in the lagoon at S5. Note that other terms in the decomposition were negligible and have not been shown for clarity.

Relative importance of waves and currents

The decomposed third velocity moment (u^3) provided insight into the relative importance of sea-swell waves, infragravity waves and currents to the nonlinearity of the nearbed velocity. On the reef flat at S2 (Figure 3.10b), the term that represented sea-swell wave combined with mean currents ($3\langle u_{sw}^2 \rangle \bar{u}$) was substantially larger than the other terms throughout most of the experiment. However, as water depth on the reef flat decreased (Figure 3.10a), $3\langle u_{sw}^2 \rangle \bar{u}$ also decreased and the contribution of other terms to u^3 also became nearly substantial. During lower tidal stages with relatively low waves, the contribution of infragravity waves combined with mean currents ($3\langle u_{ig}^2 \rangle \bar{u}$), as well as the mean currents alone ($\langle u^3 \rangle$), increased. While there appeared to be an upper limit to the relative contribution by $3\langle u_{ig}^2 \rangle \bar{u}$, during the swell events $\langle u^3 \rangle$ made a substantial contribution to u^3 and at low tidal states made an equivalent or slightly greater contribution to u^3 as the other terms.

$3\langle u_{sw}^2 \rangle \bar{u}$ was also the dominant term within the lagoon at S5 (Figure 3.10c) throughout the entire experiment. The contribution to u^3 made by the remaining two terms was different to that observed at S2. $3\langle u_{ig}^2 \rangle \bar{u}$ was constant and relatively low throughout the experiment while $\langle u^3 \rangle$ varied from almost no contribution at higher tidal states to a contribution similar to $3\langle u_{ig}^2 \rangle \bar{u}$. There was very little impact on the relative weighting of the various terms during swell events except that the contribution by $\langle u^3 \rangle$ began to correlate with the offshore wave height and not to the mean water depth.

These results suggest that on a reef flat, sea-swell waves, infragravity waves and mean currents may make a contribution to transport of sediment, especially at different tidal states. However, despite the relative increase in the importance of infragravity waves in fringing reef lagoons, these results suggest that sea-swell waves might continue to remain an important, and even a dominant, contributor to the nonlinearity of the near bed velocity and thus may remain a key driver of sediment transport.

3.4 Discussion

Numerous studies have measured suspended sediment concentrations for a wide range of reefs in the Caribbean (e.g., Hubbard, 1986), Pacific ocean (e.g., Ogston et al., 2004; Storlazzi et al., 2004; Presto et al., 2006), Indian ocean (e.g., Morgan and Kench, 2014) and Great Barrier Reef (e.g., Vila-Concejo et al., 2013). However, these studies have not focused on how different hydrodynamic mechanisms contribute to spatial patterns in sediment transport across a reef-lagoon system. This field study provides new quantitative insight into the relative importance of sea-swell waves, infragravity waves and mean currents, and how these processes relate to the temporal and spatial variability of shear stress and SSCs in fringing reef environments.

In this study, SSCs measured at all locations varied at sub-tidal and intra-tidal timescales but the magnitude of the concentrations differed. The SSCs measured on the reef flat were consistently lower than the SSC measured within the lagoon and channel regions. While the increased concentration in the channels can be explained by the much larger waves that could propagate into the channels, which resulted in higher maximum wave-current shear stresses ($u_{*,max}$), the difference in the magnitude of the concentration between the reef flat at S2 and the lagoon near the salient at S5 is of particular interest because shear stresses in many fringing reef lagoons are often thought to be insufficient to suspend new sediment (e.g., Brander et al., 2004). There are broadly three possible explanations for greater SSCs near the salient when compared to the reef flat: (1) spatial differences in hydrodynamic processes, (2) the presence of large bottom roughness on the reef flat, and (3) the availability of sediment that may be suspended, which is a function of the grain size distribution of bed sediment. Here we consider each of these explanations in the context of the field data.

Influence of different hydrodynamic processes

Hydrodynamic processes affect suspended sediment concentrations by locally suspending sediment from the bed and/or advecting sediment suspended in the water column. In reef environments, as the water depth rapidly decreases incident wave breaking on the forereef limits the propagation of larger swell waves onto the reef flat and generates cross-reef currents (e.g., Lowe et al., 2009c; Taebi et al., 2011). Furthermore, increased dissipation of swell waves due to wave breaking and bed friction on the reef flat has been shown to result in the swell waves

on the reef flat becoming similar in height to the longer infragravity waves (e.g., Pomeroy et al., 2012b; Harris et al., 2015). It is therefore of particular interest to compare the relative importance of the sea-swell waves, infragravity waves and currents on the reef flat to those in the lagoon, and how they may relate to the measured SSC.

The SSC measured on the reef flat and in the lagoon varied at intra-tidal timescales. Intratidal modulation was also observed in the relative contribution of $3\langle u_{sw}^2 \rangle \bar{u}$ to the reef flat nearbed velocity skewness, which also decreased with the decrease in water depth. This reduction is consistent with decreased sea-swell wave heights on the reef flat as larger waves break on the forereef. At lower water depths, the increase in the relative importance of infragravity waves combined with mean currents ($3\langle u_{ig}^2 \rangle \bar{u}$) as well as mean currents alone ($\langle u^3 \rangle$) suggests that these processes may become important. The increased contribution made by these terms is consistent with the intensification of the cross-reef current as demonstrated by the Empirical Orthogonal Function analysis that occurred at both sub-tidal and intratidal timescales. These velocity moment observations were consistent with the laboratory experiment by Pomeroy et al. (2015) that demonstrated that on the rough reef flat, $3\langle u_{sw}^2 \rangle \bar{u}$ was the dominant term at deep water but that $3\langle u_{ig}^2 \rangle \bar{u}$ made an increased contribution to u^3 at shallow water depths. Although in that laboratory experiment, the Eulerian flow was directed offshore as a return current whereas in the field data described by this experiment the Eulerian flow was onshore directed due to the presence of the channels. However, the reduction in SSC at lower water depths suggest that these processes do not play a substantial role in governing the SSC on the reef flat, which is also demonstrated by $u_{*max,ig}$ consistently remaining lower than $u_{*max,sw}$. This is due to the long period of these waves, which reduces the near bed velocity of these waves for a given height as well as reduces the bed friction factor (e.g., Madsen, 1994). Thus, while the infragravity waves may increase in relative importance as measured by nearbed velocity skewness, the impact of these waves as measured by the shear velocity at the bed, suggests that these waves do not have a major impact on the SSC - at least when considered independently of the sea-swell waves.

In the lagoon, $3\langle u_{sw}^2 \rangle \bar{u}$ was consistently the largest contributor to the nearbed velocity skewness. While the dissipation of infragravity waves across the reef and lagoon observed in this experiment may have contributed to the dominance of $3\langle u_{sw}^2 \rangle \bar{u}$, the two-dimensional nature of the hydrodynamic processes at this site enabled greater sea-swell wave energy to propagate to the shoreline than for more alongshore uniform fringing reef systems (e.g., Van Dongeren et al., 2013). This additional wave energy originated from the southern channel, whose deeper depth enabled larger sea-swell waves to propagate beyond the reef crest and into the lagoon. It was also a major contributor to the mean sea-swell wave directions measured near the salient. The low contribution made by the mean currents is consistent with the substantial reduction in the current magnitude in the lagoon area. Thus, the intratidal and sub-tidal variability in the SSC can be explained by the modulation of sea-swell waves and mean currents but not the absolute magnitude between the measurement locations.

Influence of large bottom roughness

Laboratory experiments (e.g., Lowe et al., 2005a, 2008; Luhar et al., 2010) have demonstrated that the presence of roughness can attenuate the waves and currents above as well as within the roughness, which results in a reduction in the bed shear stresses (e.g., Le Bouteiller and Venditti, 2015; Stocking et al., 2016). This was also demonstrated at this study site in Section 2, where it was shown that the shear stresses that arise from the large canopy drag forces imposed on the overlying flow did not represent the actual shear stress imparted on the underlying bed sediment. The actual shear stress, demonstrated by the fineness of the suspended fraction, was substantially smaller.

However, the present study has shown that despite the presence of large bed roughness on the reef flat, the mean u_{*m} and maximum u_{*max} shear velocity calculated near the bed and within the roughness were still greater than the u_{*m} and u_{*max} calculated near the bare sandy bed in the lagoon. Thus, the shear velocity alone cannot explain the difference in SSC magnitude. The reduction in the shear velocity within the lagoon can be explained by two key hydrodynamic controls: (1) the morphological control imposed on the waves by the reef flat water depth, which limits the height of the waves that can propagate over the reef and into the lagoon; and (2) an

increase in the lagoon water depth landward of the reef flat, which reduces the wave orbital velocities near the bed and decreases the magnitude of the wave-driven current. These two hydrodynamic controls also result in a reduction of the shear velocities in the lagoon relative to those on the reef flat. Some enhancement of the shear velocities on either side of the salient was observed in this experiment due to the propagation of waves through breaks in the reef (channels) into the lagoon, however this enhanced shear stress was still lower than the shear stress on the reef flat within the canopy. Thus, the spatial difference in shear velocity between S2 and S5 can be explained by the reef geometry but not the difference in SSC.

Sediment availability

A plausible explanation for the difference in the SSC magnitude between the reef flat and the lagoon is the advection of sediment from the reef flat towards the shoreline that may supplement locally suspended sediment. However, the median grain size observed in suspension on the reef flat was $\sim 70 \mu\text{m}$ (Section 3) and therefore can be expected to take $\sim 640 \text{ s}$ to settle through the roughly $\sim 3 \text{ m}$ lagoon water depth (without resuspension of the sediment within the water column). The Eulerian and Lagrangian measurements of the mean current in this study also indicate that the current decreases in magnitude from the reef crest to the shoreline and therefore the sediment would only travel $\sim 60 \text{ m}$ from the back of the lagoon before the sediment is deposited onto the seabed. The distance between the back of the reef and the salient is $\sim 1200 \text{ m}$. Furthermore, the Lagrangian measurements, along with the flow pathways identified by the EOF analysis, indicate that the flow that transports suspended sediment within the lagoon does not converge at the salient but instead diverges. Excluding increased sediment suspension as well as sediment advection as the primary causes of the concentration discrepancy between the reef flat and the lagoon, another explanation of the reduced SSC on the reef, relative to in the lagoon, is the availability of sediment for suspension.

On the reef flat, bed sediment is interspersed between roughness elements that may occupy a large proportion of the planform area reducing the area over which sediment can be entrained and therefore, when compared to a sandy bed lagoon, there is less sediment available for transport. In addition to the limited availability of sediment on the reef flat, wave-driven currents in reef environments are consistently directed across the reef (e.g., Taebi et al., 2011) and thus continually transport finer sediment suspended from the bed on the reef into the lagoon (the sediment that remains on the reef flat is coarser than the sediment observed in a lagoon, Figure 3.11). While this experiment did not quantify the volume of sediment available for transport on the reef flat, comparison of the bed sediment grain size distribution demonstrates that in the lagoon the bed sediment is substantially finer than the sediment on the reef flat. A larger shear stress is required to suspend the reef sediment and thus explains the reduced concentration of fine sediment observed on the reef flat; there is more finer sediment available for suspension in the lagoon.

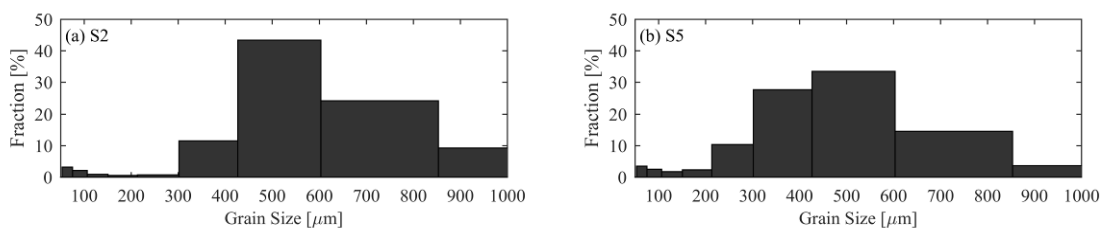


Figure 3.11. Grain size distribution of bed surface sediment on (a) the reef flat at S2 within the roughness and (b) in the lagoon at S5 near the salient.

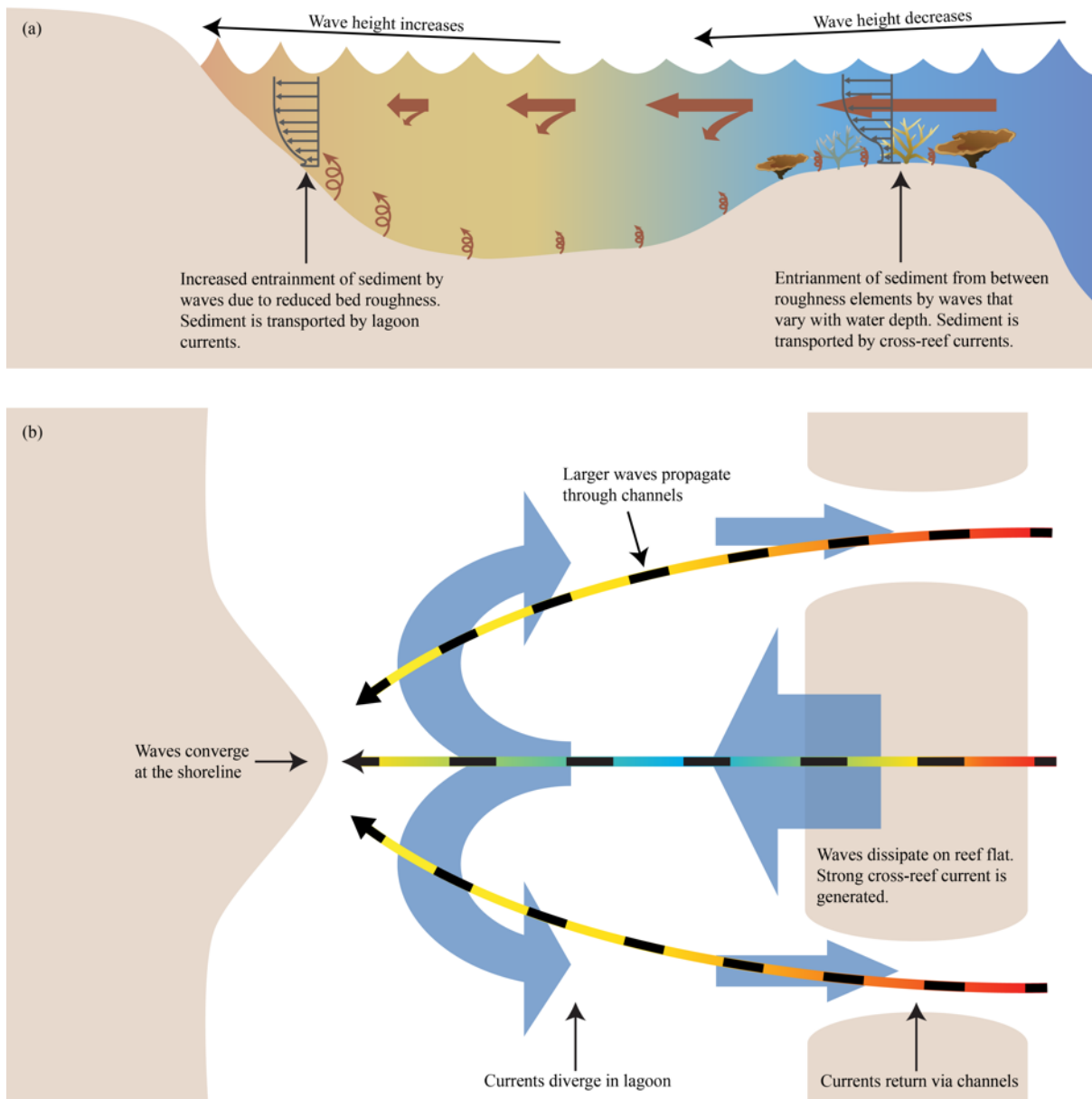


Figure 3.12. Conceptual model of sediment transport processes in a fringing coral reef. (a) Cross section of waves, currents and sediment process across a reef and lagoon. Brown arrows indicate the direction of sediment transport by currents and the upward arrows indicate sediment resuspension. (b) Plan view of the wave rays and current pathways throughout a reef system. The colour gradient in (a) indicates increased turbidity (brown indicates high turbidity and blue low turbidity) while in (b) the gradient indicates the change in wave height (red corresponds to larger waves and blue to smaller waves).

Synthesis: mechanisms and pathways of sediment transport in fringing reefs

In the context of this study, a conceptual model (Figure 3.12) for sediment transport in a fringing coral reef is proposed.

Large incident swell waves break in the narrow surf zone region near the reef crest (Figure 3.12a). The extent of wave breaking depends on the offshore wave height (varying over sub-tidal time scales) and tidal variations in the reef flat water depth. Cross-reef wave-driven currents are also affected by the variation in the water depth and thus vary over sub-tidal and intra-tidal time scales. At high tidal elevations, larger swell waves propagate over the reef flat, which enhance sediment entrainment from the bed. As the tidal water depth decreases and more swell waves are dissipated by wave breaking, cross-reef currents increase (due to a reduced water depth) and infragravity waves make an increasing contribution to the reef flat wave height. However, this increase in

infragravity wave importance does not result in these shear stresses becoming the dominant stress imposed on the sediment; the depth limited sea-swell waves continue to impose the largest bed stresses. However, on the reef flat the presence of large immobile roughness elements that occupy a substantial fraction of the plan area, as well as the continual transportation of sediment across the reef flat into the lagoon, results in relatively low quantities of sediment available for suspension into the water column resulting low suspended sediment concentration on the reef flat for a given shear stress.

Within the lagoon (Figure 3.12b), the waves and currents decrease in magnitude. However, wave propagation through the channels into the lagoon increases the wave height close to the shoreline. These slightly larger wave heights, along with the reduced bottom roughness and greater sediment availability, enable more sediment entrainment and higher concentrations in the lagoon (in particular close to the shoreline). Sediment that is suspended within the lagoon is transported by shoreward directed currents that diverge near the shoreline, converge and increase in magnitude in the channels and exit through the channels as a relatively strong narrow current. While suspended sediment will predominantly be transported to both the north and south by cross-reef currents flowing towards the two channels, under favorable alongshore wind conditions sediment may also be directed in one direction, which in the case of this experiment is to the north.

3.5 Conclusions

In this study, we conducted a broad-scale hydrodynamic and sediment transport field experiment throughout a fringing reef system to investigate the variability of sea-swell waves, infragravity waves, mean currents and SSCs at different spatial and temporal scales. The key results of this study were as follows:

1. Sea-swell wave heights within the lagoon can be slightly larger than those that propagate across the reef flat due to the propagation of waves through the breaks (channels) in the reef flat. The height of these waves in the channels is related to the offshore wave conditions, and contribute to elevated wave heights on either side of the salient.
2. The mean flow within the reef system was predominantly driven by sub-tidal variations in the offshore wave conditions; however, when the offshore waves were small and alongshore wind persistent, flows could occasionally be driven directly by the wind. In addition to the sub-tidal variability, flow within the lagoon also varies at tidal timescales. This variability in the alongshore was driven by the propagation of the tidal flow through the lagoon while in the cross-shore was due to tidal modulation of wave breaking induced flow.
3. On the reef flat, sea-swell waves combined with currents was the main contributor to the nearbed velocity skewness. However, as the water level on the reef flat decreased, longer infragravity waves as well as the mean current become relatively more important. Thus, sea-swell waves, infragravity waves and currents may all contribute to sediment transport processes on the reef flat. In the lagoon, the nearbed velocity skewness was overwhelmingly due to the sea-swell wave-current interaction only.
4. Suspended sediment variability on the reef flat was smaller than in the lagoon or channels. However, throughout the system a majority of the SSC variability could be explained by variations over sub-tidal timescales with less variance in the concentration occurring at intra-tidal timescales.

3.6 References

- Acevedo, R., Morelock, J., & Olivieri, R. A. (1989). Modification of Coral Reef Zonation by Terrigenous Sediment Stress. *PALAIOS*, 4(1), 92–100.
- Anthony, K. (2000). Enhanced particle-feeding capacity of corals on turbid reefs (Great Barrier Reef, Australia). *Coral Reefs*, 19(19), 59–67.
- Australian Institute of Marine Science. (2013). AIMS Ningaloo Reef Platform. Retrieved November 13, 2014, from <http://data.aims.gov.au/aimsrtds>
- Bagnold, R. A. (1966). An approach to the sediment transport problem from general physics. *US Geol. Surv. Prof. Pap.*, 422–I, 11–137.
- de Bakker, A., Tissier, M., & Ruessink, B. (2013). Shoreline dissipation of infragravity waves. *Continental Shelf Research*.
- Beadsley, R. C., Limeburner, R., & Rosenfeld, L. K. (1985). Introduction to the CODE-2 moored array and large-scale data report. *CODE-2: Moored Array and Large-Scale Data Report*, 85–35.
- Bosman, J. J., van der Velden, E. T. J. M., & Hulsbergen, C. H. (1987). Sediment concentration measurement by transverse suction. *Coastal Engineering*, 11(4), 353–370. [https://doi.org/10.1016/0378-3839\(87\)90033-0](https://doi.org/10.1016/0378-3839(87)90033-0)
- Brander, R. W., Kench, P. S., & Hart, D. (2004). Spatial and temporal variations in wave characteristics across a reef platform, Warraber Island, Torres Strait, Australia. *Marine Geology*, 207(1–4), 169–184. <https://doi.org/10.1016/j.margeo.2004.03.014>
- Buddemeier, R., & Hopley, D. (1988). Turn-ons and turn-offs: causes and mechanisms of the initiation and termination of coral reef growth. Lawrence Livermore National Lab., CA (USA).
- Cheriton, O. M., Storlazzi, C. D., & Rosenberger, K. J. (2016). Observations of wave transformation over a fringing coral reef and the importance of low-frequency waves and offshore water levels to runoff, overwash, and coastal flooding. *Journal of Geophysical Research: Oceans*.
- Cordier, E., Poizat, E., & Méar, Y. (2012). Swell impact on reef sedimentary processes: A case study of the La Reunion fringing reef. *Sedimentology*, 59(7), 2004–2023. <https://doi.org/10.1111/j.1365-3091.2012.01332.x>
- Coronado, C., Candela, J., Iglesias-Prieto, R., Sheinbaum, J., López, M., & Ocampo-Torres, F. J. (2007). On the circulation in the Puerto Morelos fringing reef lagoon. *Coral Reefs*, 26, 149–163. <https://doi.org/10.1007/s00338-006-0175-9>
- Cuttler, M. V. W., Lowe, R. J., Falter, J. L., & Buscombe, D. (2017). Estimating the settling velocity of bioclastic sediment using common grain-size analysis techniques. *Sedimentology*, 64(4), 987–1004. <https://doi.org/10.1111/sed.12338>
- Cuttler, M. V. W., Lowe, R., Hansen, J., Falter, J., & Pomeroy, A. W. M. (2015). Grainsize, composition and beform patterns in a fringing reef system. *The Proceedings of Coastal Sediments*.
- Dalrymple, R. A., MacMahan, J. H., Reniers, A. J., & Nelko, V. (2011). Rip currents. *Annual Review of Fluid Mechanics*, 43, 551–581.
- Emery, W. J., & Thomson, R. E. (2001). *Data analysis methods in physical oceanography*. Elsevier Science.
- Ertfemeijer, P. L., Riegl, B., Hoeksema, B. W., & Todd, P. A. (2012). Environmental impacts of dredging and other sediment disturbances on corals: a review. *Marine Pollution Bulletin*, 64(9), 1737–1765.
- Francis, J. (1973). Experiments on the motion of solitary grains along the bed of a water-stream, 332, 443–471. <https://doi.org/10.1098/rspa.1973.0037>
- Goring, D., & Nikora, V. (2002). Despiking Acoustic Doppler Velocimeter Data. *Journal of Hydraulic Engineering*, 128(1), 117–126. [https://doi.org/10.1061/\(ASCE\)0733-9429\(2002\)128:1\(117\)](https://doi.org/10.1061/(ASCE)0733-9429(2002)128:1(117))
- Gourlay, M. R. (1994). Wave transformation on a coral reef. *Coastal Engineering*, 23(1–2), 17–42. [https://doi.org/10.1016/0378-3839\(94\)90013-2](https://doi.org/10.1016/0378-3839(94)90013-2)
- Gourlay, M. R. (1996a). Wave set-up on coral reefs. 1. Set-up and wave-generated flow on an idealised two dimensional horizontal reef. *Coastal Engineering*, 27(3–4), 161–193. [https://doi.org/10.1016/0378-3839\(96\)00008-7](https://doi.org/10.1016/0378-3839(96)00008-7)
- Gourlay, M. R. (1996b). Wave set-up on coral reefs. 2. set-up on reefs with various profiles. *Coastal Engineering*, 28(1–4), 17–55. [https://doi.org/10.1016/0378-3839\(96\)00009-9](https://doi.org/10.1016/0378-3839(96)00009-9)
- Gourlay, M. R., & Colleter, G. (2005). Wave-generated flow on coral reefs -an analysis for two-dimensional horizontal reef-tops with steep faces. *Coastal Eng*, 52(4), 353–387. <https://doi.org/10.1016/j.coastaleng.2004.11.007>
- Grant, W. D., & Madsen, O. S. (1979). Combined wave and current interaction with a rough bottom. *Journal of Geophysical Research: Oceans (1978–2012)*, 84(C4), 1797–1808.
- Ha, H., Maa, J.-Y., Park, K., & Kim, Y. (2011). Estimation of high-resolution sediment concentration profiles in bottom boundary layer using pulse-coherent acoustic Doppler current profilers. *Marine Geology*, 279(1), 199–209.

- Hardy, T. A., & Young, I. R. (1996). Field study of wave attenuation on an offshore coral reef. *Journal of Geophysical Research: Oceans*, 101(C6), 14311–14326. <https://doi.org/10.1029/96jc00202>
- Harris, D. L., Vila-Concejo, A., & Webster, J. M. (2014). Geomorphology and sediment transport on a submerged back-reef sand apron: One Tree Reef, Great Barrier Reef. *Geomorphology*, 222, 132–142. <https://doi.org/10.1016/j.geomorph.2014.03.015>
- Hearn, C. J. (1999). Wave-breaking hydrodynamics within coral reef systems and the effect of changing relative sea level. *J. Geophys. Res.*, 104, 30007–30019. <https://doi.org/10.1029/1999jc900262>
- Hench, J. L., Leichter, J. J., & Monismith, S. G. (2008). Episodic circulation and exchange in a wave-driven coral reef and lagoon system. *Limnol. Oceanogr*, 53(6), 2681–2694. <https://doi.org/10.4319/lo.2008.53.6.2681>
- Hubbard, D. K. (1986). Sedimentation as a control of reef development: St. Croix, U.S.V.I. *Coral Reefs*, 5, 117–125. <https://doi.org/10.1007/BF00298179>
- Jago, O., Kench, P., & Brander, R. (2007). Field observations of wave-driven water-level gradients across a coral reef flat. *Journal of Geophysical Research: Oceans* (1978–2012), 112(C6).
- Jokiel, P. L., Rodgers, K. S., Storlazzi, C. D., Field, M. E., Lager, C. V., & Lager, D. (2014). Response of reef corals on a fringing reef flat to elevated suspended-sediment concentrations: Moloka'i, Hawai'i. *PeerJ*, 2, e699. <https://doi.org/10.7717/peerj.699>
- Larcombe, P., Costen, A., & Woolfe, K. J. (2001). The hydrodynamic and sedimentary setting of nearshore coral reefs, central Great Barrier Reef shelf, Australia: Paluma Shoals, a case study. *Sedimentology*, 48(4), 811–835.
- Le Bouteiller, C., & Venditti, J. G. (2015). Sediment transport and shear stress partitioning in a vegetated flow. *Water Resources Research*, 51(4), 2901–2922. <https://doi.org/10.1002/2014WR015825>
- Longuet-Higgins, M. S., & Stewart, R. W. (1962). Radiation stress and mass transport in gravity waves, with application to. *Journal of Fluid Mechanics*, 13(04), 481–504. <https://doi.org/10.1017/S0022112062000877>
- Longuet-Higgins, M. S., & Stewart, R. W. (1964). Radiation stresses in water waves - a physical discussion, with applications. *Deep-Sea Research*, 11(4), 529–562. [https://doi.org/10.1016/0011-7471\(64\)90001-4](https://doi.org/10.1016/0011-7471(64)90001-4)
- Lowe, R. J., Falter, J. L., Monismith, S. G., & Atkinson, M. J. (2009). A numerical study of circulation in a coastal reef-lagoon system. *J. Geophys. Res.*, 114, C06022. <https://doi.org/10.1029/2008jc005081>
- Lowe, R. J., & Falter, J. L. (2015). Oceanic Forcing of Coral Reefs. *Annual Review of Marine Science*, 7(18), 1–25. <https://doi.org/10.1146/annurev-marine-010814-015834>
- Lowe, R. J., Falter, J. L., Bandet, M. D., Pawlak, G., Atkinson, M. J., Monismith, S. G., & Koseff, J. R. (2005). Spectral wave dissipation over a barrier reef. *Journal of Geophysical Research: Oceans*, 110(C04001). <https://doi.org/10.1029/2004jc002711>
- Lowe, R. J., Koseff, J., & Monismith, S. G. (2005). Oscillatory flow through submerged canopies: 1. Velocity structure. *Journal of Geophysical Research: Oceans*, 110(C10016), 1–17. <https://doi.org/10.1029/2004JC002788>
- Lowe, R. J., Shavit, U., Falter, J. L., Koseff, J. R., & Monismith, S. G. (2008). Modeling flow in coral communities with and without waves: A synthesis of porous media and canopy flow approaches. *Limnology and Oceanography*, 53, 2668–2680. <https://doi.org/10.4319/lo.2008.53.6.2668>
- Lugo-Fernández, A., Roberts, H. H., Wiseman Jr, W. J., & Carter, B. L. (1998). Water level and currents of tidal and infragravity periods at Tague Reef, St. Croix (USVI). *Coral Reefs*, 17(4), 343–349. <https://doi.org/10.1007/s003380050137>
- Luhar, M., Coutu, S., Infantes, E., Fox, S., & Nepf, H. (2010). Wave-induced velocities inside a model seagrass bed. *Journal of Geophysical Research: Oceans* (1978–2012), 115(C12). <https://doi.org/10.1029/2010JC006345>
- Madsen, O. S. (1994). Spectral wave-current bottom boundary layer flows. *Coastal Engineering Proceedings*, 1(24). <https://doi.org/10.1061/9780784400890.030>
- Madsen, O. S., Poon, Y.-K., & Graber, H. C. (1988). Spectral wave attenuation by bottom friction: theory. *Coastal Engineering Proceedings*, 1(21). Retrieved from <https://journals.tdl.org/icce/index.php/icce/article/viewArticle/4241>
- Massel, S. R., & Gourlay, M. R. (2000). On the modelling of wave breaking and set-up on coral reefs. *Coastal Eng.* (39), 1–27. [https://doi.org/10.1016/S0378-3839\(99\)00052-6](https://doi.org/10.1016/S0378-3839(99)00052-6)
- Mathisen, P. P., & Madsen, O. S. (1999). Waves and currents over a fixed rippled bed 3. Bottom and apparent roughness for spectral waves and currents. *J. Geophys. Res.*, 104, 18447–18461. <https://doi.org/10.1029/1999jc900114>
- Monismith, S. G. (2007). Hydrodynamics of Coral Reefs. *Annual Review of Fluid Mechanics*, 39, 37–55. <https://doi.org/10.1146/annurev.fluid.38.050304.092125>
- Morgan, K. M., & Kench, P. S. (2014). A detrital sediment budget of a Maldivian reef platform. *Geomorphology*, 222, 122–131. <https://doi.org/10.1016/j.geomorph.2014.02.013>

- Nielsen, P. (1992). Coastal bottom boundary layers and sediment transport (Vol. 4). Singapore: World scientific.
- Ogston, A. S., Storlazzi, C. D., Field, M. E., & Presto, M. K. (2004). Sediment resuspension and transport patterns on a fringing reef flat, Molokai, Hawaii. *Coral Reefs*, 23(4), 559–569. <https://doi.org/10.1007/s00338-004-0415-9>
- O'Hara Murray, R. B., Thorne, P., & Hodgson, D. (2011). Intrawave observations of sediment entrainment processes above sand ripples under irregular waves. *Journal of Geophysical Research*, 116(C1), C01001. <https://doi.org/10.1029/2010JC006216>
- Péquignet, A.-C. N., Becker, J. M., Merrifield, M. A., & Aucan, Jè. (2009). Forcing of resonant modes on a fringing reef during tropical storm Man-Yi. *Geophysical Research Letters*, 36(L03607). <https://doi.org/10.1029/2008gl036259>
- Péquignet, A.-C. N., Becker, J. M., & Merrifield, M. A. (2014). Energy transfer between wind waves and low-frequency oscillations on a fringing reef, Ipan, Guam. *Journal of Geophysical Research: Oceans*, 119. <https://doi.org/10.1002/2014JC010179>
- Pomeroy, A. W. M., Lowe, R. J., Symonds, G., Van Dongeren, A., & Moore, C. (2012). The dynamics of infragravity wave transformation over a fringing reef. *Journal of Geophysical Research: Oceans*, 117(C11), C11022. <https://doi.org/10.1029/2012JC008310>
- Pomeroy, A. W. M., Lowe, R. J., Ghisalberti, M., Storlazzi, C. D., Symonds, G., & Roelvink, D. (2017). Sediment transport in the presence of large reef bottom roughness. *Journal of Geophysical Research: Oceans*.
- Presto, M. K., Ogston, A. S., Storlazzi, C. D., & Field, M. E. (2006). Temporal and spatial variability in the flow and dispersal of suspended-sediment on a fringing reef flat, Molokai, Hawaii. *Estuarine, Coastal and Shelf Science*, 67, 67–81. <https://doi.org/10.1016/j.ecss.2005.10.015>
- Roeber, V., & Bricker, J. D. (2015). Destructive tsunami-like wave generated by surf beat over a coral reef during Typhoon Haiyan. *Nature Communications*, 6, 7854. <https://doi.org/10.1038/ncomms8854>
- Rogers, C. S. (1990). Responses of coral reefs and reef organisms to sedimentation. *Marine Ecology Progress Series*.
- Roth, M. S. (2014). The engine of the reef: photobiology of the coral–algal symbiosis. *Frontiers in Microbiology*, 5, 422. <https://doi.org/10.3389/fmicb.2014.00422>
- Roy, K. J., & Smith, S. V. (1970). Sedimentation and coral reef development in turbid water: Fanning Lagoon. *Hawaii Institute of Geophysics Contribution*, (358).
- Schmidt, W. E., Guza, R. T., & Slinn, D. N. (2005). Surf zone currents over irregular bathymetry: Drifter observations and numerical simulations. *Journal of Geophysical Research*, 110(C12). <https://doi.org/10.1029/2004JC002421>
- Schoellhamer, D. H. (2002). Variability of suspended-sediment concentration at tidal to annual time scales in San Francisco Bay, USA. *Continental Shelf Research*, 22(11–13), 1857–1866. [https://doi.org/10.1016/S0278-4343\(02\)00042-0](https://doi.org/10.1016/S0278-4343(02)00042-0)
- Sheremet, A., Kaihatu, J. M., Su, S. F., Smith, E. R., & Smith, J. M. (2011). Modeling of nonlinear wave propagation over fringing reefs. *Coastal Engineering*, 58(12), 1125–1137. <https://doi.org/10.1016/j.coastaleng.2011.06.007>
- Shields, A. (1936). Application of similarity principles and turbulence research to bed-load movement.
- Soulsby, R., & Clarke, S. (2005). Bed shear-stresses under combined waves and currents on smooth and rough beds. *HR Wallingford, Report TR137*.
- Stocking, J. B., Rippe, J. P., & Reidenbach, M. A. (2016). Structure and dynamics of turbulent boundary layer flow over healthy and algae-covered corals. *Coral Reefs*, 1–13. <https://doi.org/10.1007/s00338-016-1446-8>
- Storlazzi, C. D., Ogston, A. S., Bothner, M. H., Field, M. E., & Presto, M. K. (2004). Wave- and tidally-driven flow and sediment flux across a fringing coral reef: Southern Molokai, Hawaii. *Continental Shelf Research*, 24(12), 1397–1419. <https://doi.org/10.1016/j.csr.2004.02.010>
- Storlazzi, C. D., Norris, B. K., & Rosenberger, K. J. (2015). The influence of grain size, grain color, and suspended-sediment concentration on light attenuation: Why fine-grained terrestrial sediment is bad for coral reef ecosystems. *Coral Reefs*, 1–9.
- Symonds, G., Huntley, D. A., & Bowen, A. J. (1982). Two dimensional surfbeat: Long wave generation by a time varying breakpoint. *J. Geophys. Res.*, 87, 492–498. <https://doi.org/10.1029/JC087iC01p00492>
- Symonds, G., Black, K. P., & Young, I. R. (1995). Wave-driven flow over shallow reefs. *J. Geophys. Res.*, 100, 2639–2648. <https://doi.org/10.1029/94jc02736>
- Taebi, S., Lowe, R. J., Pattiaratchi, C. B., Ivey, G. N., Symonds, G., & Brinkman, R. (2011). Nearshore circulation in a tropical fringing reef system. *J. Geophys. Res.*, 116, C02016. <https://doi.org/10.1029/2010jc006439>
- Taebi, S., Lowe, R. J., Pattiaratchi, C. B., Ivey, G. N., & Symonds, G. (2012). A numerical study of the dynamics of the wave-driven circulation within a fringing reef system. *Ocean Dynamics*, 62(4), 585–602. <https://doi.org/10.1007/s10236-011-0514-4>

- van Thiel de Vries, J. S. M., van Gent, M. R. A., Walstra, D. J. R., & Reniers, A. J. H. M. (2008). Analysis of dune erosion processes in large-scale flume experiments. *Coastal Engineering*, 55, 1028–1040.
- Thorne, P. D., Davies, A. G., & Williams, J. J. (2003). Measurements of near-bed intra-wave sediment entrainment above vortex ripples. *Geophysical Research Letters*, 30(20), 2028. <https://doi.org/10.1029/2003GL018427>
- Traykovski, P., Hay, A. E., Irish, J. D., & Lynch, J. F. (1999). Geometry, migration, and evolution of wave orbital ripples at LEO-15. *Journal of Geophysical Research: Oceans*, 104(C1), 1505–1524. <https://doi.org/10.1029/1998JC900026>
- Tudhope, A. W., & Scoffin, T. P. (1994). Growth and structure of fringing reefs in a muddy environment, South Thailand. *Journal of Sedimentary Research*, 64(4).
- Van Rijn, L. C. (1984a). Sediment transport, part I: bed load transport. *Journal of Hydraulic Engineering*, 110(10), 1431–1456. [https://doi.org/10.1061/\(ASCE\)0733-9429\(1984\)110:10\(1431\)](https://doi.org/10.1061/(ASCE)0733-9429(1984)110:10(1431))
- Van Rijn, L. C. (1984b). Sediment transport, Part II: Suspended load transport. *Journal of Hydraulic Engineering*, 110(11), 1613–1641. [https://doi.org/10.1061/\(ASCE\)0733-9429\(1984\)110:11\(1613\)](https://doi.org/10.1061/(ASCE)0733-9429(1984)110:11(1613))
- Van Rijn, L. C. (2007). Unified view of sediment transport by currents and waves. III: Graded beds. *Journal of Hydraulic Engineering*, 133(7), 761–775. [https://doi.org/10.1061/\(ASCE\)0733-9429\(2007\)133:7\(761\)](https://doi.org/10.1061/(ASCE)0733-9429(2007)133:7(761))
- Vautard, R., Yiou, P., & Ghil, M. (1992). Singular-spectrum analysis: A toolkit for short, noisy chaotic signals. *Physica D: Nonlinear Phenomena*, 58(1–4), 95–126. [https://doi.org/10.1016/0167-2789\(92\)90103-T](https://doi.org/10.1016/0167-2789(92)90103-T)
- Vila-Concejo, A., Harris, D. L., Power, H. E., Shannon, A. M., & Webster, J. M. (2014). Sediment transport and mixing depth on a coral reef sand apron. *Geomorphology*, 222, 143–150. <https://doi.org/10.1016/j.geomorph.2013.09.034>
- Weber, M., de Beer, D., Lott, C., Polerecky, L., Kohls, K., Abed, R. M., ... Fabricius, K. E. (2012). Mechanisms of damage to corals exposed to sedimentation. *Proceedings of the National Academy of Sciences*, 109(24), E1558–E1567. <https://doi.org/10.1073/pnas.1100715109>

4 Near-bed hydrodynamics and bed shear stresses in canopies with current-dominated flows

Abstract

Both the thresholds for, and rates of, sediment transport in coastal environments are typically described through a bed shear stress (often indicated by the friction velocity, u_*). Recent studies have indicated, however, that the bed stress alone may not control sediment transport in aquatic canopies, and that the strength of near-bed turbulence (the turbulent kinetic energy, TKE) may be dynamically important. Here, we evaluate how these characteristics of the near-bed flow vary with properties of the ambient flow and of the canopy in current-dominated conditions. Flume experiments were conducted in which both u_* and TKE were measured across a wide and realistic range of flow and canopy properties. It is shown that, in terms of its impact on the near-bed flow, a submerged canopy can be uniquely characterised in terms of its roughness density, β . Predictive relationships for both u_* and TKE in terms of β are developed here, and shown to be accurate predictors of the flow characteristics that control sediment transport in aquatic canopies.

4.1 Introduction

The laboratory component of this study investigates (a) the hydrodynamic properties (e.g. bed stress, near-bed turbulence levels) that govern sediment transport in these systems, and (b) the impact of a benthic canopy on the thresholds for, and quantity of, sediment transport. Here, we focus on (a) in canopies subjected to steady (i.e. current-dominated) flows.

Benthic canopies have a profound impact on coastal hydrodynamics by imposing substantial drag forces on the flows generated by waves and currents. This, in turn, results in substantial modifications to the mean and turbulent flow structure near the sea bed. The near-bed hydrodynamics that governs transport of both natural and dredging-derived sediments (which is closely coupled to the hydrodynamics), including rates of sediment deposition and suspension, can be dramatically altered in these environments. The flow structure in and around reef organisms depends on the complex interaction between the overlying water motion and the typically large, three-dimensional canopies formed by benthic organisms such as coral reef communities and seagrasses. The common challenge for understanding the flow dynamics in all natural canopies is how to properly account for the highly variable spatial flow structure that arises within even the simplest morphologies.

In current-dominated flows, the drag exerted by the canopy creates strong flow attenuation within the canopy. This is described by the current attenuation parameter (α_c), which represents the ratio of the free-stream velocity well above the canopy (U_∞) to the near-bed mean velocity (U_b , Figure 4.1). Here, flow velocities in the streamwise (x), lateral (y) and vertical (z) directions are denoted by u , v and w , respectively.

The discontinuity in drag near the top of the canopy generates a region of strong shear in the mean velocity profile (Figure 4.1b). This shear layer transfers momentum from the overlying water column down into the canopy, thus driving flow inside the canopy. Particularly in dense canopies, the shear layer often does not penetrate completely to the bed. This separates the canopy vertically into two zones (Nepf and Vivoni, 2000). The upper zone (termed the ‘exchange zone’) is a region of rapid vertical transport and is driven by both the turbulent stress and the pressure gradient. The lower zone (termed the ‘wake zone’) is governed by a simple balance of drag and pressure gradient, much like classical porous medium flow. The turbulent stress in the wake zone is very small, except in the very thin boundary layer at the bed. The extent of shear layer penetration into a submerged canopy is inversely proportional to a , the canopy frontal area per unit volume. Consequently, ah , the scale ratio of canopy height (h) to exchange zone depth, is a key dimensionless parameter in the description of near-bed hydrodynamics, such as bed stress and sediment transport in canopy flows (Nepf et al. 2007). The near-bed hydrodynamics are also influenced the dimensionless packing density of the canopy, ad , where d is the

characteristic width of canopy elements.

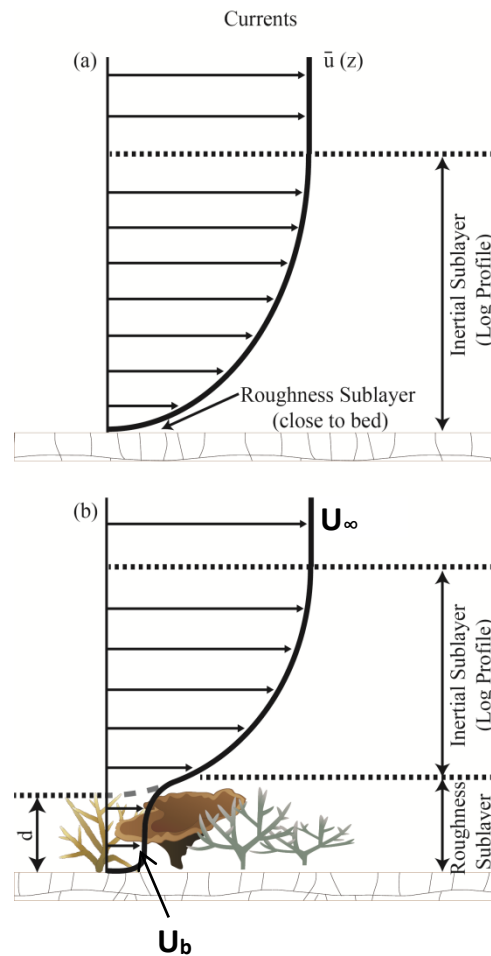


Figure 4.1. Conceptual model of the mean velocity profile over (a) bare beds and (b) canopies under current-dominated conditions.

Sediment transport over bare beds is largely described through a bed shear stress. However, the bed shear stress in aquatic canopies, and its role in driving sediment transport, has largely eluded quantitative description. Furthermore, even if bed stress could be readily predicted, it is unlikely to be the only flow descriptor relevant to sediment transport; the intensity of the turbulence in the flow is almost certainly important as well (see, e.g., Celik et al. 2010, Yang et al., 2016). Over a bare bed, the situation is simplified, as the mean bed stress and turbulence strength are linked.

Thus, the aim of this work is to build predictive capability for the two key hydrodynamic parameters, bed shear stress (τ_b) and near-bed turbulent kinetic energy (TKE), that are expected to govern sediment erosion and deposition in coastal canopies. This requires a systematic laboratory study of the variation of these parameters with ambient flow conditions and canopy properties. The bed shear stress is indicated by the bed friction velocity, $u_* (= \sqrt{\tau_b/\rho})$, where ρ is the fluid density). The turbulent kinetic energy is given by $0.5(\overline{u'^2} + \overline{v'^2} + \overline{w'^2})$, where the prime indicates turbulent fluctuation and the overbar an average over the length of the velocity record.

4.2 Methods

Experimental facilities

Experiments were conducted in two flumes of different scale: a smaller-scale flume at the University of

Melbourne (width = 20 cm, maximum depth = 20 cm, Figure 4.2a) and a larger flume at the University of Western Australia (width = 60 cm, maximum depth = 45 cm, Figure 4.2b). The first flume was used to look at the near-bed hydrodynamics in flows through emergent canopies, whereas the latter was used for investigation of flows over submerged canopies. While coastal canopies tend (but are not invariably) submerged in the water column, the study of emergent canopies removes canopy height (h) as a variable, allowing a much clearer link to be made between in-canopy velocities and bed stress. In both flumes, model canopies were constructed from rigid cylinders of uniform diameter and height. Across the range of experiments, key canopy properties were varied widely: $a = 0.01\text{--}0.33\text{ cm}^{-1}$, $d = 0.6\text{--}5.5\text{ cm}$, $h/H = 0.07\text{--}1$ (where H is the water depth). This ensured that the key dimensionless canopy descriptors had a wide span that mimicked ranges in real aquatic systems ($ah = 0.33\text{--}1.1$; $ad = 0.016\text{--}0.22$). In the smaller flume, eight bare-bed experiments were also run, to isolate the impact of aquatic canopies on the near-bed hydrodynamics.

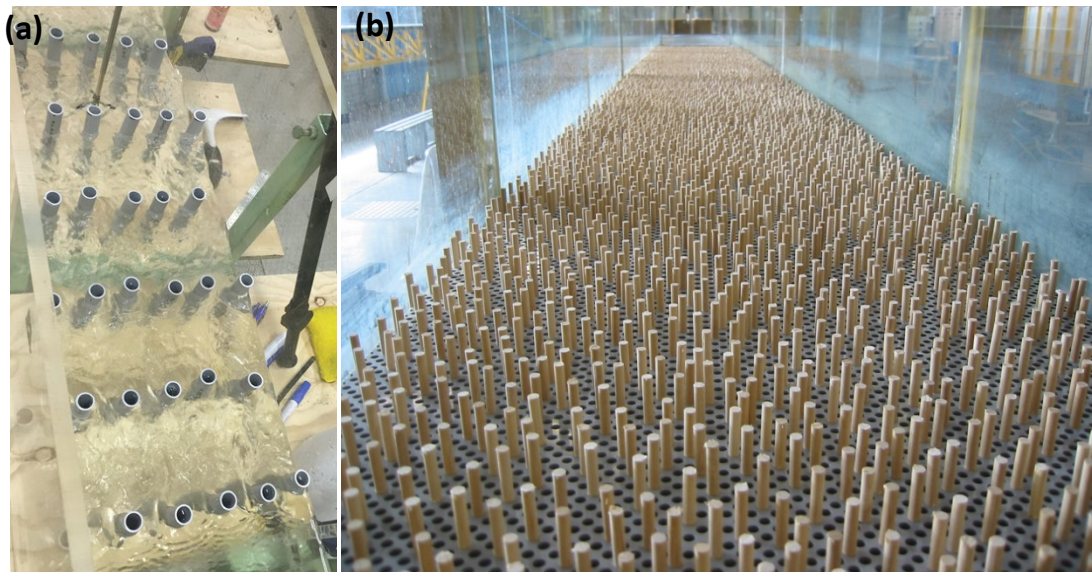


Figure 4.2 The two experimental flumes used in this study: (a) smaller-scale flume at the University of Melbourne (width = 30 cm), and (b) the larger-scale flume (width = 60 cm) at the University of Western Australia. An emergent model canopy ($ad = 0.05$) is shown in (a), and a submerged canopy ($ad = 0.22$) in (b).

Measurement techniques

During each experiment, vertical profiles of velocity records were taken using a Nortek acoustic Doppler velocimeter (ADV). Data were collected for 10 minutes at 25 Hz, with a vertical spacing of less than 1 cm between points in each profile. In the emergent canopy experiments, where a very high resolution is required to determine the maximum turbulent shear stress, an ADV profiler was used with a cell size of 2 mm. To account for the spatial variability in canopy flow, profiles were taken at 3-4 locations within the canopy; all hydrodynamic data presented here represent horizontal averages.

The bed shear stress was estimated as the maximum value of the turbulent shear stress $\overline{u'w'}$ above the viscous sublayer at the flume bed (within which the turbulent stress decays to zero, Figure 4.3). Preliminary experiments revealed that this method provides bed stress estimates that are in excellent agreement (i.e. within 10%) with ultra-high-resolution measurements of viscous shear stress in the viscous sublayer. The near-bed TKE could be obtained directly from velocity records, and was taken as that at a height of approximately 1 cm above the bed.

4.3 Results

Canopy impact on near-bed flow

The impact of a submerged canopy on the near-bed flow in current-dominated conditions is summarised in Figure

4.3. Relative to a bare bed, the canopy greatly reduces the bed shear stress (τ_b , Figure 4.3.a). The near-bed TKE is similarly reduced (Figure 4.3.b.). Both of these attenuations may explain why canopies are typically regarded as regions of limited erosion and active deposition.

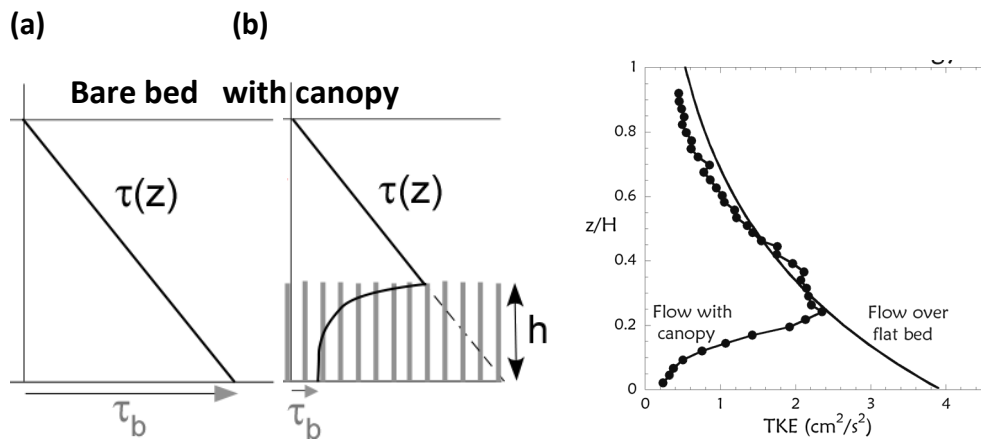


Figure 4.3 Impact of a submerged canopy (of height h) on the bed stress and near-bed TKE. In both cases, relative to a bare bed, the canopy results in significant attenuation, promoting sediment deposition over erosion.

Variation of bed stress in emergent canopies

The relationship between bed stress (as indicated by u_*) and near-bed in-canopy velocity (U_b) was determined from the emergent canopy experiments; in emergent canopies, where the velocity is uniform through the canopy ($u = U_b$ everywhere). The data reveal that, despite canopies being seen as regions of reduced bed stress, there is a clear increase in the ratio u_*/U_b with canopy density (ad , as illustrated in Figure 4.4). This can be explained by the fact that the boundary layer at the bed thins as canopy density increases. Thus, for a given near-bed velocity, the shear (and thus the shear stress) is greater.

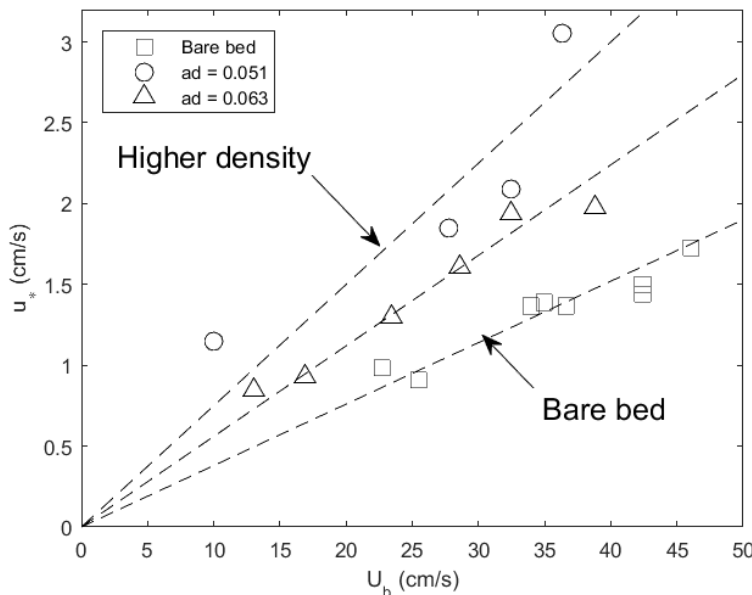


Figure 4.4 The variation of bed stress (as indicated by u_*) with in-canopy velocity U_b in two emergent canopies (of slightly different density ad) and a bare bed. There is a clearly-increasing ratio of u_*/U_b with canopy density.

Across all experiments, it was shown that this dependence on emergent canopy density is best expressed by:

$$\frac{u_*}{u_b} \approx 0.038 \left(1 + (ad)^{\frac{1}{8}} \right) \quad (4.5)$$

To determine the applicability of Eq. (4.1) to canopy flows, data of bed stress from Yang et al. (2015) were employed. This study similarly measured stress in some canopy flows (albeit in a more limited range than that employed here), including control (i.e. bare bed) runs. The agreement between the formulation in Eq. (4.1) and all experimental data is excellent (Figure 4.5). Importantly, this figure incorporates both bare bed and canopy flows, such that Eq. (4.1) is expected to be quantitatively relevant across the entire range of canopy densities in aquatic systems. The coefficient of 0.038 in Eq. (4.1) represents the ratio of u_*/U_b in the absence of a canopy, and is good agreement with previous studies, which suggest a ratio of 1/25 for smooth glass beds. In real systems, however, that coefficient should be replaced with a representative value for a mobile sediment bed, typically seen to be 0.065-0.10.

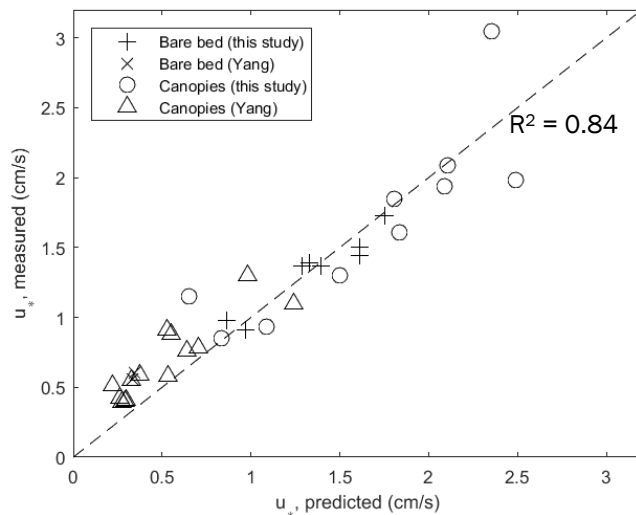


Figure 4.5 Comparison of observed values of bed friction velocity in emergent canopies with those predicted by Equation (4.1). Data from Yang *et al.* (2015) are included for comparison. The dashed line indicates perfect agreement.

Flow attenuation and bed stress in submerged canopies

The formulation in Eq. (4.1) was developed for emergent canopies, where there is a uniform velocity within the canopy (Figure 4.3), such that it is known *a priori*. While it is expected to hold for submerged canopies as well, the near-bed velocity in submerged canopies is not necessarily known. To determine U_b in submerged canopies, we require predictive capability for the current attenuation parameter ($\alpha_c = U_\infty/U_b$) as a function of canopy properties. As flow attenuation by submerged canopies will increase with both the dimensionless density (ad) and the dimensionless canopy height (ah). The experimental results suggest that the attenuation is a unique function of the parameter $\beta = ah\sqrt{ad}$ (Figure 4.6). In this figure, each data point represents the mean attenuation of several runs with a range of free-stream velocities (U_∞); the standard deviation of these is indicated by the error bars. The best-fit curve to the data in Figure 4.6 is given by:

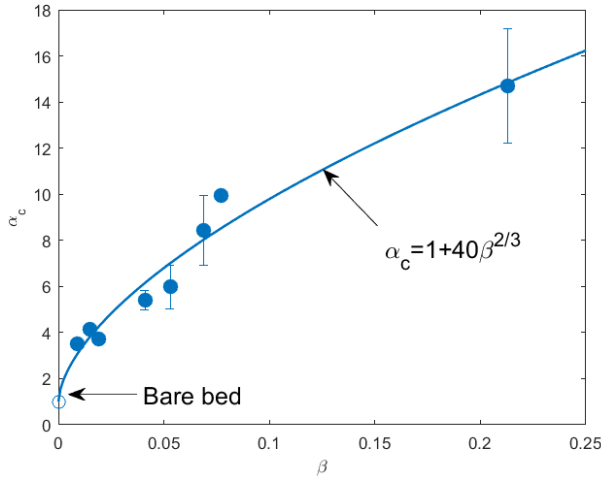


Figure 4.6 The attenuation of flow within submerged canopies. The attenuation parameter α_c shows that the near-bed velocity in submerged canopies can be up to 15 times lower than that in the free-stream well above the canopy. The attenuation parameter is a unique function of β , which is purely a function of canopy properties. The error bars represent the standard deviation of attenuation data across several experiments (with different flow rates) for each canopy. The unfilled marker represents the theoretical value (of 1) in the absence of a canopy.

$$\alpha_c = \frac{U_\infty}{U_b} \approx 1 + 40\beta^{\frac{2}{3}} \tag{4.2}$$

Thus, to determine the bed stress in submerged canopies for given free-stream velocity, Eq. (4.2) can be used to determine the near-bed velocity, with Eq. (4.1) then providing the friction velocity, u_* . The impact of submerged canopies on bed stress in coastal flows is illustrated in Figure 4.7. Here, the stress on a sediment bed overlain by a canopy is compared to that on a bare bed at the same free-stream flow velocity (fixed at 10 cm/s here), as a function of the dimensional canopy density, a . In this analysis, the canopy height is fixed at 30 cm, and the canopy element width at 1 cm. The bed stress can be reduced by several orders of magnitude by dense canopies, but there is the potential for an increase in the bed stress generated by sparse canopies ($a < 10^{-3} \text{ cm}^{-1}$). This is consistent with recent observations of enhanced sediment transport (relative to adjacent bare beds) in regions of low canopy density (see, e.g., van Katwijk et al. 2010, Lawson et al. 2011).

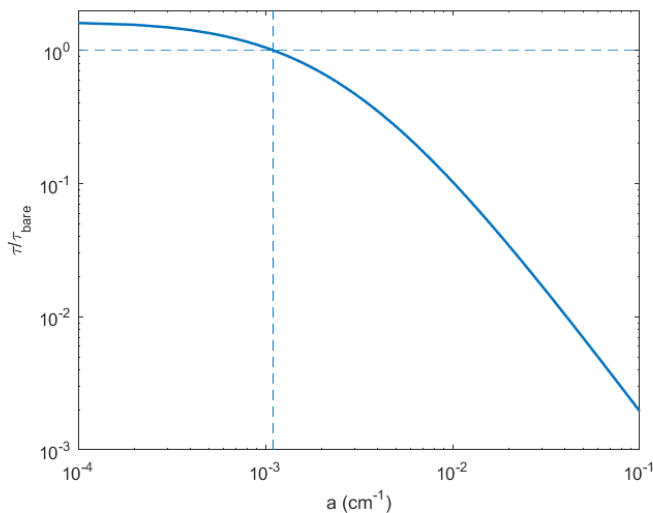


Figure 4.7 The stress on the sediment bed (τ) in a submerged aquatic canopy, relative to that on a bare bed (τ_{bare}), as a function of canopy density. The canopy height (30 cm), element width (1 cm) and free-stream velocity (10 cm/s) have all been fixed in this analysis. Significant stress reduction is seen for denser canopies, while sparser canopies may in fact cause a modest increase in the bed stress.

Near-bed turbulent kinetic energy in submerged canopies

While bed stress is likely to be a driver of sediment transport in canopies, it may not be the only flow descriptor

that determines the onset and rate of sediment transport. In particular, the near-bed TKE has been identified as fundamentally important to the processes that mobilise sediment (see Yang et al., 2016). The impact of the submerged canopies on the strength of near-bed turbulence is demonstrated in Figure 4.8. Here, the near-bed TKE is normalised by the square of the free-stream velocity (which, again, we are treating as known) and is shown as a function of the submerged canopy descriptor β . As in Figure 4.6, each data point represents the mean ratio of several runs with a range of free-stream velocities; the standard deviation of these is indicated by the error bars. The data in Figure 4.8 ultimately represent competing processes. As canopy density and height increase, the in-canopy velocity decreases while the contribution of wake and shear-layer turbulence to the canopy flow increase. Overall, however, the effects of reducing the near-bed velocity dominate such that near-bed TKE is lower in denser submerged canopies. The relationship between normalised TKE and canopy roughness density β is given by:

$$\frac{TKE}{U_\infty^2} \approx 0.004 + 0.0055 \exp(-50\beta) \quad (4.3)$$

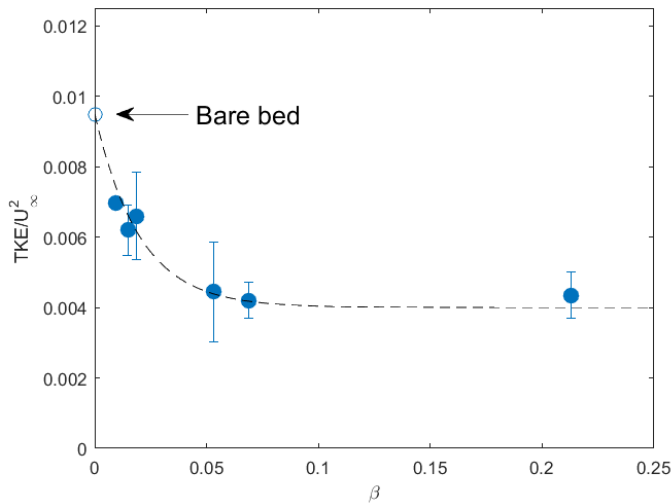


Figure 4.8 The dimensionless near-bed TKE near the bed of submerged canopies. There is a decrease in the value of TKE with the submerged canopy parameter β . The unfilled marker represents the theoretical value (of 1) in the absence of a canopy and is taken from well-known open-channel formulations (Nezu and Nakagawa, 1993). The error bars represent the standard deviation of dimensionless TKE values across several experiments (with different flow rates) for each submerged canopy. The dashed line has the form given in Equation (4.3).

4.4 Discussion

The results of this study demonstrate that, if given the roughness density β of a submerged canopy, and the flow velocity in the absence of the canopy, accurate predictions of the bed-stress and the near-bed TKE can be made. The process for making these predictions is as follows:

Shear stress

1. Employ equation (4.2) to predict the near-bed flow velocity (U_b) given the ambient flow velocity and which requires knowledge of the canopy roughness density, β .
2. With the estimate of U_b from 1), estimate u_* using Equation (4.1).

Near-bed TKE:

1. Use Equation (4.3) to predict the near-bed flow turbulent kinetic energy (*TKE*) given the ambient flow velocity and canopy roughness density, β .

The trends presented in Figures 4.7 and 4.8 show that, for given ambient velocity, both the bed stress and near-bed TKE decrease with increasing canopy density. That is, the two flow parameters that likely drive erosion in canopies decrease with (a) ambient flow speed and (b) canopy density, such that denser canopies in low flows are most likely to be zones of significant deposition.

4.5 References

- Celik, A.O.; Diplas, P.; Dancey, C.L. & Valyrakis, M. (2010), 'Impulse and particle dislodgement under turbulent flow conditions', *Phys. Fluids* **22**, 046601.
- Lawson, S.; McGlathery, K. & Wiberg, P. (2012), 'Enhancement of sediment suspension and nutrient flux by benthic macrophytes at low biomass', *Mar. Ecol. Prog. Ser.* **448**, 259-270.
- Nepf, H. & Vivoni, E. (2000), 'Flow structure in depth-limited, vegetated flow', *J. Geophys. Res.* **105**(C12), 28547-28557.
- Nepf, H.; Ghisalberti, M.; White, B. & Murphy, E. (2007), 'Retention time and dispersion associated with submerged aquatic canopies', *Water Resour. Res.* **43**(4), W04422.
- Nezu, I. & Nakagawa, H. (1993), *Turbulence in open-channel flows*, A.A. Balkema, Rotterdam, the Netherlands.
- van Katwijk, M.; Bos, A.; Hermus, D. & Suykerbuyk, W. (2010), 'Sediment modification by seagrass beds: Muddification and sandification induced by plant cover and environmental conditions', *Estuarine Coastal Shelf Sci.* **89**, 175-181.
- Yang, J.Q., Kerger, F. & Nepf, H.M. (2015) 'Estimation of the bed shear stress in vegetated and bare channels with smooth beds', *Water Resour. Res.* **51**(5), 3647-3663.
- Yang, J.Q., Chung, H. & Nepf, H.M. (2016) 'The onset of sediment transport in vegetated channels predicted by turbulent kinetic energy', *Geophys. Research Lett.*, doi: 10.1002/2016GL071092.

5 Sediment transport in aquatic canopies with current-dominated flows

Abstract

In this Section, we link the onset and rate of sediment transport to the near-bed characteristics of canopy flow. Flume experiments with mobile sediment beds (consisting of uniform glass spheres) were conducted where both the characteristics of the near-bed flow and sediment mobilisation were measured. Firstly, the critical near-bed velocity required to initiate sediment motion in canopies was seen to be significantly lower (by up to 50%) than that observed for a bare bed. This does not mean that canopies promote erosion, though, as the canopies create significant attenuation (by up to an order of magnitude) of the near-bed flow relative to a bare bed (see Section 4). Secondly, once motion is initiated, sediment transport rates are seen to be strongly (and linearly) related to the near-bed turbulent kinetic energy (TKE). Thus, near-bed TKE (for which predictive capability is developed in Section 4) may be the most accurate predictor of rates of transport in canopy systems. Finally, sediment transport occurs on a range of scales in these systems, with variation observed on the scale of the individual canopy elements and also on the scale of the canopy height. This means that canopies that experience spatially-averaged erosion may still contain regions of vigorous deposition (and vice versa).

5.1 Introduction

The laboratory component of this study investigates (a) the hydrodynamic properties (e.g. bed stress, near-bed turbulence levels) that govern sediment transport in these systems, and (b) the impact of a benthic canopy on the thresholds for, and quantity of, sediment transport. Here, we focus on (b) in canopies subjected to steady (i.e. current-dominated) flows.

Given that existing sediment transport formulations have been developed for bare sediment beds (see Fredsøe & Deigaard 1992 for a review), they cannot be directly applied to coastal canopies. In contrast to bare beds, where hydrodynamic forces (e.g. shear stresses) are exerted directly on the sediment, in canopy environments the momentum transfer to the canopy via drag forces can dramatically reduce the forces that act on the sediment. Furthermore, the increased bottom roughness of canopies that enhance the drag encountered by waves and currents also leads to the increased dissipation of hydrodynamic energy in the water column. To account for this dissipation, numerical models of coral reefs and seagrass meadows must incorporate higher bottom drag forces (via increasing drag coefficients) that ultimately result in higher predictions of bottom shear stresses. As a result, application of standard sediment transport models based on smooth bed theory will actually predict greater rates of sediment mobilization and transport; in reality, the opposite will generally occur, with bed shear stresses at the base of the canopy typically being substantially reduced.

Studies quantifying rates of sediment erosion and deposition in vegetation canopies are comparatively rare. Nevertheless, the impact of submerged canopies on sediment transport has been shown to be profound, relative to a corresponding bare bed. The majority of studies (both experimental and field) point to vegetation canopies as regions of net sediment deposition (see extensive reviews of Baptist 2005, Järvelä et al. 2006, Kothyari et al. 2009, Jones et al. 2012, Montakhab et al. 2012). Rates of sediment accumulation can be so high that they result in changes in bed morphology that can further reinforce accumulation, as has been recorded in a variety of vegetation canopies (James et al. 2004). Gacia et al. (1999) demonstrated that particle retention in vegetated beds could be up to 15 times greater than the equivalent non-vegetated bed, and that the rate of deposition was strongly related to the projected surface area of the canopy.

However, recent laboratory and field observations of sediment transport in aquatic canopies have been divergent. Several studies have brought into doubt the core idea that canopies (averaged over the patch-scale) are invariably zones of sediment deposition. Such studies include:

- Those that highlight the importance of the patch size: smaller vegetation patches have been shown to be zones of increased net erosion (relative to their surroundings), especially at the front of the patch (e.g. Fonseca & Koehl 2006, Chen et al. 2012, Follett & Nepf 2012, Ortiz et al. 2013).
- Those that highlight the importance of the canopy density: at low canopy densities, increases in net erosion (again, relative to their surroundings) have been observed (e.g. Van Katwijk et al. 2010, Lawson et al. 2011).

Accordingly, there exists no real predictive capability for sediment transport in vegetation canopies. Studies may provide system-specific descriptions for sediment retention capacity in vegetation canopies (perhaps relative to the corresponding bare bed), but it is unclear how this capacity varies with properties of the canopy and of the ambient flow.

Thus, the aim of this study is to use systematic laboratory experiments to determine the impact of submerged coastal canopies on thresholds for sediment motion and rates of sediment transport. The experiments will highlight the impact of canopy properties on sediment transport and demonstrate the inapplicability of conventional transport formulations to canopy environments.

5.2 Methods

Experimental facilities

Experiments were conducted in two flumes of different scale at the University of Western Australia: a smaller-scale flume (Figure 5.1a, width = 25 cm, maximum depth = 25 cm) for determination of incipient motion and bulk erosion rates and a larger flume (that in Figure 5.2b) used to look at the generation of bedforms in submerged canopies (Figure 5.1b). Canopy and ambient flow properties were varied similarly to Section 5; sediment dynamics in both emergent and submerged canopies were investigated, with canopy density varied significantly ($\alpha = 0.02\text{--}0.10\text{ cm}^{-1}$). Canopies were again represented by arrays of cylindrical dowels (diameter 0.63 cm). Based on matching a dimensionless fall velocity to field conditions, uniform, 200-250 μm glass beads were used as the model sediment. Two series of experiments were done for each canopy condition: one to measure the incipient velocity for sediment transport and the other to quantify the rate of erosion in the canopy (through monitoring changes in bed height).

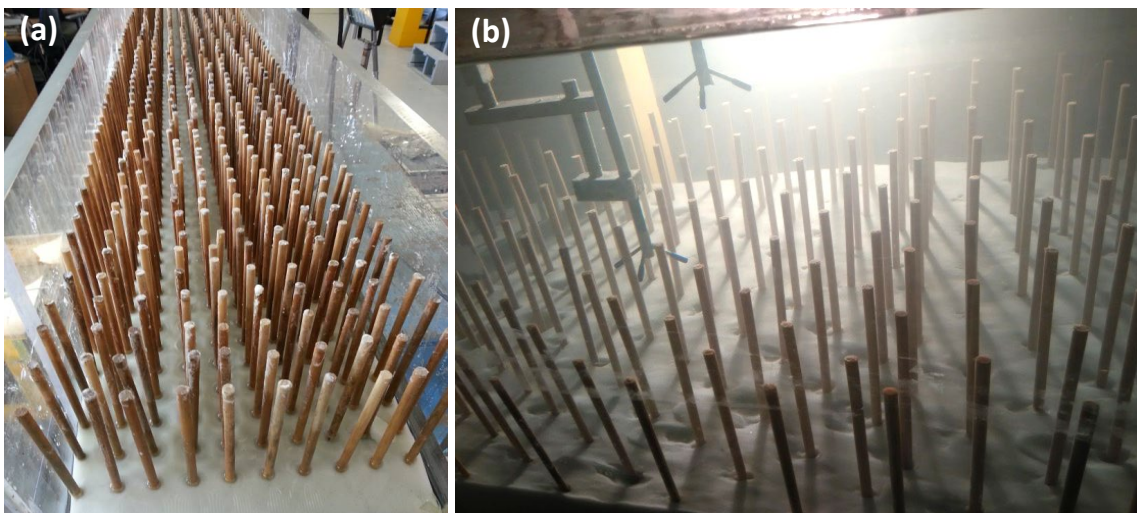


Figure 5.1 The two experimental flumes used in the investigation of sediment transport in aquatic canopies: (a) smaller-scale flume (width = 25 cm), and (b) the larger-scale flume (width = 60 cm) used to looking at sediment bedforms in aquatic canopies.

Measurement techniques

Thresholds for incipient sediment motion were determined by slowly varying the flowrate in the flume, and observing a small section of the sediment bed with a video camera. ADVs were used to determine the bulk and near-bed velocities at the point of incipient motion. ADVs were also employed in all experiments (as in Figure 5.1b) to measure vertical profiles of velocity, with a frequency and spatial resolution similar to that in Section 4.

Sediment transport rates were measured in two ways. Firstly, bulk sediment transport rates were determined from comparison of the spatially-averaged bed height before and after each experiment. A David SLS2 bed scanner (Figure 5.2) was used to scan the model sediment bed. The scanner was attached to a moving trolley to allow transects along the sediment bed. The scanner provided sub-millimetre-resolution of the bed height, and was in excellent agreement with manual measurements of bed height by a pointer gauge (Figure 5.3). This resolution is particularly important given the complex and rapidly-varying bed elevation that is generated in aquatic canopies. Secondly, in all experiments in the larger flume, a sediment trap was placed at the downstream end of the test section to collect the transported bedload as a means of validating the bed scan results.

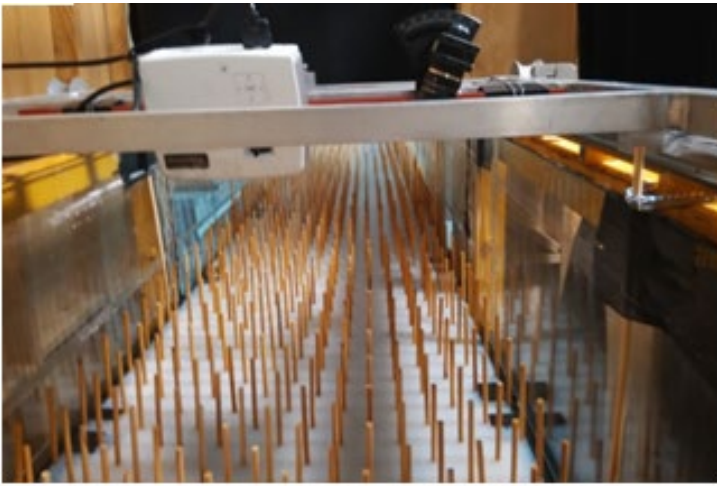


Figure 5.2 The David SLS2 scanning system, which was employed to provide sub-millimetre-resolution estimates of bed height before and after each experiment.

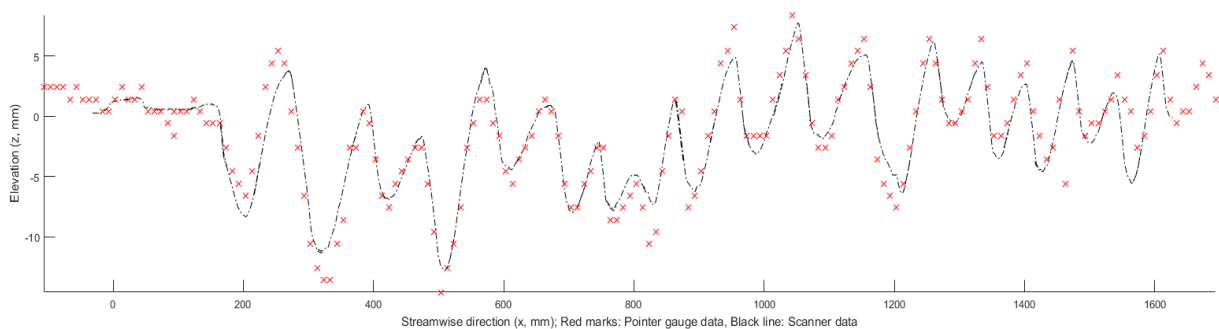


Figure 5.3 The agreement between streamwise transects of bed elevation generated by the bed scanning system (dashed line) and a pointer gauge (red crosses).

5.3 Results

Spatial variability of sediment transport in submerged canopies

Just as the flow within aquatic canopies is highly spatially variable, so too is sediment transport. An understanding of the scales of sediment transport is essential for understanding (a) the impact of horizontal canopy scale size on the net erosion/deposition characteristics, (b) how to determine spatially-averaged sediment transport rates in these systems, and (c) how to accurately describe the impact of benthic canopies on sediment transport. This work has identified sediment transport occurring across several scales within benthic canopies. Three spatial scales that are demonstrably relevant to sediment transport are:

- The ‘element scale’ (typically $O(\text{mm-cm})$) – significant erosion (as evidenced by scour holes) can occur around individual stems (Figures 5.4a and 5.4b), much as it does around pylons and pipelines.
- The ‘canopy scale’ (equivalent to σ^{-1} , typically $O(0.1-1 \text{ m})$) – this represents the (shear-layer) scale of turbulence induced by canopy drag. There is significant sediment transport on the canopy scale in aquatic canopies (Figure 5.4b).
- The ‘patch scale’ (typically $O(1-10 \text{ m})$, but highly variable) – sediment transport on the horizontal scale of a patch of an aquatic canopy will greatly impact the overall sediment retention and flushing within a canopy (Follett & Nepf 2012, Ortiz et al. 2013).

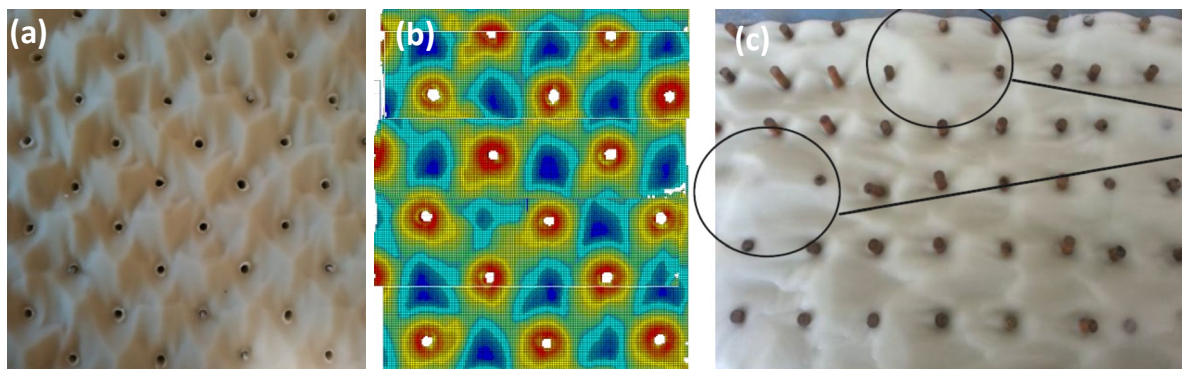


Figure 5.4 Patterns of sediment transport within a benthic canopy. (a) Coherent sediment scour patterns on the scale of the canopy elements (after the elements have been removed at the completion of an experiment) (b) A section of the bed scan of the bed in (a), where red indicates a decrease in bed height over the experiment, and blue an increase (c) Canopy-scale sediment transport, as seen by regions of vigorous deposition (indicated by the black circles) where the canopy elements are completely inundated by the completion of the experiment. The horizontal separation between these regions is of the same order as the canopy scale.

Incipient sediment motion in aquatic canopies

A key aspect of this study is determination of the threshold near-bed velocity ($U_{b,crit}$) require to mobilise sediment in aquatic canopies. Perhaps counter-intuitively, it is seen here that the threshold near-bed velocity decreases with increasing canopy density (Figure 5.5). In this figure, the velocity required to mobilise this sediment in the absence of a canopy ($U_{crit,bare}$) was evaluated through the Shields curve, which allowed determination of the critical value of u_* . Assuming a friction velocity that is roughly 1/10 of the bulk velocity over the rough sediment beds yielded a value of $U_{crit,bare} = 9.3 \text{ cm/s}$. This is consistent with the fact that erosion was observed over the bare bed at all velocities in excess of 10 cm/s.

Through consideration of near-bed turbulent kinetic energy levels, it has been suggested that the ratio of the threshold velocity in an emergent canopy to the corresponding value over a bare bed is given by:

$$\frac{U_{b,crit}}{U_{crit,bare}} = \frac{1}{\sqrt{1+36\left(\frac{\pi}{4}ad\right)^{2/3}}} \quad (5.1)$$

(Yang et al., 2016). This expression is shown in Figure 5.5 as the dashed line. As canopy density increases, the observed threshold near-bed velocity falls below the emergent canopy prediction. This is likely due to the generation of shear-layer-scale turbulence in the submerged canopies which, as an additional source of turbulence, mobilises the sediment more readily.

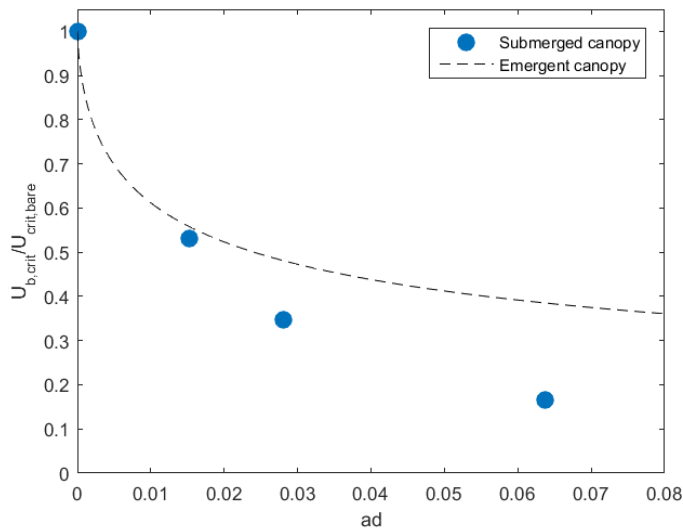


Figure 5.5 Threshold velocities for sediment motion in submerged canopies ($U_{b,crit}$), relative to the expected value over a bare bed ($U_{crit,bare}$). This ratio decreases with canopy density, falling below the theoretical formulation for emergent canopies in Equation (5.1) (dashed black line).

Sediment transport rates

Once sediment transport is initiated, by having the near-bed velocity exceed the critical value given in Figure 5.5, overall rates of sediment transport are lower in denser canopies (Figure 5.6). In this figure, the “relative erosion rate” is plotted as a function of the canopy roughness density β across all experiments. The relative erosion rate represents the observed rate of erosion of a sediment bed in a canopy, relative to that observed for a bare bed at the same ambient velocity (U_∞). The decrease in relative erosion rate with canopy density is entirely expected, given that both bed stress and near-bed TKE (for fixed above-canopy velocity) decrease with increasing density (see Figures 5.7 and 5.8). As shown in Figure 5.6, canopies with $\beta < 0.08$ can reduce (relative to an adjacent bare bed) the overall erosion rate by up to 40%.

The variation of sediment transport with canopy density for a given value of above-canopy velocity can be viewed as competition between two effects. Firstly, as canopy density increases, the attenuation of the near-bed flow increases. However, there is a simultaneous reduction in the critical near-bed velocity required for sediment mobilisation (Figure 5.5). As can be seen in Figure 5.6, the attenuation of the near-bed flow (and thus near-bed TKE levels) is greater, such that erosion rates decrease with canopy density.

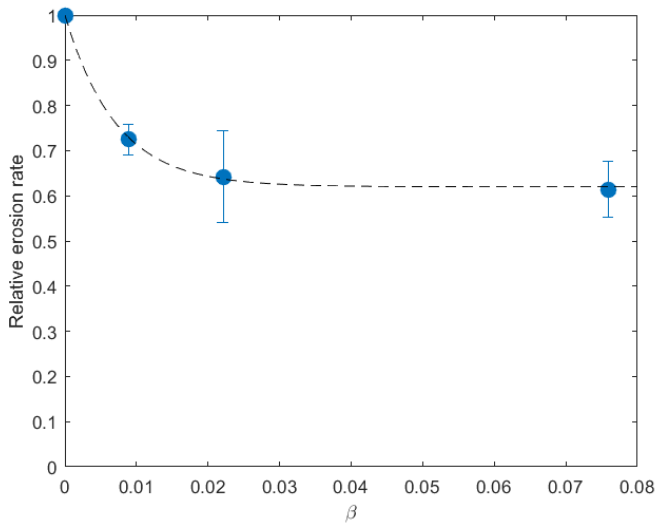


Figure 5.6 The trend of spatially-averaged erosion rate within the canopy, as a function of both the flow speed (the bulk velocity is given in the legend), the canopy density and canopy type (emergent vs submerged). There is a clearly nonlinear relationship between canopy density and sediment transport, with maximum sediment transport observed at intermediate density ($ad \approx 0.03$)

The flow characteristic seen to be most strongly linked to rates of sediment transport is the near bed TKE ($R^2 = 0.94$, Figure 5.7b). There is a positive, but weaker, dependence of sediment transport rates on the bed stress ($R^2 = 0.42$, Figure 5.7a). Figure 5.6 strongly suggests the possibility of describing sediment transport rates through TKE levels within the canopy. This is supported by the fact that the curve in Figure 5.6 takes almost exactly the same form as that in Figure 4.8. That is, as canopy density increases for a given ambient current speed, both the near-bed TKE and rates of sediment transport decrease (at the same rate).

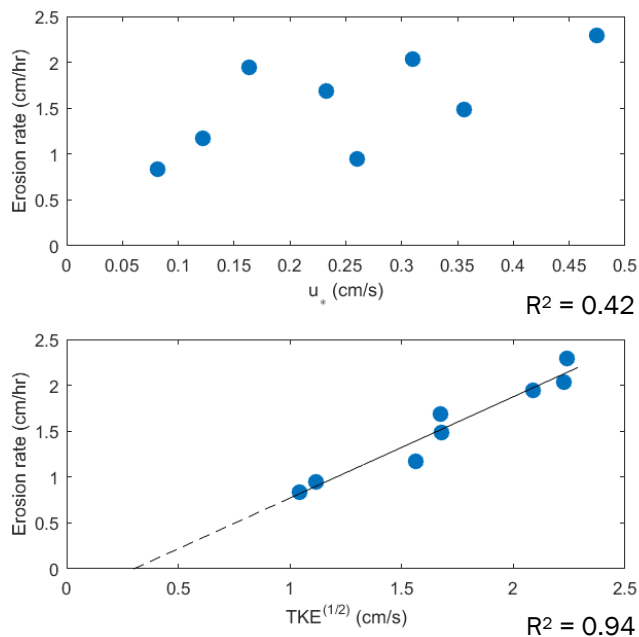


Figure 5.7 The linear dependence of erosion rates in submerged canopies on the near-bed TKE. The x-intercept of the line of best fit is positive, suggesting the possibility of a ‘threshold TKE’ in canopy sediment transport.

5.4 Discussion

Erosive v depositional environments

The near-bed flow velocity required to initiate sediment motion is shown to be lower than that over a bare bed. This lowering of the threshold velocity is in reasonable agreement with Equation (5.1) developed for emergent canopies; the additional turbulence of the canopy shear layer causes even greater diminishment of the threshold velocity. Use of the mean near-bed velocity still represents the most robust way of describing sediment transport

thresholds in canopy systems. Traditional approaches can be used to determine the near-bed velocity required for incipient motion for a particular sediment grain size in a bare bed (e.g. the Hjulstrom curve). From Equation (5.1) and/or Figure 5.5, the corresponding velocity required in the canopy can be determined. Given the ambient current speed, this can be compared to the actual in-canopy velocity, predicted through Equation (4.2); if the predicted velocity exceeds the threshold, erosion will occur. Otherwise, the canopy will be a depositional environment. The description of sediment transport thresholds from this study can thus be extrapolated to any sediment grain size, including the comparatively fine material in dredging plumes.

Quantifying rates of sediment transport

Once sediment motion is initiated, the rate at which sediment is transported through the canopy is shown to depend linearly on the near-bed turbulent kinetic energy (TKE). That is, turbulence mobilises the sediment, which is then entrained into the flow and transported as either bedload or suspended load. That is, the bed stress, the widely-adopted descriptor for sediment transport in coastal systems, is the less effective predictor in canopy systems. Existing hydrodynamic/sediment transport models typically have the means for bed stress prediction, and the results presented in Section 4 (which agree well with other experimental data) are sufficiently robust for extrapolation to a wide range of canopy systems. Conversely, models are not configured to predict near-bed turbulence levels, and Figure 4.8 contains the only known data that evaluate TKE as a function of canopy and ambient flow properties. It is recommended that both approaches to predicting transport rates of dredged sediments be considered, with field observations of dredging plume deposition and remobilisation used to determine the optimal modelling approach. Extrapolation of the results in Figure 5.7 to other sediment sizes remains untested; thus, while spatial and temporal variation in sediment transport can be described qualitatively, precise rates (in, say, cm/hr) for the finer sediment in dredging plumes cannot.

Broadly, the implications of these findings for understanding the impact of dredging plumes are as follows:

1. High density canopies in low-flow conditions are most at risk of experiencing significant rates of sediment deposition. Although the threshold near-bed velocity falls with canopy density, the attenuating effects of the canopy overcome this, such that the true near-bed velocity is most likely to fall below the threshold value.
2. In understanding the timescale of sediment retention within a canopy, the rates of sediment transport during comparatively high-flow periods become important. These transport rates decrease with increasing canopy density and decreasing current speed, such that canopies are seen here to reduce rates of erosion by up to 40%, relative to adjacent bare bed regions.

5.5 References

- Baptist MJ (2005) Modelling floodplain biogeomorphology. Delft University of Technology, Delft, Netherlands
- Chen Z, Ortiz A, Zong L, Nepf H (2012) The wake structure behind a porous obstruction and its implications for deposition near a finite patch of emergent vegetation. *Water Resources Research* 48(9), DOI: 10.1029/2012WR012224
- Follett EM, Nepf HM (2012) Sediment patterns near a model patch of reedy emergent vegetation. *Geomorphology* 179:141-151
- Fonseca MS, Koehl M (2006) Flow in seagrass canopies: the influence of patch width. *Estuarine, Coastal and Shelf Science* 67:1-9
- Fredsøe J, Deigaard R (1992) Mechanics of coastal sediment transport, Vol 3. World Scientific.
- Gacia E, Granata TC, Duarte CM (1999) An approach to measurement of particle flux and sediment retention within seagrass (*Posidonia oceanica*) meadows. *Aquatic Botany* 65:255-26.
- James WF, Barko JW, Butler MG (2004) Shear stress and sediment resuspension in relation to submersed macrophyte biomass. *Hydrobiologia* 515:181-191
- Järvälä J, Aberle J, Dittrich A, Rauch H, Schnauder I Flow-vegetation-sediment interaction: Research challenges. *Proc River Flow*, p. 2017-2026
- Jones J, Collins A, Naden P, Sear D (2012) The relationship between fine sediment and macrophytes in rivers. *River Research and Applications* 28:1006-1018
- Kothyari UC, Hashimoto H, Hayashi K (2009) Effect of tall vegetation on sediment transport by channel flows. *Journal of Hydraulic Research* 47:700-710
- Lawson S, McGlathery K, Wiberg P (2011) Enhancement of sediment suspension and nutrient flux by benthic macrophytes at low biomass. *Marine Ecology Progress Series* 448:259-270
- Montakhab A, Yusuf B, Ghazali A, Mohamed T (2012) Flow and sediment transport in vegetated waterways: a review. *Reviews in Environmental Science and Bio/Technology* 11:275-287
- Ortiz AC, Ashton A, Nepf H (2013) Mean and turbulent velocity fields near rigid and flexible plants and the implications for deposition. *Journal of Geophysical Research: Earth Surface* 118:2585-2599
- Van Katwijk M, Bos A, Hermus D, Suykerbuyk W (2010) Sediment modification by seagrass beds: Muddification and sandification induced by plant cover and environmental conditions. *Estuarine, Coastal and Shelf Science* 89:175-181
- Yang JQ, Chung H, Nepf HM (2016) The onset of sediment transport in vegetated channels predicted by turbulent kinetic energy. *Geophysical Research Letters*, doi: 10.1002/2016GL071092.